CHALMERS

Ringhals Diagnostics and Monitoring, Annual Research Report 2021-22

I. PÁZSIT

L. A. TORRES

C. MONTALVO

V. DYKIN

M. Al-DBISSI

P. VINAI

H. NYLÉN

Ringhals Diagnostics and Monitoring, Annual Research Report 2021-2022

I. Pázsit, L. A. Torres, C. Montalvo, V. Dykin,
M. Al-dbissi, P. Vinai and H. Nylén

Ringhals Diagnostics and Monitoring, Annual Research Report 2021-2022

**I. Pázsit, L. A. Torres, C. Montalvo, V. Dykin,
M. Al-dbissi, P. Vinai and H. Nylén**

**Nuclear Engineering Group
Division of Subatomic, High Energy and Plasma Physics
Chalmers University of Technology
SE-412 96 Göteborg, Sweden**

Abstract

This report gives an account of the work performed by the Division of Subatomic, High Energy and Plasma Physics (formerly, Division of Nuclear Engineering), Chalmers, in the frame of a research collaboration with Ringhals, Vattenfall AB, contract No. 4501747546-003. The contract constitutes a one-year co-operative research work concerning diagnostics and monitoring of the PWR units. The work in the contract has been performed between 1 July 2021 and 30 June 2022. During this period, we worked with four main items as follows:

1. Further analysis of the vibrations of thimble tubes with axially dependent in-core measurements in various radial positions;

2. Evaluation of new ex-core measurements for beam, reactivity, shell and tilting mode vibrations in R3;

3. Preliminary evaluation of the feasibility of a conceptual design, through simulations and pilot measurements, of a fibre-based detector for the measurement of the gradient of the neutron flux;

4. Investigation of the possibility of detecting subcooled boiling in the upper part of a PWR through evaluation of in-core measurements made by movable detectors.

The work was performed by Imre Pázsit (project co-ordinator at Chalmers), Luis Alejandro Torres and Cristina Montalvo (research collaborators from UPM, Madrid), Victor Dykin, Moad Al-dbissi, Paolo Vinai and Henrik Nylén, the latter being the contact person at Ringhals. The work reported in Chapter 4 (item 3 above) was performed together with our collaborating partners Alessandro Borella and Riccardo Rossa at the Belgian nuclear research centre SCK CEN.

CONTENTS

1. INTRODUCTION

This report gives an account of the work performed by the Nuclear Engineering Group of the Division of Subatomic, High Energy and Plasma Physics (formerly, Division of Nuclear Engineering), Chalmers, in the frame of a research collaboration with Ringhals, Vattenfall AB, contract No. 4501747546-003. The contract constitutes a one-year co-operative research work concerning diagnostics and monitoring of the BWR and PWR units. The work in the contract has been performed between 1 July 2021 and 30 June 2022. During this period, we worked with four main items as follows:

1. Further analysis of the vibrations of thimble tubes with axially dependent in-core measurements in various radial positions;

2. Evaluation of new ex-core measurements for beam, reactivity, shell and tilting mode vibrations in R3;

3. Preliminary evaluation of the feasibility of a conceptual design, through simulations and pilot measurements, of a fibre-based detector for the measurement of the gradient of the neutron flux;

4. Investigation of the possibility of detecting subcooled boiling in the upper part of a PWR through evaluation of in-core measurements made by movable detectors.

The work was performed by Imre Pázsit (project co-ordinator at Chalmers), Luis Alejandro Torres and Cristina Montalvo (research collaborators from UPM, Madrid), Victor Dykin, Moad Al-dbissi, Paolo Vinai and Henrik Nylén, the latter being the contact person at Ringhals. The work reported in Chapter 4 (item 3 above) was performed together with our collaborating partners Alessandro Borella and Riccardo Rossa at the Belgian nuclear research centre SCK CEN.

2. FURTHER ANALYSIS OF THE VIBRATIONS OF THIMBLE TUBES WITH AXIALLY DEPENDENT IN-CORE MEASUREMENTS IN VARIOUS RADIAL POSITIONS

The phenomenon of thimble tube vibrations, and the possible consequences of these vibrations and impacting of the thimble tubes on the instrument tubes have long been known. The problem got a wider attention first within the nuclear program of EDF in the late 1980's, when their 1300 MWe PWR plants were introduced [1, 2]. Several cases of thimble tube vibrations and their effects were observed, including fatigue and wear of both the thimble tube and the instrument tube, and in some cases leaks in the thimble tube. This resulted in the fact that EDF launched a dedicated program for the surveillance and monitoring of thimble tube vibrations and impacting [3].

The investigation of possible thimble tube vibrations was taken up within the Chalmers-Ringhals collaboration in Stage 2018 [4], when also a survey of the literature on the previous experiences was performed. As it was described in Ref. [4], the diagnostic problem is rather complicated. The characteristics of these vibrations is very varied, as they are functions of a number of different factors, such as the fuel assembly type, the contact surface between the fuel assembly bottom nozzle and the thimble tubes, and not the least the radial position in the core.

According to the EDF experience, there are two possibilities to detect and quantify thimble tube vibrations, and possibly detect impacting. The most effective method is to use ex-core accelerometers, attached to the guide tubes below the bottom of the pressure vessel. These accelerometers can detect both the vibrations (from the periodic component of the signal) as well as impacting (from the spikes caused by the impacting). Unfortunately, this possibility is not available in Ringhals, due to the absence of such accelerometer signals, hence the other, less effective method of analysing the in-core neutron noise measurements has to be used.

From the neutron noise diagnostic point of view, detection of thimble tube vibrations shows some resemblance to the detector instrument tube vibrations and impacting in BWRs [5]. BWR instrument tube vibrations can also lead to impacting against the wall(s) of some of the surrounding four fuel boxes. In some cases heavy impacting led to damage of the LPRM detectors in the instrument tube, and even to holes in the fuel channel walls, leading to undesired cross-flow. Such instrument tube vibrations and impacting have occurred also in Swedish BWRs [5], and the problem was investigated in several previous Stages, i.e from Stage 8 through Stage 12 [6, 7, 8, 9, 10], as well as in some stages of the SKI reports [11, 12, 13].

However, detection of BWR instrument tube vibrations is significantly simpler than that of the thimble tube vibrations. In the BWR case, each and every one of the 36 instrument tubes contains not only one, but four LPRM detectors. Hence, in every case of a vibrating instrument tube, the four detectors of the detector string in that tube will all exhibit a peak at the vibration frequency, due to the movement of the detectors in a flux gradient. The frequency of the detector string

vibrations is also known, it is around 2-3 Hz, and it is easily observed and pointed out in the otherwise smooth frequency dependence of the in-core BWR neutron noise spectrum. A final advantage is that one can take the cross-spectrum between two detectors in the same detector string, sitting at different axial positions. In a normal (vibration-free) case, the phase depends linearly on the frequency, which is a characteristics of the "propagation noise" [14], due to the transit of the void between the two detectors. The vibrations, which are in-phase and hence have zero phase delay between two detectors in the same string, will distort this nice linear phase, bringing it closer to zero around the vibration frequency. This gives immediately a hint on the existence of vibrations, but even on their severity, through the severity of the distortion.

In contrast, in the case of the Swedish PWRs (like in all Westinghouse-type PWRs), there are no fixed in-core detectors installed. One can make short measurements with a maximum of 4 movable detectors at a time, and these have to be in different guide tubes, i.e. in different radial core positions. This means that by relying on the same method as with BWR instrument tube vibrations, i.e. detecting thimble tube vibrations from the noise signals induced by the vibrations of the detectors themselves, only a very small fraction of all thimble tubes can be diagnosed. A further complication is that auto power spectra (APDS) of the PWR in-core movable detectors contains a considerably larger number of peaks, not to mention that the eigenfrequency of the thimble tubes is not known. The axial dependence of the amplitude of the possible thimble tube vibrations is not known either. Last, but not least, the possibility of cross-correlating detector signals in the same instrument tube is also missing.

What concerns the vibrations of thimble tubes that do not contain movable detectors, the only possibility of detecting these from in-core measurements performed in other thimble tubes, is to utilize the noise induced by the vibrations of the detector-free thimble tubes. The principle of the detection in this case is different from that of the case of a vibrating thimble tube containing a detector. The principle in this case is that a thimble tube can be interpreted as an absorber, hence its vibrations would lead to a neutron noise with the characteristics of a (laterally) vibrating absorber. In the neighbourhood of such a vibrating absorber, two neutron detectors at opposite sides of the vibrating object would show out-of-phase behaviour, or at least significant deviations from the in-phase behaviour (which is the characteristics of an absorber of variable strength, such as a channel-type two-phase flow instability).

However, this method has substantial weaknesses. First, the amplitude of the induced noise will be rather small. Compared to a control assembly containing large volumes of strong neutron absorbers, the thimble tube contains small amounts of weakly absorbing material. Second, the range of the local component of the vibration induced noise (which is the reason of the opposite phase behaviour between two detectors at opposite sides of the vibrating thimble tube) is short. In practice this means that using the maximum of 4 detectors, the possible vibrations of detector-free thimble tubes can only be detected in between the 3 pairs of closest instrumented tubes. Third, the possible vibrations of individual fuel assemblies will also induce neutron noise, which might exceed the noise induced by the vibrating thimble tube.

Last, but not least, if any of the two instrumented thimble tubes, used to identify the vibrations of non-instrumented thimble tubes, should also vibrate during the measurement, then the noise induced by their own vibration will suppress completely the weak noise induced by the vibrations of the non-instrumented thimble tube.

It is thus seen that the problem to be solved contains a number of unknown parameters and lacking necessary information, with only a few measured data. The only way of having some insight is to progress in a heuristic trial-and-error manner. Therefore we expect that this phenomenon will be investigated during several further Stages, possibly with various analysis methods.

Our previous experience with in-core PWR neutron noise measurements stems from some of the earlier stages, such as Stages 4, 12 and 13 [15, 10, 16], when in-core measurements were performed in five radial positions simultaneously, at four or six different axial positions. However, the purpose of those measurements was different. At that time, the interest was not on the investigation of thimble tube vibrations. Rather, based on the literature and similar studies in the US, we assumed that all measured in-core noise is due to fuel assembly vibrations. Hence in those measurements we attempted to identify the axial vibration modes of the individual fuel assemblies, and also to assist the analysis of the ex-core measurements for the diagnostics of shell mode vibrations. It was assumed that the individual peaks in the in-core detector signals were due to the vibrations corresponding to the various bending modes of the fuel assemblies. In the analysis of those measurements, only the APDSs of the individual detectors were investigated.

The first attempt to diagnose thimble tube vibrations was made during Stage 2018 [4]. In that year, no new in-core measurements were possible to make, hence we decided to use the in-core measurements analysed in Stage 12 for fuel assembly vibrations, taken in 2008, in cycle 25 in R4. Since the peak structure of those measurements was already analysed in Stage 12 and was found rather difficult to interpret, we decided to analyse the hypothetical scenario that none of the instrumented thimble tubes would vibrate, hence a peak of the coherence and out-of-phase between radially close detector pairs at the same axial elevation would indicate the vibration of a thimble tube in between the two radial positions. No clear-cut decision was possible to be drawn from the analysis. A slight possibility of thimble tube vibrations was seen between one of the detectors and other three detectors, around 2 - 6 Hz. An even slighter possibility was seen for vibrations centered around 20 Hz, although too broad in frequency (15 - 25 Hz) to correspond to vibrations. The fact that one of the detectors in a group of four did not share the out-of-phase behaviour with the fifth detector was interpreted as a possibility that particular instrumented thimble tube could have vibrated.

In Stage 2020, two new measurements were made in R3, with two different layouts. However, for reasons described in the report [17], only Measurement 1 was evaluated. Since these data were new, we investigated both the peaks in the auto-spectra for each detector in all six axial positions, as well as the coherence and phase between two detectors at the same axial position. In the present stage, two measurements of the same structure were made, and this time both were evaluated. The layout of the measurements, and the analysis results will be discussed in the

following.

2.1 The layout and details of the measurements

In the in-core measurements, four movable in-core detectors were used, labeled from A to D. The layout of the measurements, i.e. the radial and axial detector positions used in the measurements are shown in Figs. 2.1 and 2.2, respectively. (Note that, in contrast to the previous Stage, the quantitative value of the position of the measurement levels in centimetres follows now the Ringhals convention, i.e. the distances are now measured from the top of the core). The detector notations with their corresponding core positions are shown in Table 2.1.

In-core detector	Core position
A	N12
B	N08
C	N10
D	L04

Table 2.1: The detector designations in the instrumented thimble tubes and their core positions.

As it is seen on the core map of Fig. 2.1, and also from Table 2.1, the in-core detectors are aligned nearly along a line (in column N of the core, except detector D). Originally, detector D was intended to be placed into the core position N05, but this position shares the guide tube switch with position N12, which is already used in the measurement, this is why position L04 was chosen for detector D. Due to the placing of the detectors, in the coherence and phase analysis, one expects information on the possible vibrations of thimble tubes in column N or its neighbourhood.

Regarding the measurement system, a Westinghouse digital Flux Mapping System was installed in R3 during the outage 2016. The thermal neutron sensitivity of the four in-core flux detectors (fission chambers) ranges up to 10^{14} nv, although noticeable variation of the sensitivity amongst the detectors can be observed. The sampling frequency was 62.5 Hz for all three sets of measurements. The structure of the measurement was similar to that of the ex-core measurements, in that four in-core detector AC signals replaced four of the regular ex-core DC signals. The registered quantities (static and fluctuating parts, i.e. DC and AC, respectively) are shown in Table 2.2.

From the foregoing, in particular from Table 2.2, it is seen that for the in-core detectors, the DC component was not registered. This means that, unlike with the ex-core measurements, there is no possibility to normalise the signals to their static (average) value. This does not incur much problem for the investigations of the thimble tube vibrations, as long as one is interested in the structure of the spectra and the coherences/phases, without trying to perform a quantitative trend analysis. However, it affects the usefulness of the data when the axial dependence of the amplitudes is investigated, which will be the case in Chapter 5 on the detection of subcooled boiling.
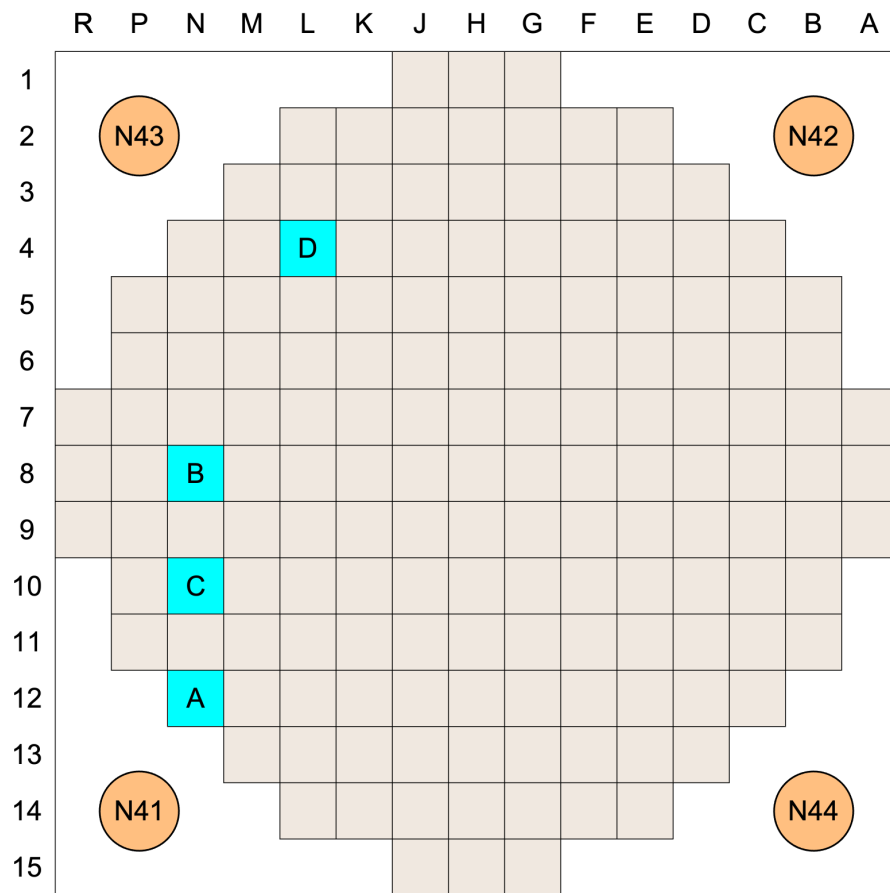
Figure 2.1:   The radial positions of the four in-core detectors.
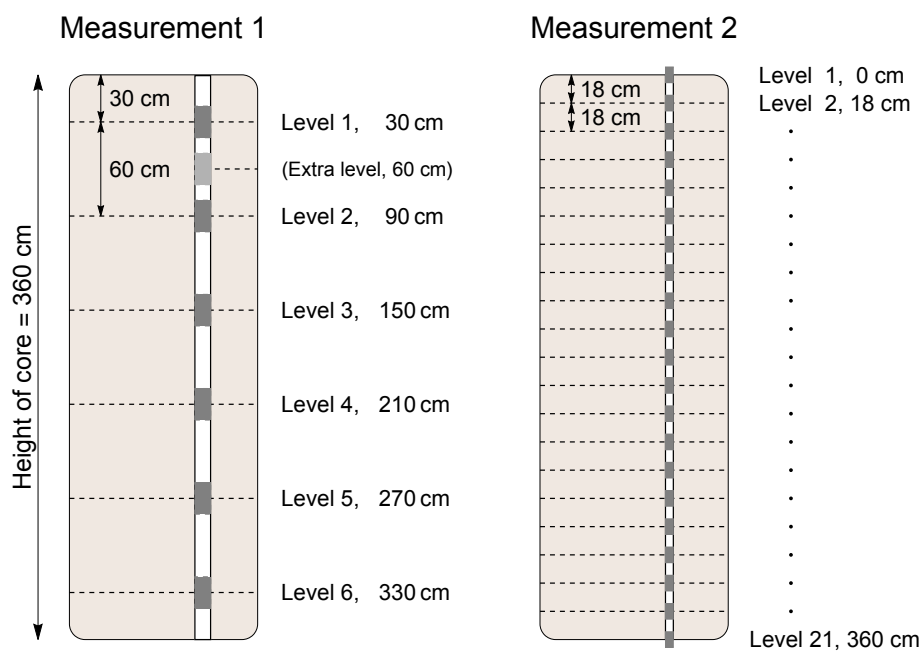
Figure 2.2:   The axial positions of the measurement points in the two measurements.

Table 2.2:   The measurement data structure of the two in-core measurements in Ringhals 3 on 2022-04-08

Channel	Measurement point
0	Time
1	N41U DC
2	N42U DC
3	N43U DC
4	N44U DC
5	IncoreA_N12 AC
6	IncoreB_N08 AC
7	IncoreC_N10 AC
8	IncoreD_L04 AC
9	N41U AC
10	N42U AC
11	N43U AC
12	N44U AC
13	N41L AC
14	N42L AC
15	N43L AC
16	N44L AC

Two measurement series were made, both on 8 April 2022, in cycle 39 of R3. In each series, measurements were made at a number of axial positions during a given time for all four detectors. Then all detectors were moved simultaneously to the next position, another measurement of the same length was taken, and so on.

In Measurement 1, similarly to the previous Stage, the original plan was to make measurements in six axial positions, each being 20 minutes long. The first position, Level 1, was 30 cm below the core top, then the detectors were lowered by 60 cm to the next position in five consecutive steps, the last measurement being taken 30 cm above the bottom of the core. The measurement data for each level was stored in a different file, containing the signals of all four detectors for that level (plus that of the ex-core detectors). However, in addition to the original plan, an extra measurement was made between Level 1 and Level 2, i.e. 60 cm below the top of the core (see Fig. 2.2). This extra measurement was not evaluated for the investigation of the thimble tube vibrations; it was only accounted for in a different context, in the investigation of the detection of subcooled boiling (Chapter 5).

In Measurement 2, the measurement was taken in one sequence, without interrupting the data logging, such that all four in-core detectors were moved simultaneously between the measurement positions. In this series, a one-minute measurement was made in 21 subsequent axial positions, separated by 18 cm from each other. The first 1-minute measurement was taken in level with the core bottom (360 cm in Ringhals terminology), and the last at the level of the core top (0 cm). The axial positions of the detectors in the two measurement series are shown in Fig. 2.2.

In this Stage, both Measurement 1 and Measurement 2 were evaluated. In Measurement 1, a spectral analysis (APSD, coherence and phase) was performed for each level. Measurement 2 was conceived in order to analyse it with wavelet transform methods, in order to follow the evolution of the characteristic peaks in time as the detectors are stepwise moved from the bottom of the core to the top in steps of 18 cm, hence revealing at which positions characteristic frequencies occur, and which frequencies are persistent (not depending on the measurement position). This is equivalent with a short-time Fourier transform with a sliding time window. This is now investigated quantitatively.

2.2 Results of the analysis of Measurement 1

2.2.1 Power spectra

As discussed in the previous section, the power spectra (APSDs) are mostly useful to detect and interpret vibrations of the instrumented thimble tubes themselves, and the interpretation of the spectra will be made with this point of view in mind. The APSDs of Measurement series 1 are displayed in two different layouts. In Figs 2.3 and 2.4, the APSDs of all four detectors are shown, taken at the three upper and the three lower axial positions, respectively. In Figs 2.5 and 2.6 the spectra of the four detectors are shown in separate plots, in each plot the 6 spectra are shown for the six axial positions in which the measurements were made.

As discussed in the previous Stage, these spectra show both similarities and

Figure 2.3: APSDs of the four detectors A, B, C and D at the three upper axial positions (levels 1 - 3).
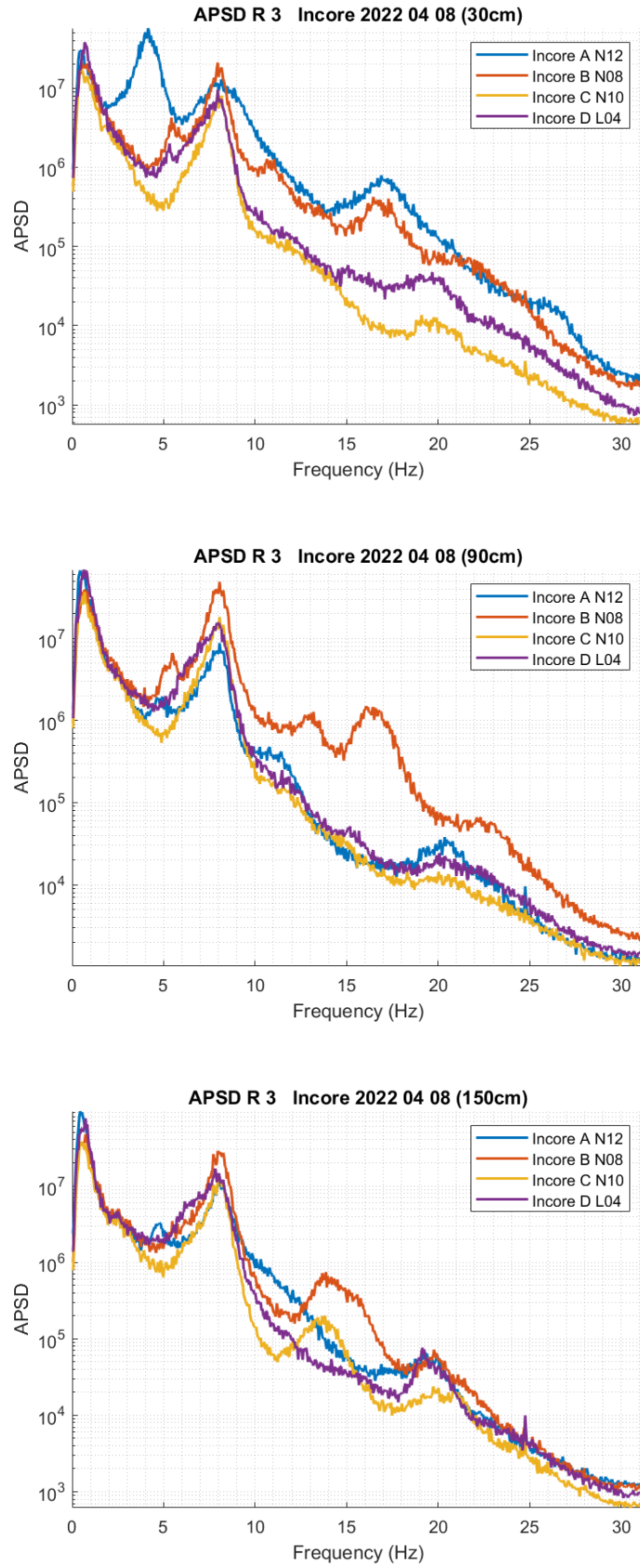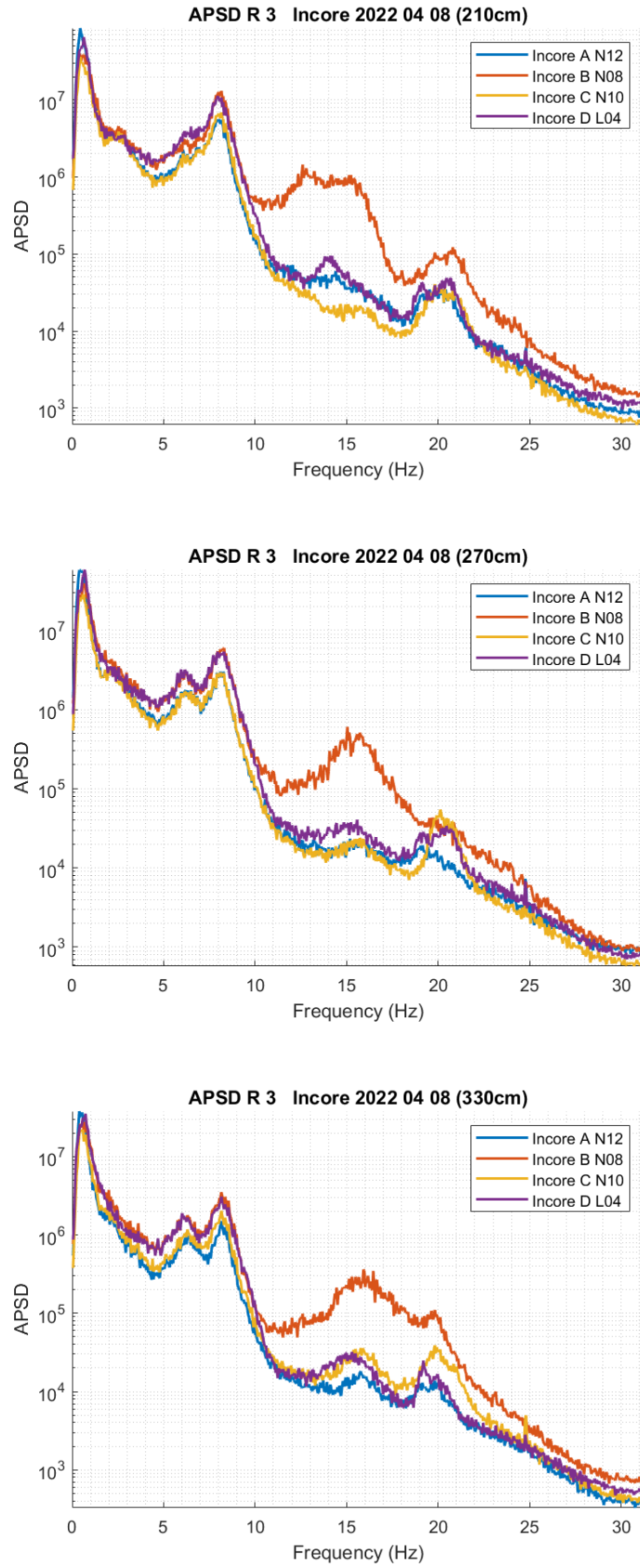
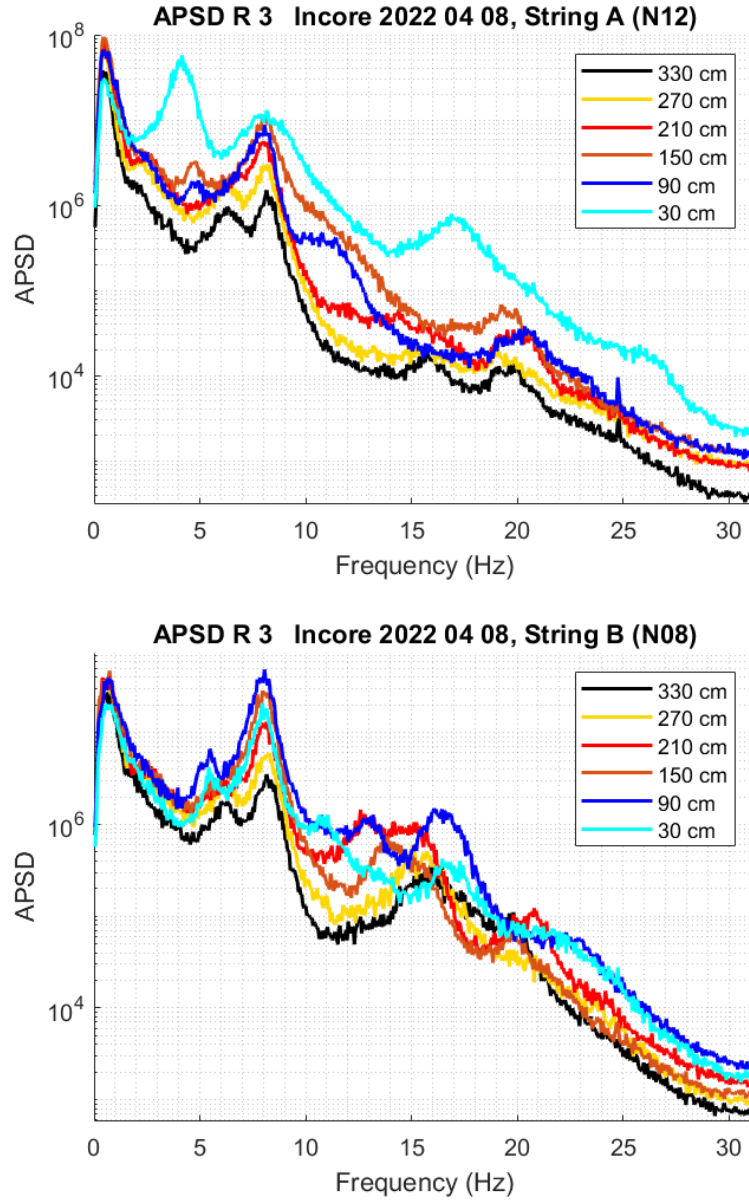Figure 2.4: APSDs of the four detectors A, B, C and D at the three lower axial positions (levels 4 - 6).

Figure 2.5: Individual APSDs of the detectors in the strings N12 and N08 at all 6 axial positions in one plot
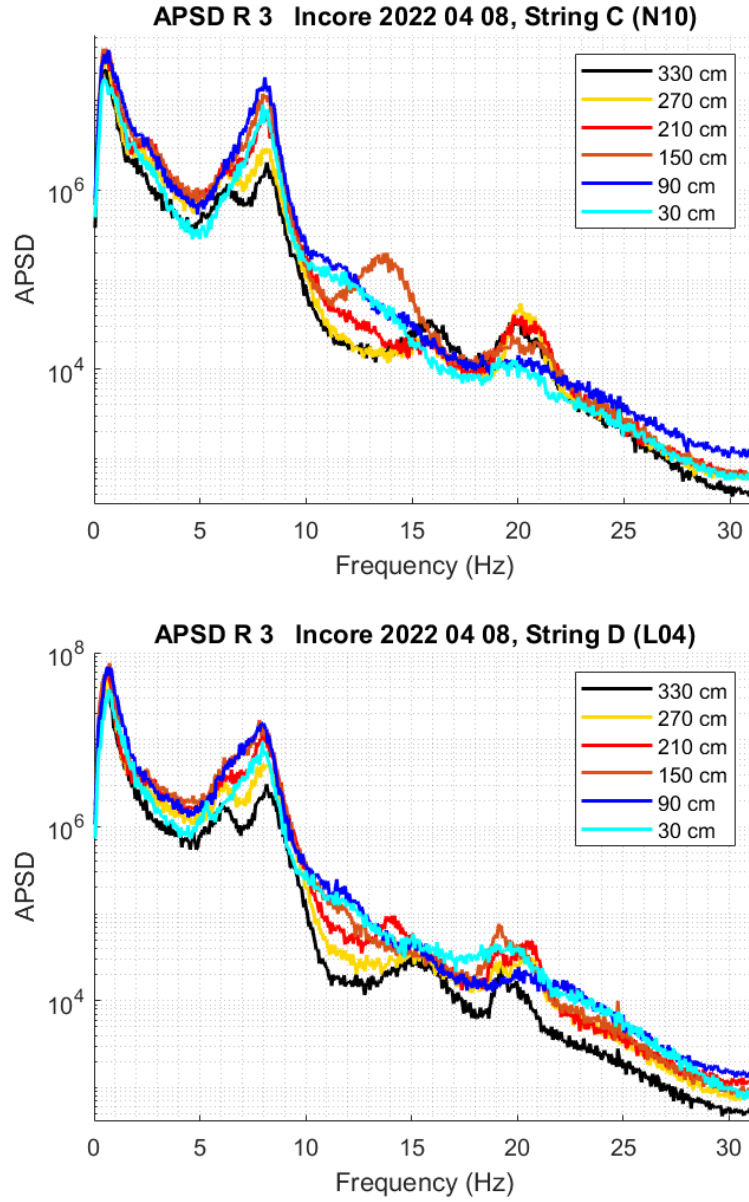
Figure 2.6: Individual APSDs of the detectors in the strings N10 and L04 at all 6 axial positions in one plot

differences compared to those in the measurements taken in R4 in 2008 [10]. In the 2008 measurements, in practically all measurements, there was a relatively broad peak at around 6-7 Hz, which was most likely the superposition of two peaks with close frequencies (6 and 7 Hz, respectively). In the previous Stage, there was one dominating sharp peak around 8 Hz, which was partly higher than the broad one in the R4 measurements in 2008, and the peak was significantly narrower. This peak was present in all detectors and at all axial levels. It has the same frequency as the 8 Hz peak in the ex-core signals, attributed to the individual fuel assembly vibrations.

In addition, there were some other peaks, which only occurred in certain detectors and/or at certain axial elevations. In the two lowermost positions, nearly all detectors showed an additional narrow peak at around 5 - 6 Hz. Further, detector D showed a broad peak with varying width in the upper levels. This is a frequency range, where in Stage 2018 opposite phase behaviour was found between detector E and the other four detectors, and hence a possible thimble tube vibration of a non-instrumented thimble tube (or that of a fuel assembly) was suspected. The interesting point is that, as the core map in Fig. 3.1 in [4] shows, similarly to detector D in the present measurements, detector E in those measurements lay somewhat separated from the rest of the detectors.

The spectra in the present Stage, although in many ways still being similar to the previous Stage, also show considerable differences. The peak at 8 Hz has increased in amplitude (relative to the other peaks), and it is also noticeably broader than in the previous Stage in all four detectors and at all levels. If this frequency corresponds to the eigenfrequency of the thimble tube vibrations (which is not known), then this would be a definite indicator of increased impacting. The peak around 6 Hz in the two lowermost positions also exists. However, it has another, much stronger singular appearance, namely in the uppermost position (Level 1, 30 cm) of the spectrum of detector A. Actually, at this level, the whole spectrum of detector A appears to be abnormally high, showing also an increased peak at 17.5 Hz.

Another difference as compared to the previous Stage is seen in the spectra of detector B. In the present Stage, at all levels, it has a rather large peak at 15 - 16 Hz, which largely exceeds the spectra of the other detectors. The other detectors have a much milder peak around 20 Hz, where detector B does not show any noticeable peaks. In the previous Stage, nearly no peaks were seen at these frequencies.

Altogether it can be claimed that there are significant changes in the spectra as compared to the previous Stage. On the other hand, similarly to the conclusions of the previous Stage, the significant peaks occur at frequencies which coincide with known vibration properties of the core barrel of the fuel assemblies, hence it is not clear how much of these can be attributed to thimble tube vibrations. One impediment for the interpretation is the lack of the knowledge of the possible eigenfrequency or eigenfrequencies of the thimble tubes and detectors. Such an information could be gained either from international experience, or from the signals of dedicated accelerometers. However, none of these are available. At any rate, the broadening of the peak at 8 Hz could be an indicator of increased impacting in all four detector positions. The increased amplitude of some peaks, or even the whole spectra, indicates that detector A may have impacting at the uppermost level, and

detector B at all levels.

2.2.2 Coherences and phases between detector pairs at the same axial elevation

As mentioned earlier, the coherence and phase data may be suitable to detect thimble tube vibrations (or vibrations of other components) in between the line of the detectors, which are aligned in columns N and L. The use of coherences and phases has also the advantage that they are totally uneffected from the lack of normalisation of the signals. Similarly to the analysis in Stages 2018 and 2020 [4, 17], since 4 detectors can be paired in 6 different ways, together with the 6 axial positions, this gives 36 different cases, whose display has to be condensed. Hence the results are shown such that several configurations are grouped together, for a more condensed representation. In Figs 2.7 and 2.8 the coherence and phase between the pairs A-B, A-C and A-D are shown for the three upper and three lower axial positions, respectively; in Figs 2.9 and 2.10 the pairs B-C, B-D and C-D , are shown for the same axial positions. These can be hence condensed into 4 figures altogether.

The coherences and phases also show noticeable differences from those in the previous stage. As a rule, the coherences are non-zero mostly in the region 1 - 8 Hz. In the previous Stage, in the coherence between detector A and the other three, there were two distinct peaks, one at around 1 Hz and another one around 8 Hz. Also a difference in the character of the coherence was found between the upper three and the lower three levels. In the present Stage, altough the coherences are different from those in the previous Stage, still there is a difference between the upper three and the lower three positions. For the upper three levels, the coherence is generally high betwee 0 - 8 Hz, the highest between the closest pairs A-C, and the lowest betweent the farthest detectors A-D, with a markedly large dip at 5 Hz. At the lower three positions, the dip disappeared, so the coherences change smoother in frequency, decreasing towards lower frequencies and with increasing distance between the detector pair. At some levels, the coherence deviates from zero even around 20 Hz.

In the pairwise coherences between detectors B - D, the tendency is similar: a dip between all three pairs at the upper three levels, and a smooth coherence with a maximum at 8 Hz, with an amplitude decreasing with decreasing frequencies. The monotonic dependence of the amplitude with increasing distance between the detectors remains.

The phase shows a more similar behaviour to phases in the previous Stage. Essentially, it is zero between all detector combinations for all axial elevations up to about 15 Hz, except between detector A and the other three around 6 Hz, especially at the uppermost level. This is the frequency where an extra peak appeared in the signal of detector A. From the dominating in-phase behaviour between all detector pairs one can draw the conclusion that thimble tube vibrations (or vibrations of other components) are unlikely between the "line of sight" of the four detectors up to 10-15 Hz.

Similarly to the results of the previous Stage, out-of-phase behaviour can be seen

Figure 2.7: Coherence and phase between the pairs A-B, A-C and A-D for the three upper axial positions.
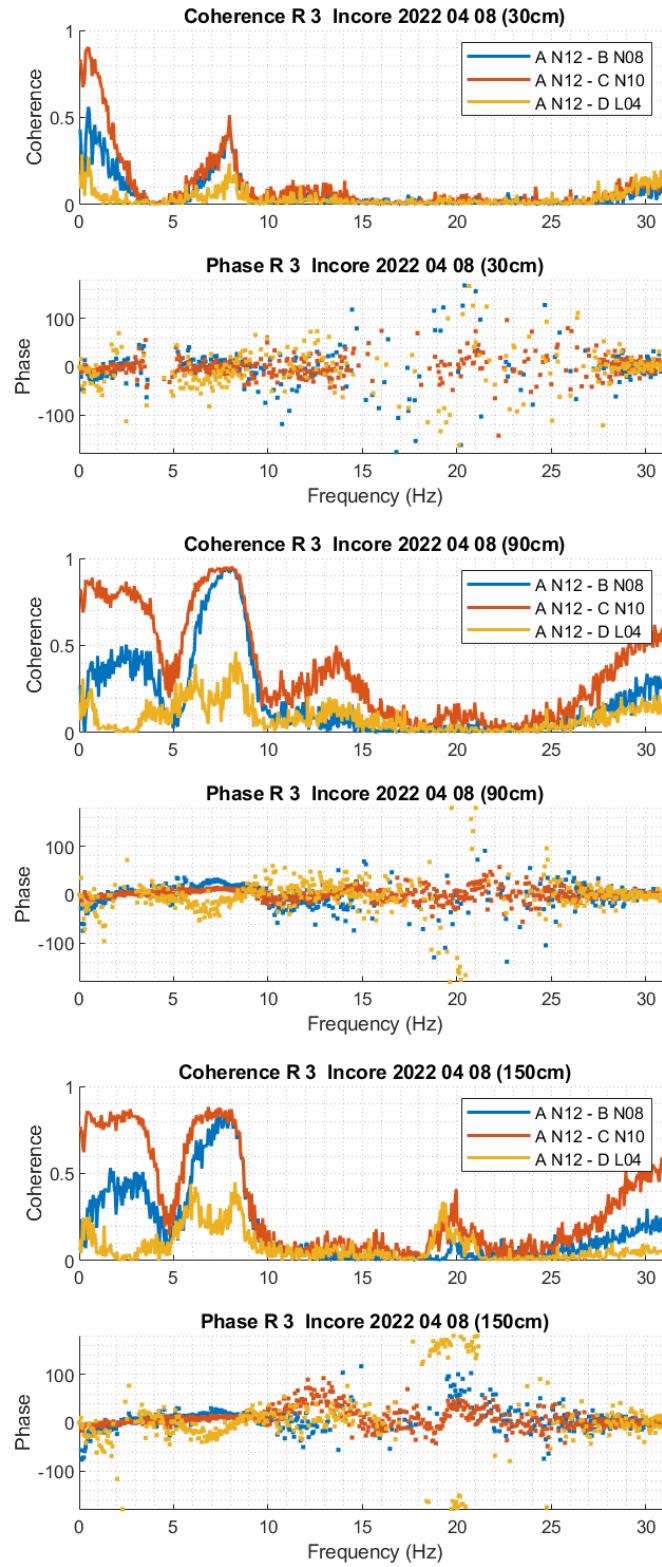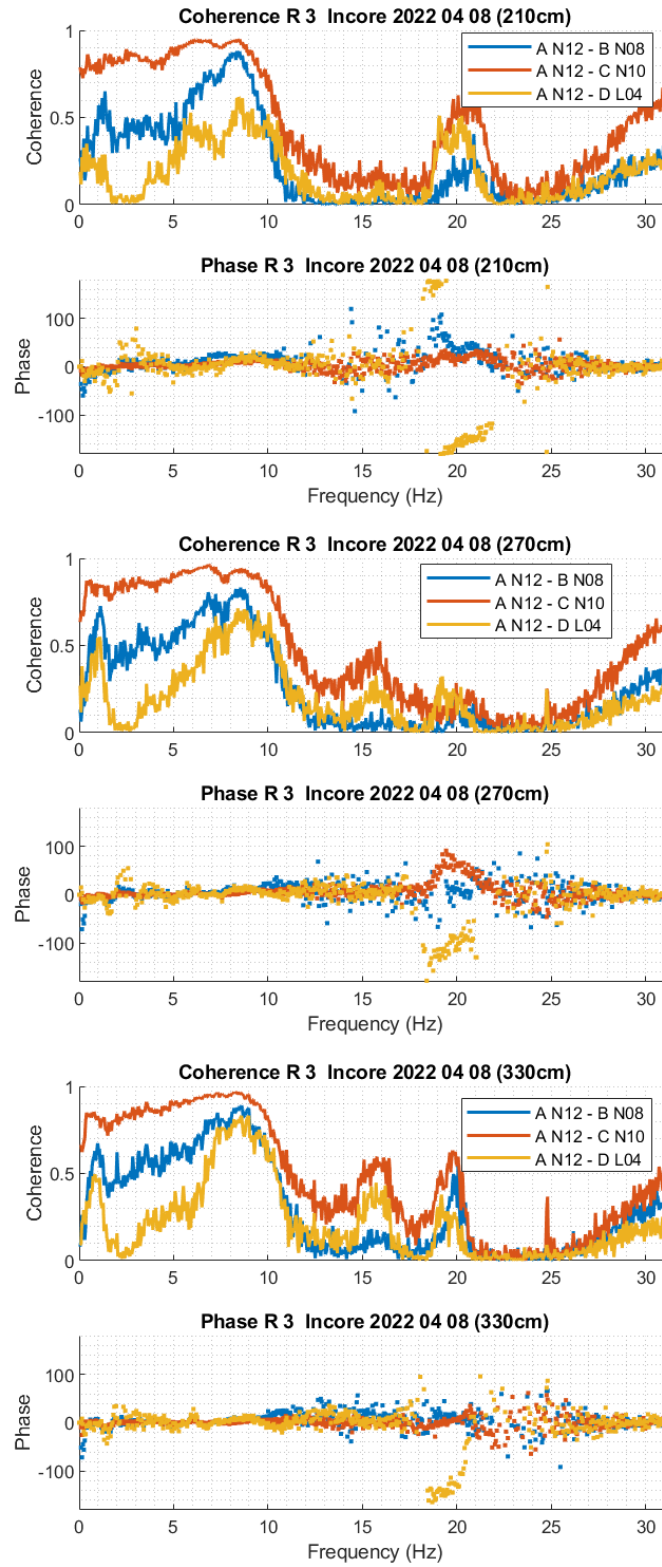
Figure 2.8: Coherence and phase between the pairs A-B, A-C and A-D for the three lower axial positions.
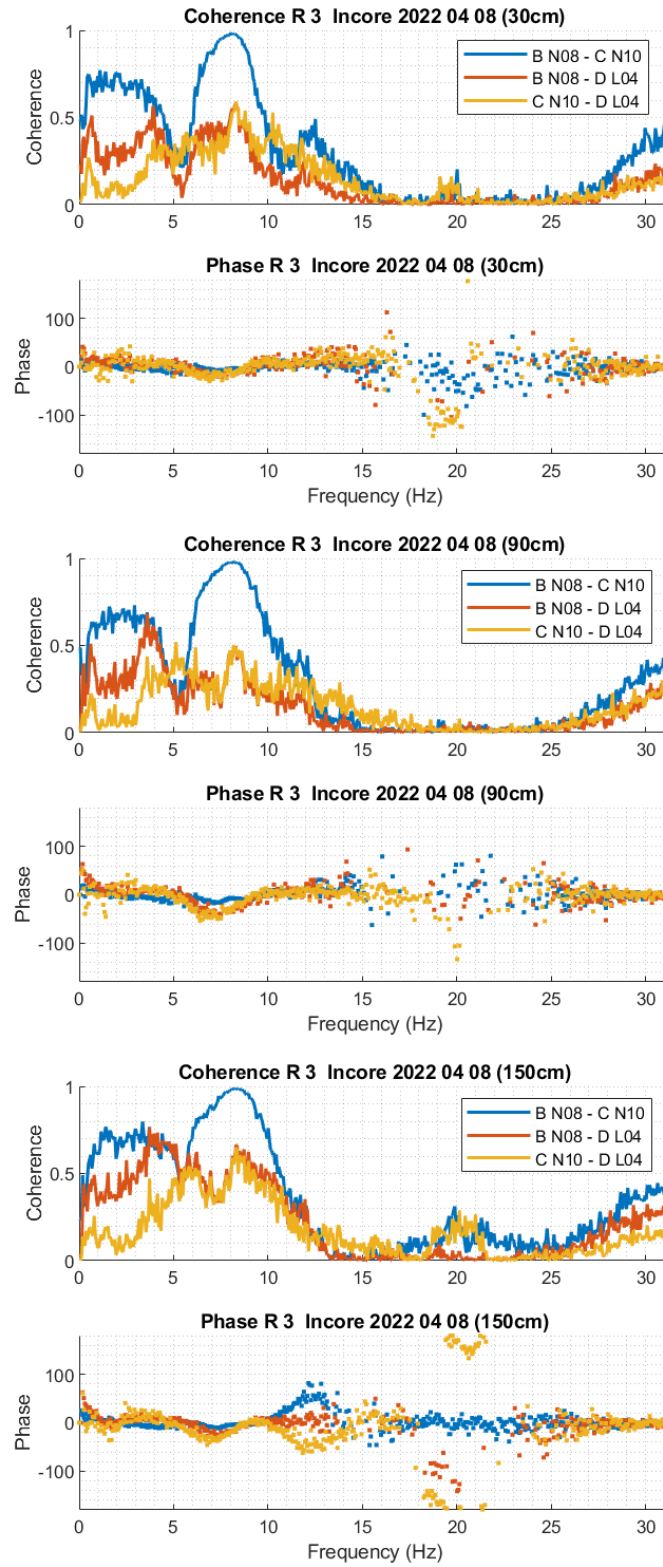
Figure 2.9: Coherence and phase between the pairs B-C, B-D and C-D for the three upper axial positions.
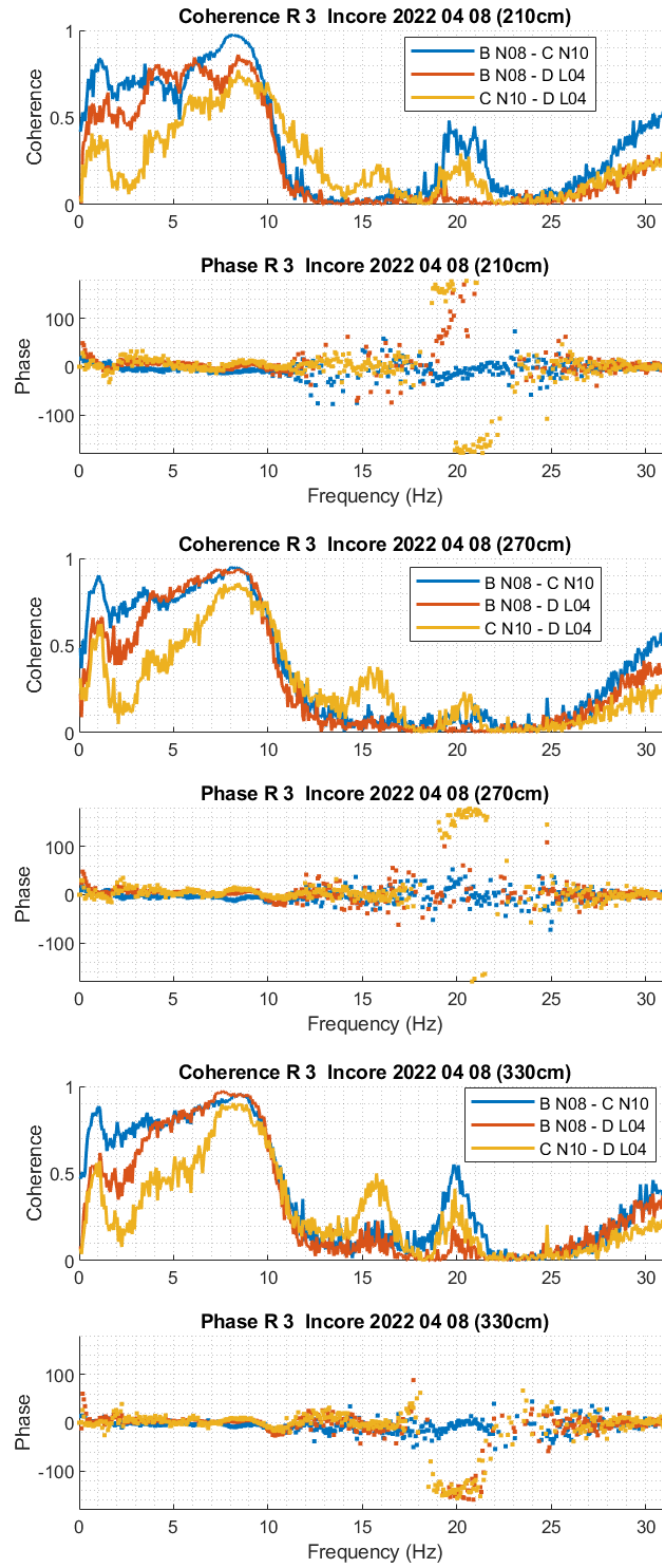
Figure 2.10: Coherence and phase between the pairs B-C, B-D and C-D for the three lower axial positions.

around 15 - 20 Hz between most detector pairs, of which the one between between A and D deviates mostly from zero at some levels. As noted in the previous Stage, it is interesting that opposite phase occurs mostly between detectors which are not neighbours; this was the case also in the 2008 measurements. This suggests that the opposite phase is not due to thimble tube vibrations, rather to the shell mode vibrations of the core barrel, which are also sensed by the inc-core detectors. In such a case detectors in different quadrants of the core should exhibit out-of-phase relationships. Nevertheless, the coherence is low in this frequency region, and the phase values also show a large scatter, so no concrete conclusion can be drawn from the out-of-phase behaviour around 20 Hz.

2.3 Evaluation of Measurement 2

This section reports on the evaluation of Measurement 2 with spectral and wavelet methods. The right hand side figure in Fig. 2.2 shows the scheme of the measurement. Measurements were taken in all four detector positions, at 21 axial levels, starting at the bottom of the core, and raising the detector in steps of 18 cm in 20 steps. As mentioned in the previous section, the measurement time in each of the 21 axial positions was only about one minute, so calculation of the power spectra in the individual positions is not feasible. Hence, two types of calculations were made for all four detectors (A - D):

- the APSD of the whole time series of the measurement in one piece;

- the continuous wavelet transform of the whole measurement.

The results are shown in Figs 2.11 - 2.14 below. Since in the measurement the detectors were moved from the bottom of the core to the top of the core, the x-axis of the top and the bottom sub-figures (time sequence and wavelet transform, respectively), corresponds to detector positions with increasing elevation from the bottom to the top. That is, in the top sub-figures, the positions are not those of the Ringhals convention, rather they show the distance from the bottom. Similarly, the left hand side of the bottom sub-figures (wavelet transforms) correspond to the detector being at the bottom of the core, and the right hand side to the top of the core.

Interpretation of the content of these results requires some care. First of all, the whole measurement series contains measurements in 21 different axial points. Although the frequency content can be expected to change smoothly as a function of the position, the amplitude of the noise depends on the axial position, as is seen visually in the top plot of each Figure. In all plots, it seems that the axial dependence of the noise amplitude has basically a cosine shape, but it is not symmetric, rather the amplitudes are higher in the upper part of the core. Further, as is also seen in these time series plots, at the time of the movement of the detector from one position to the next introduces a spike in the signal. This spike was not eliminated from the measurement before processing the data, which in some way distorts the frequency content of the noise.

The APSDs of the whole time series, with the detector being at 21 different

positions in the core, are shown in the centre plot of all four figures. Despite that the spikes were not eliminated, the APSDs look largely the same way as in Measurement 1, where longer measurements were taken in 6 different axial points. These APSDs give a kind of a feeling of the existing frequencies, although they do not tell at which time (elevation) the frequencies persist, or if they exist in all positions. This is more visible on the continuous wavelet transform ("spectrogram") of the signals, which is the lowermost plot in the figures. For instance in the signal of detector A (core position N12), it is seen that the component around 5 Hz exists only at the top of the core. This is in good agreement with the analysis of Measurement 1 in the previous section, which also showed the peak at 5 Hz only in the position 30 cm from the top of the core. A similar effect is seen in the spectrogram of detector B (core position N08), where a component around 6 - 7 Hz appears only in the uppermost positions. In the spectrogram of detectors C and D (core positions N10 and L04, respectively), some frequencies around 15 and 20 Hz appear in part of the time.

An interesting feature of the wavelet transforms is that vertical spike-like structures appear at the low frequency part, which occur approximately at the same times as the spikes of the original time signal due to the shift of the detector from one position to the next. With some extrapolation, one might associate vertical structures at other times and frequencies also with spikes of the original time signal, which are however not visible in the time signal. Assuming that these are due to impacting of the thimble tubes and/or the detector, then such occurrences could be related to thimble tube vibrations and impacting. An inspection of the spectrograms shows that such spike-like structures can be mostly seen in the wavelet transforms of detectors A and B (N12 and N08, respectively), and to a lesser extent, with detector D (L04), an finally some traces in the wavelet transform of detector C (N10). This would lead to the conclusion that detectors A and B might be exposed to thimble tube vibrations more than detectors C and D, out of the latter two D having the higher chance of impacting. This is, however, a relatively subjective and intuitive judgement.

2.4 Summary

Regarding the possible vibrations of the instrumented tubes, from the broadening of the peak at 8 Hz of the APSDs one might suspect vibrations of all detectors, and from the other spectral features, most likely for detectors A and B. This conclusion is also supported by the results of the wavelet analysis, which targets the frequency or likelihood of impacting, and not the vibrations.

From the coherences and phases one can draw the conclusion that no evidence supports the existence of thimble tube vibrations in the non-instrumented (i.e. detector-free) positions. This is not a proof of the absence of such vibrations or impacting, rather a statement on the possibilities of the diagnostics. The out-of-phase behaviour at 15 - 20 Hz could be an indicator of such vibrations, but those frequencies are probably above the eigenfrequencies of thimble tube vibrations.

Any differences between results from the previous Stage, apart from changes in thimble-tube vibrations, might be attributed to the fact that positions A-C have been occupied by different fuel-assembly types in different burnup regimes for the
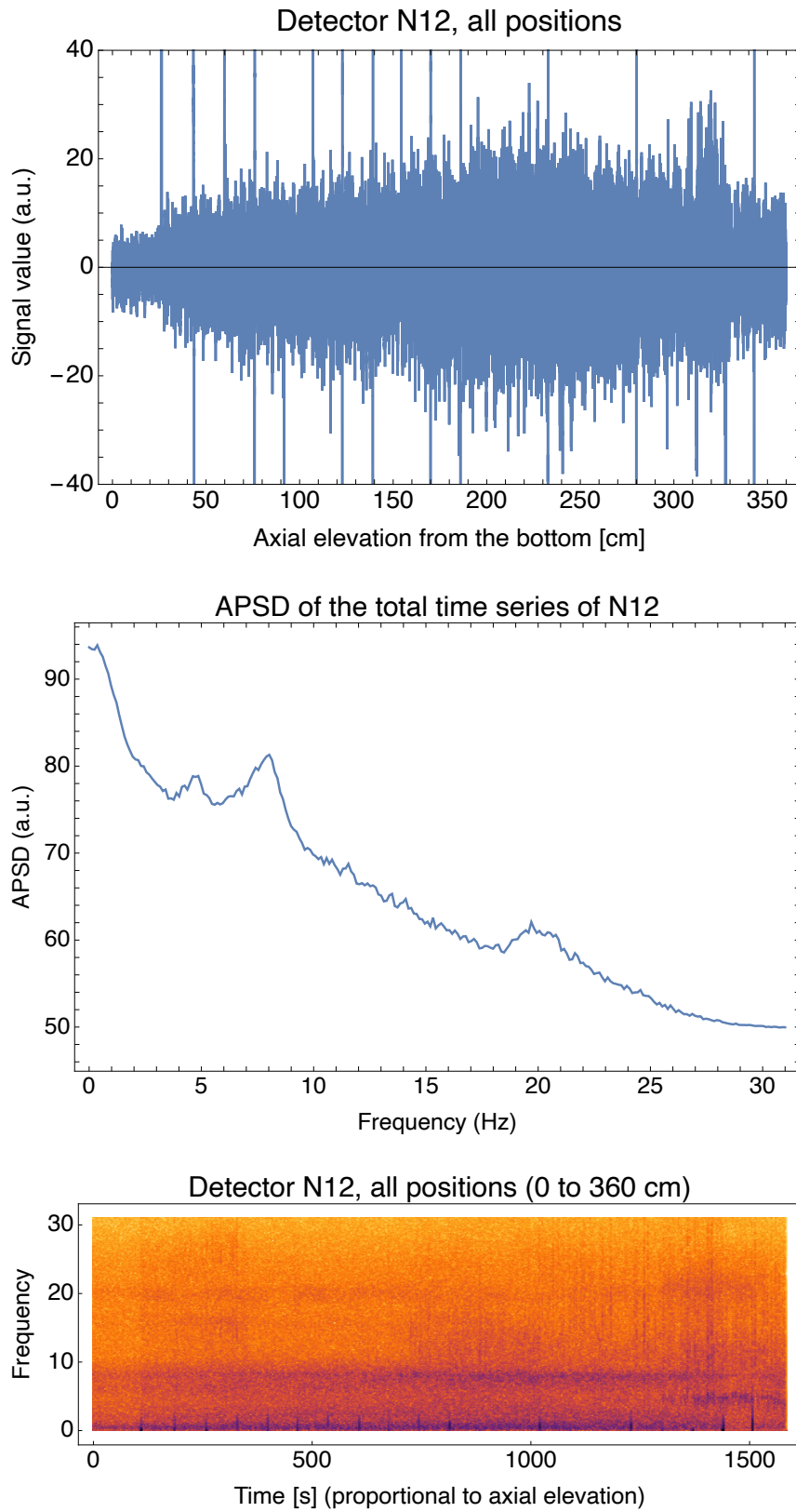
Figure 2.11: Evaluation of the moving measurement for detector A, core position N12. Top: the time series signal. Centre: the APSD calculated from the total signal. Bottom: the continuous wavelet transform of the signal.
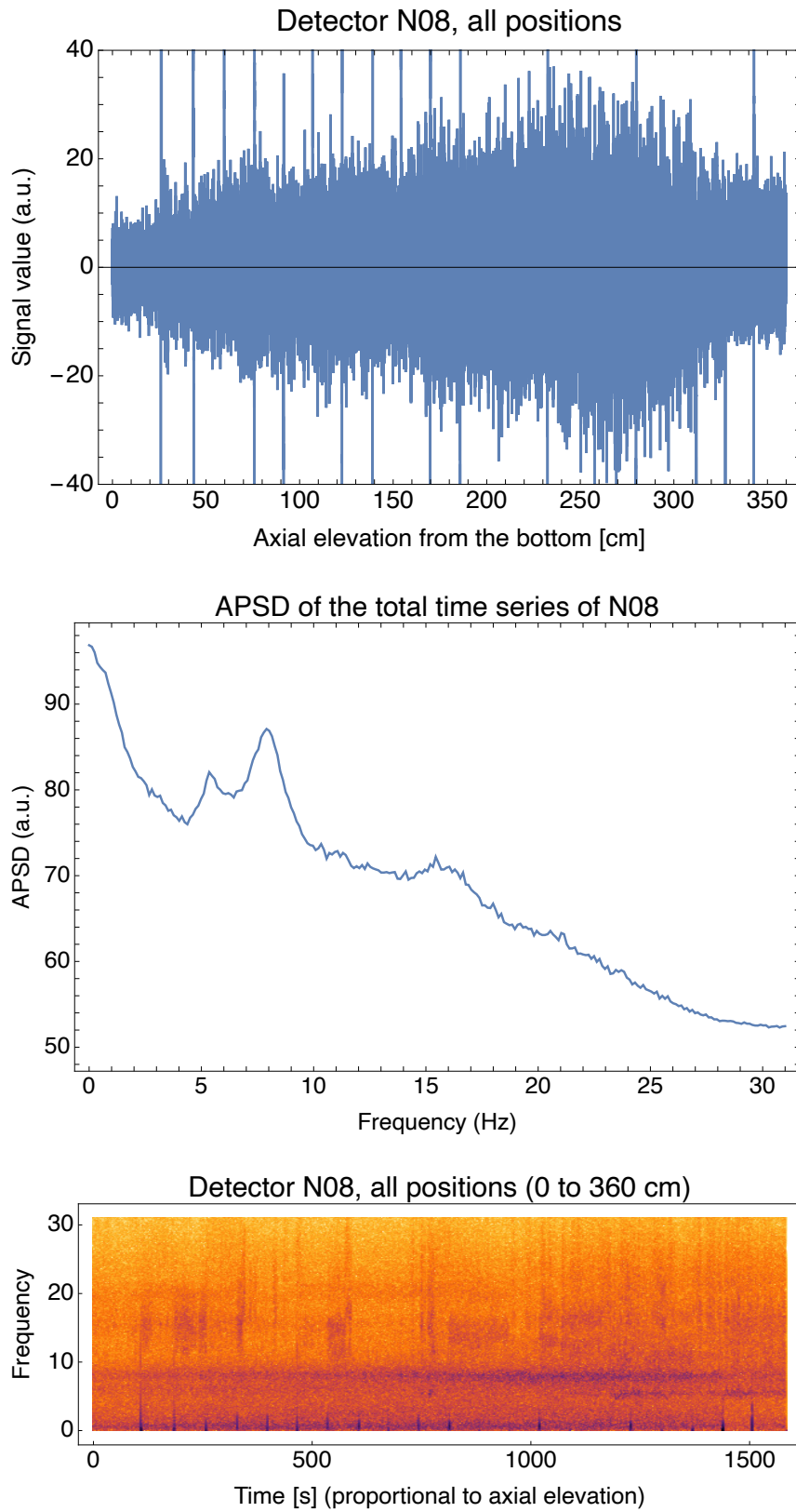
Figure 2.12: Evaluation of the moving measurement for detector B, core position N08. Top: the time series signal. Centre: the APSD calculated from the total signal. Bottom: the continuous wavelet transform of the signal.
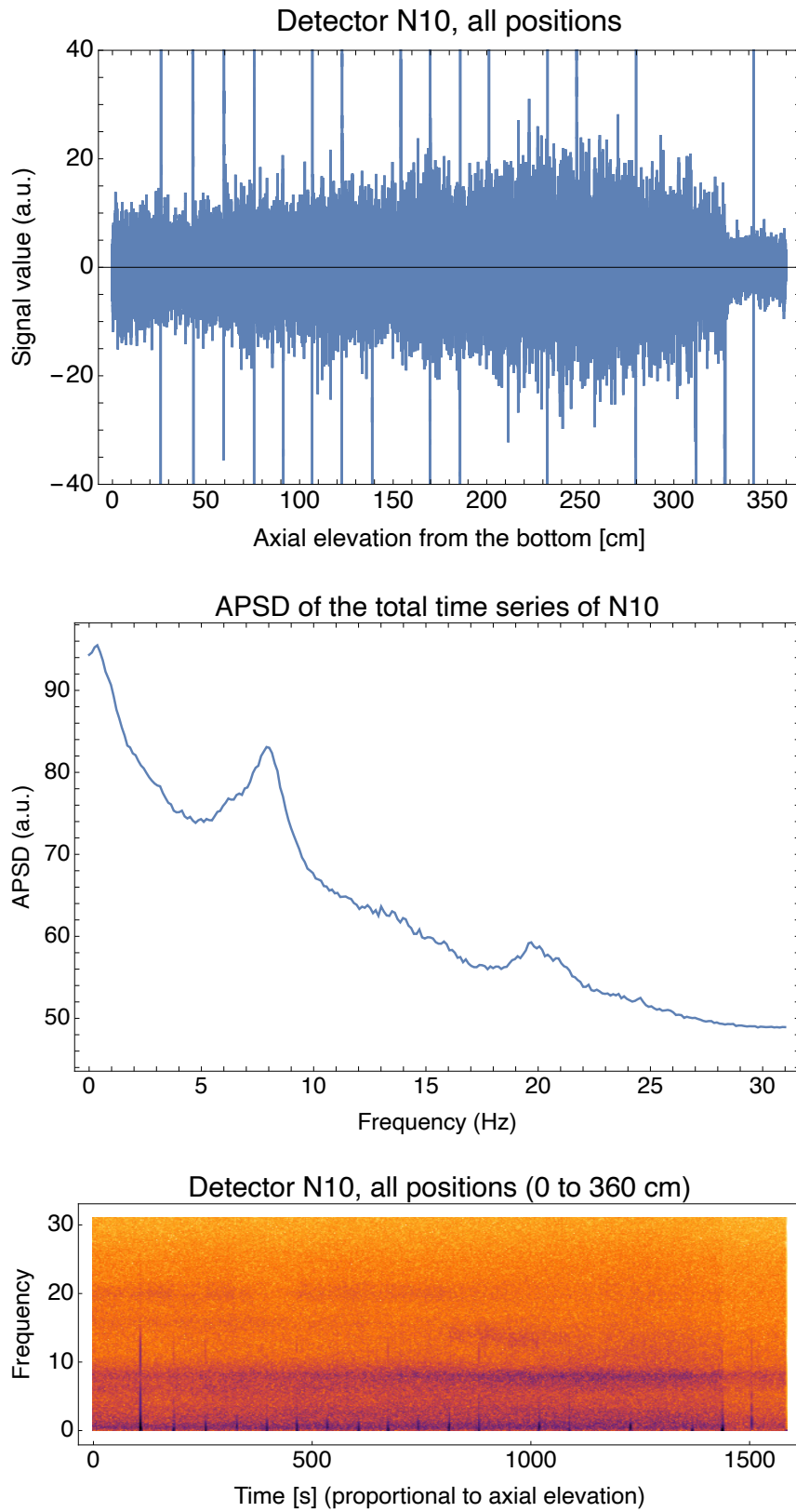
Figure 2.13: Evaluation of the moving measurement for detector C, core position N10. Top: the time series signal. Centre: the APSD calculated from the total signal. Bottom: the continuous wavelet transform of the signal.
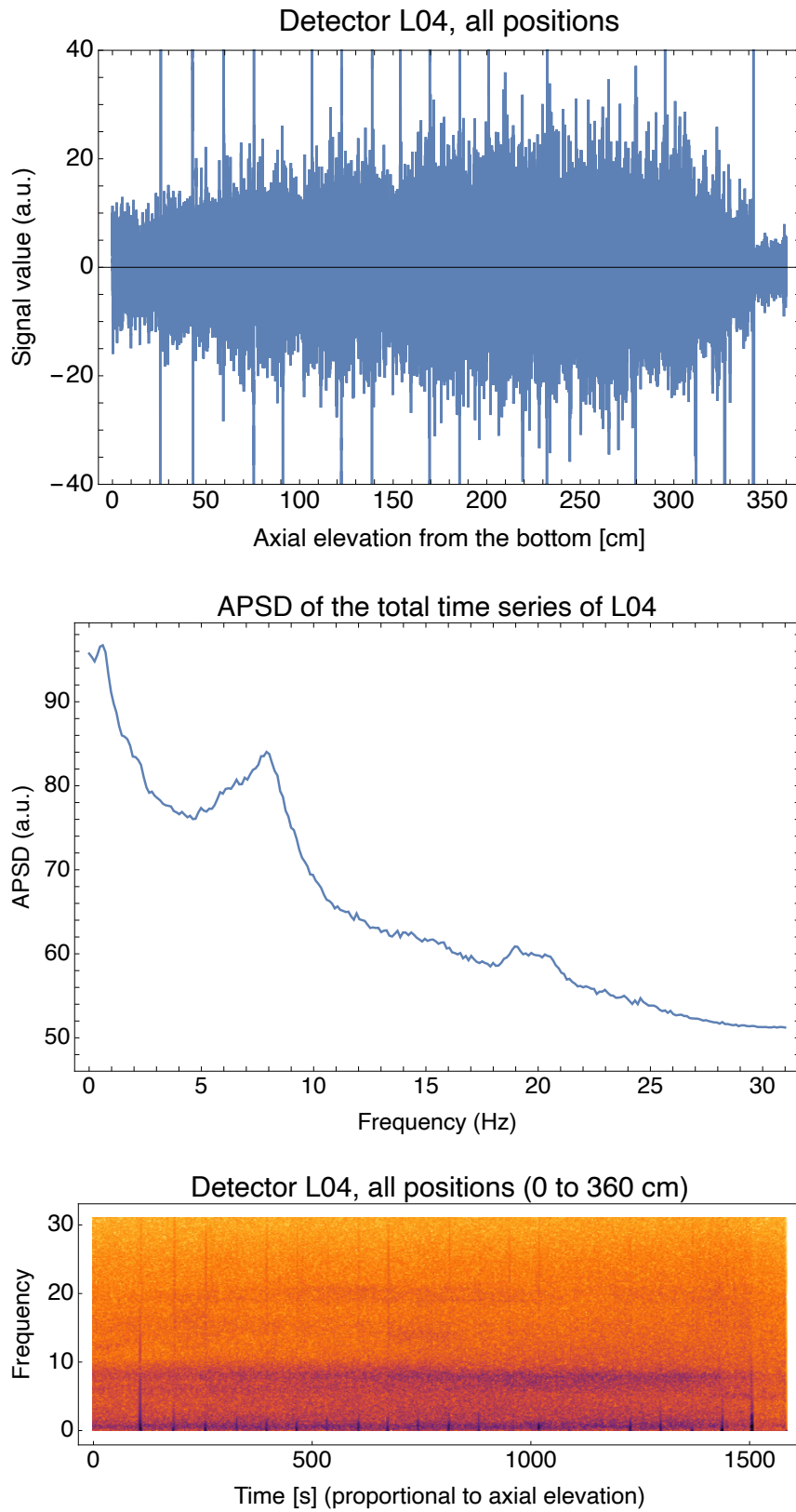
Figure 2.14: Evaluation of the moving measurement for detector D, core position L04. Top: the time series signal. Centre: the APSD calculated from the total signal. Bottom: the continuous wavelet transform of the signal.

two consecutive cycles investigated. According to the results from the thimble-tube inspections during the outage in 2022, no significant increase in TT-wear between cycle 38, and the most recent cycle 39, could be identified.

The analysis and the discussion above suggests that one has a larger chance to detect vibrations in the thimble tube positions which contain a detector. Therefore one might consider making a bigger campaign and making measurements in all thimble tube positions. The use of accelerometers, as is described in [3], could also be considered, which would largely enhance the understanding of the characteristics of thimble tube vibrations and hence would increase the performance of the methods of detecting thimble tube vibrations and impacting.

3. EVALUATION OF NEW EX-CORE MEASUREMENTS FOR BEAM, REACTIVITY, SHELL AND TILTING MODE VIBRATIONS IN R3

3.1 Introduction and background

The analysis of core-barrel vibration properties (often abbreviated to CBM, core barrel motion) have been the subject of study both in Sweden and internationally. It has also been the subject of the collaboration between Chalmers and Ringhals from the beginning, as it was reported in several previous Stages in the Ringhals diagnostic project [18, 19, 20, 21, 9, 10, 16, 22, 23, 24, 25, 4, 26, 17].

Within the last decade, a series of studies dedicated to core barrel vibrations have been performed in order to analyse and find a suitable explanation for the recent observations of wear at both the lower and upper core-barrel-support structures, i.e. the lower radial key and the reactor vessel alignment pins in the Ringhals PWRs. In the last few years the main focus in this area was put on the investigation of a double peak observed in the Auto Power Spectral Density (APSD) in the frequency region of the beam mode component, mostly in measurements made in R4. A hypothesis was formulated about the nature of this peak, where it was suggested that the lower frequency peak is due to the beam mode vibrations and the upper peak is due to fuel assembly vibrations. A test of this hypothesis was one of the main targets of the analysis. A key factor of the analysis was to assume that the lower frequency peak is due to the (coherent) vibrations of the whole core barrel, hence the symmetries between the ex-core detectors could be used to enhance the effect, as well as to condense the quantification to one single parameter by taking combinations of the detector signals. However, since the higher frequency mode was assumed to be due to the effect of the independent (incoherent) vibrations of the individual fuel assemblies, no symmetries could be utilised, and the results could not be condensed into one single parameter.

In 2014 a further, new assumption was made, in that the main effect of the individual vibrations manifests itself through the combined reactivity effect of all the individually vibrating fuel assemblies. This assumption, through the associated symmetries of the reactivity component, allowed to condense the analysis of the different detector signals into one single parameter even for the higher frequency peak. This hypothesis was tested with a positive outcome on the measurements taken at Ringhals-4. In addition, although no double peak was visible in the APSDs of the R3 measurements, with the peak separation and curve fitting technique, the two peaks could be separated even in the R3 measurements. Thus, finally, it became possible to distinguish between the beam mode component due to core barrel vibrations and the reactivity component associated to the single fuel assembly vibrations. In addition, through numerical simulations, it was also possible to confirm the constant amplitude within one fuel cycle for the beam mode component, and the varying amplitude (within one cycle) of the reactivity component (individual fuel assembly vibrations), which were in good agreement with the original hypothesis.

The work in the continuation was therefore not concentrated any longer to the test and proof of the hypothesis, and the associated trend analysis of the evolution of the peak amplitudes during the cycle, rather on checking whether there is any major change in the amplitude and frequency of the beam mode peaks, as compared to the previous measurements, which could indicate an increased play in the lower radial key support. A special circumstance in this aspect is that in 2015, the total power of Ringhals-4 was increased by 18.6 %. Another aspect is that some structural changes took place in R4. The hold-down springs were replaced during the outage in 2013, and the interior parts were lifted out during the outage in 2014 for an inspection. As it was seen and reported in the previous Stages [25, 4], this has changed the shape of the spectra around the beam mode frequency such that the visibility of the former double peak has ceased and only one peak could be observed visually. As the results of the previous Stage showed, by this change, the ex-core neutron spectra became very similar between R3 and R4.

Lastly, as it was described in the previous Stages [24, 25, 4, 26, 17], a new type of pivotal vibration mode, which we named as "tilting" or "wobbling" mode, was discovered. The separation of the tilting mode from the other components is made with methods similar to the other mode separation methods with adding and subtracting the signals in various combinations. The only difference is that for the separation of the tilting mode from the other components, all 8 detectors (the four ex-core detectors at two axial elevations) need to be used. Hence in the routine analysis, the separation of all four components (beam, shell, reactivity and tilting modes) has been made in the continuation.

In the previous three Stages (2018-19, 2019-20 and 2020-21), the ex-core measurements were made in R3. Since in the years preceding 2018, the ex-core measurements were performed in R4, in Stage 2018 there was no possibility to compare the new measurements with immediately previous ones taken in R3. It has to be added that there were measurements made in the first half of 2018, but a detailed evaluation and analysis of those measurements was not included either in Stage 2016-2017 or in Stage 2018-19 (there was a gap between Stages 2016 and 2018). Hence in Stage 2018, the structure of the spectra could not be compared with immediate past measurements, and no long-term trend analysis was presented. One could only note that unlike in the previous R4 measurements, the double peak at 8 Hz could not be seen in the spectra, they could only be separated by a refined curve fitting procedure. The within-cycle trend analysis showed that the two modes around 8 Hz behaved practically the same way within the cycle, which was another difference compared to the previous R4 measurements.

In Stages 2019 and 2020, the ex-core measurements were made again in R3, which gave a possibility to compare the measurements with those of Stage 2018. It was found that both the structure of the peaks in the APSDs, the coherences and phases, as well as the within-cycle trend analysis, showed a considerable resemblance between those three stages, i.e. both Modes around 7-8 Hz, which cannot be separated by visual inspection in the spectra, only by the mode separation technique, change similarly during the cycle. Since 2019, it was also possible to perform a long term analysis with results from two and three cycles, respectively with the

amplitudes of the beam mode and reactivity mode.

In the present Stage the ex-core measurements were made yet again in R3, which now lends the possibility to an even longer long term trend analysis. Here it has to be noted that during the outage/refuelling between Stage 2019 and 2020, and upflow conversion was performed, in order to decrease the possibility of baffle jetting. This is also the reason why no analysis of the in-core measurements concerning baffle jetting was performed since then. The upflow conversion affected the measurement results alreay in the previous Stage, but in that Stage, due to the Covid-19 situation, only 2 ex-core measurements were performed. This affected primarily the in-cycle trend analysis, but to some extent even the long-term trend analysis. However, in the present stage, three ex-core measurements were made again, making both the short-term and long-term trend analysis more effective.

Summarising the results of the analysis described below, one can say that the structure of the spectra, and the character of the in-cycle trend analysis, are again very similar to those of the two preceding Stages. The long-term trend, however, shows that the long-term increase of the vibration components, i.e. that of the beam mode and the reactivity component, is stopped, and the amplitudes in this year are lower than for the preceding Stage for the beam mode, and even lower than the preceding two Stages for the reactivity component. The long-term trend indicates that the upflow conversion might have had a beneficial effect on the magnitude of the vibrations, whereas the structure of the spectra shows that no significant qualitative change of the vibration properties can be noted.

3.2 Details of the measurements in R3

Three sets of measurements were analysed. The measurements were performed in R3 in cycle 39, on 21 December 2021, 30 March 2022 and 12 May 2022. For simplicity, as in the previous reports, they will be referred to as Measurements 1, 2 and 3, respectively. The sampling frequency was 62.5 Hz for all three sets of measurements. The detectors used and the registered quantities (static and fluctuating parts, i.e. DC and AC, respectively) are shown in Table 3.1. More detailed data regarding settings and general parameters can be found in the measurement protocols from previous measurements, which were performed in an identical manner [27, 28, 29].

3.3 Analysis of the measurements made on 2021-12-21 (Measurement 1)

3.3.1 Individual spectra of all detectors

In summary, it can be stated that what regards the peak structure of the spectra, the results of the present Stage are in a good agreement with those in the previous three Stages. There are certain smaller deviations, but they do not bear much significance, and they are not bigger than the variations between the spectra of the previous three Stages. However, several of the amplitudes of the known peaks changed as compared to the previous Stages. This concerns the amplitudes of the beam mode and the tilting mode, as well as the long-term trend, as it will be shown and discussed later. These changes are consistent with each other, and they may be

Table 3.1: The measurement data structure of the three measurements in Ringhals 3 during 2021-22.

Channel	Measurement point
0	Time
1	N41U DC
2	N42U DC
3	N43U DC
4	N44U DC
5	N41L DC
6	N42L DC
7	N43L DC
8	N44L DC
9	N41U AC
10	N42U AC
11	N43U AC
12	N44U AC
13	N41L AC
14	N42L AC
15	N43L AC
16	N44L AC

attributed to the upflow conversion.

The APSDs of all eight individual detector signals are shown in Fig. 3.1. They are rather similar to those from the previous three Stages. All signals show the two familiar peaks around 8 and 20 Hz for the beam and shell modes, respectively. Similarly to the previous measurements made in R3, as well as in the latest measurements in R4, no double peak is visible at 8 Hz. Rather, similarly to the three previous measurements, a small peak is visible around 6 Hz in most, but not all detector spectra, i.e. it is more separated from the 8 Hz peak in frequency. Another similarity is that the peak at 20 Hz seems to have a small second hump in all signals.

Similarly to the previous three Stages, the two peaks that we earlier identified with the beam mode and the reactivity mode (the latter corresponding to the noise induced by the individual fuel assembly vibrations) and which were seen in older measurements, cannot now be visibly separated. As also mentioned in the previous Stages, after the replacement of the hold-down springs in R4 during the outage in 2013, and lifting out the interior parts during the outage in 2014 for an inspection, the ex-core detector spectra in R4 and R3 look now rather similar. The mode separation is therefore essentially utilizes the separation of the signal into reactivity and beam mode spectra (together with the shell and tilted mode), and use the main peak of the two separated modes.

One visible new feature, compared to the previous Stages, is that the amplitude of the 8 Hz peak in the spectra of both N44U and N44L is visibly smaller than before. These two peaks where somewhat lower and separated from the peaks of the other three detectors already in the previous measurementrs, but the separation between the two N44 and other detectors is now much more distinct.

3.3.2 Results of the mode separation

The beam mode, shell mode, reactivity component and the tilting modes were separated according to the detector signal combination principles as in the previous work. In order to have compatibility between the measurements for different cycles, in the evaluations the fluctuating part of the signals is normalised to the their mean values. This means that e.g. the autospectra, calculated from the AC components are divided by the square of the corresponding DC signal. This makes the measurements independent of the local static power levels for the different measurements, and guarantees the validity of the long term trend analysis, where measurement data from the different cycles are compared.

The results are shown for both the upper and the lower detectors in Fig. 3.2. The results of the separation are rather similar for the two cases, as well as to those of the previous three Stages. For instance, the peculiarity, observed in the previous two Stages still exists, namely that the shell mode, which shows only a small peak at 8 Hz in the upper detectors signals (which is expected) has a quite distinct peak at 8 Hz in the lower detector signals (not expected). The peak in the lower detector signals is though not as spectacularly high as in the previous Stage. Like in the previous two stages, we have no explanation of this fact, but it seems to be consistently present in the last four Stages (including the present one).
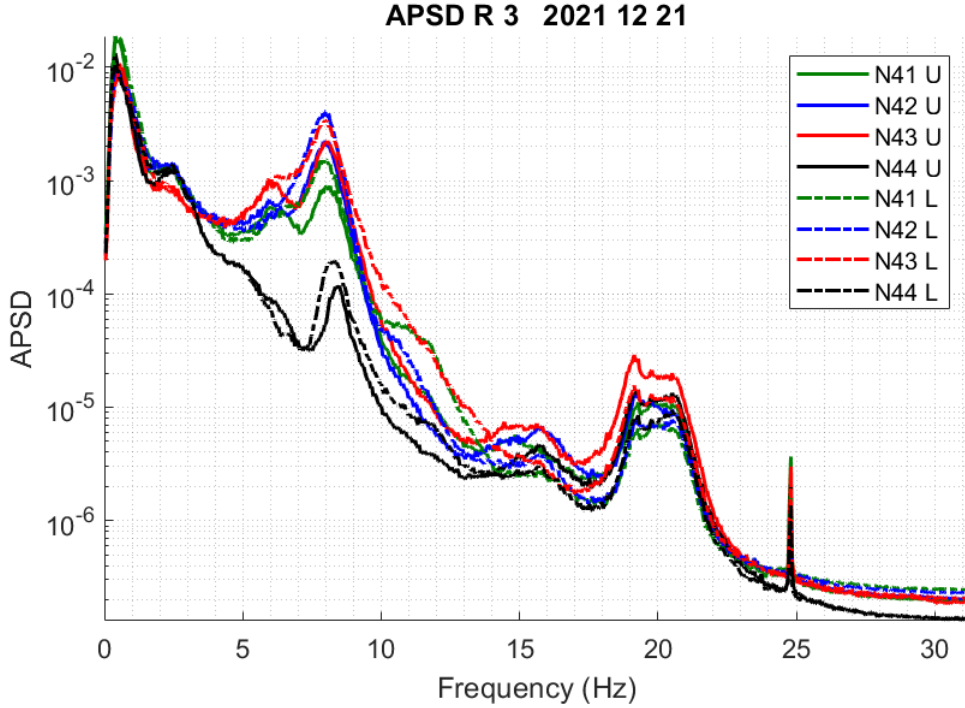
Figure 3.1: APSDs of all 8 ex-core detector signals from Measurement 1
.

It is also seen that the amplitude of the beam mode is still larger for the lower detectors, as has been the case in all previous measurements and which is expected, whereas the amplitude of most of the other components is very similar for the upper and lower detectors. The only exception is the "real" shell mode, i.e. the shell mode at 20 Hz, whose amplitude is considerably higher for the upper detectors. Similarly to the previous Stage, the difference between the upper and lower beam mode peak amplitudes is smaller than in Stages 2018 and 2019. This further confirms that this decrease of the difference between the upper and lower beam modes can most likely be attributed to the effect of the upflow conversion. Possibly the increase of the shell mode peak in the upper detectors as compared to the lower ones is also due to the upflow conversion.

Yet another new observation is that similarly to the previous Stage (2020), the amplitude of the tilted mode, both in the upper and lower detectors, has increased as compared to its value in the preceding two Stages (2018 and 2019). In the previous Stage, these peaks were actually larger than any of the other modes in both the upper and in the lower detector signals. These peaks are still large in the present analysis, although now they are not the largest out of all peaks. The largeness of the tilted mode peaks is most likely again an effect of the upflow conversion. On the other hand, the tilted mode has now two peaks; apart from the main peak at 8 Hz, there is another, almost as large peak, at around 6 Hz. This side-peak was present also in the previous Stage, but with a much smaller amplitude.

Similarly to the results of Stage 2016 [25], reporting on measurements made in R4, as well as Stages 2018 [4], 2019 [26] and 2020 [17], (all three in R3), one notes a small peak around 15.5 Hz in both the upper and the lower detector signals
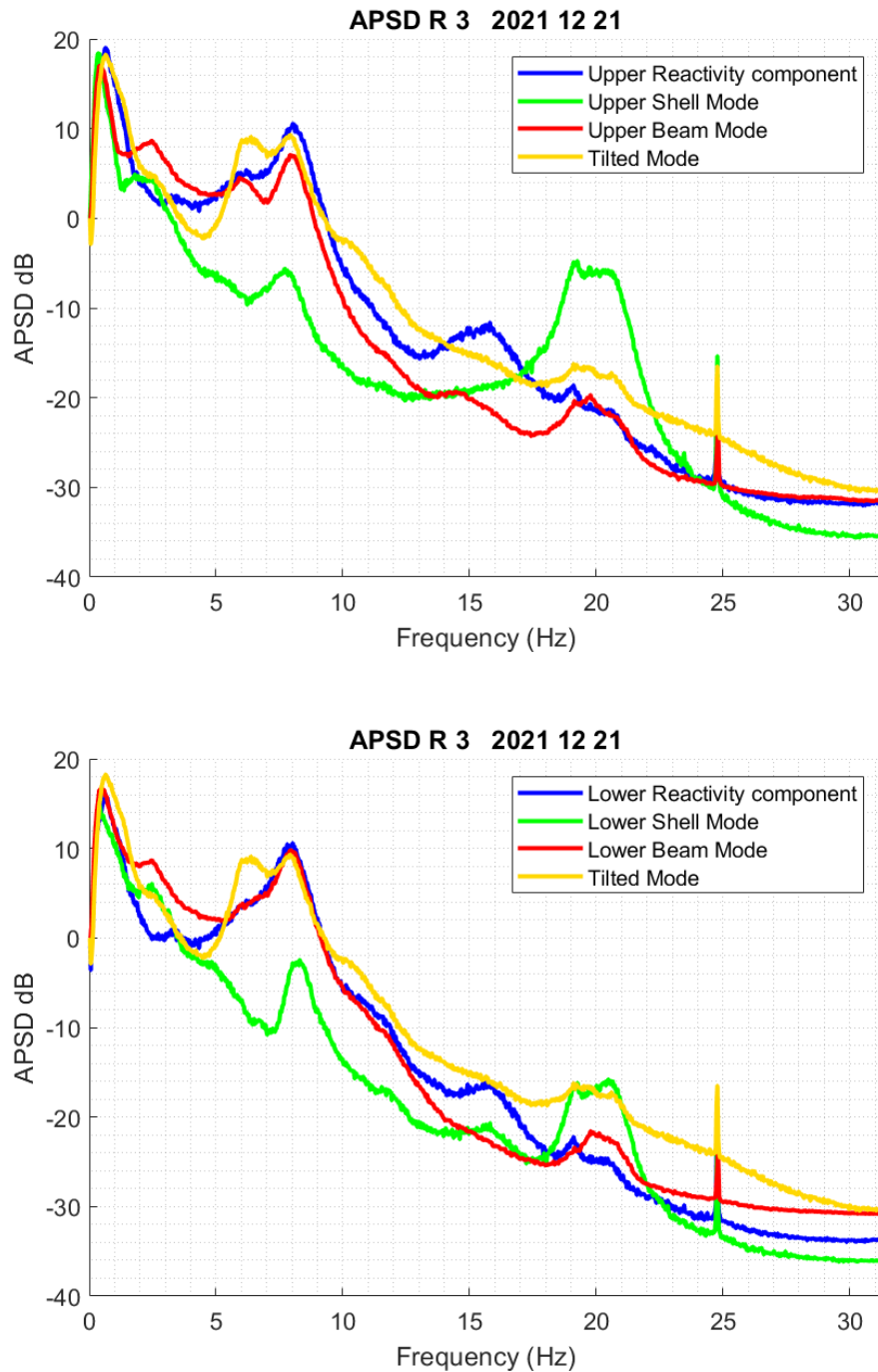
Figure 3.2: APSDs of the beam mode, shell mode, reactivity component and the tilting mode for the upper detectors (upper figure) and the lower detectors (lower figure), extracted from Measurement 1.

in the reactivity component. In Stage 2016 our interpretation was that since this frequency is about twice that of the pendular fuel vibration frequency at 8 Hz, which is also identified as a reactivity effect, the peak at 16 Hz can be attributed to the higher harmonics of the fuel assembly vibrations at the fundamental frequency 8 Hz. However, based on the analysis of the baffle jet effect in Stage 2018, in the previous Stage our judgement was that it is more likely that this peak is due to the "core

flowering" effect, i.e. the zeroth azimuthal mode of the core barrel. This judgement still holds for the present measurements.

A rocking mode of the reactor pressure vessel (RPV) may also be expected around 17 - 19 Hz [30]. For symmetry reasons, it is reasonable that any contribution from the rocking mode is enhanced in the beam-mode components, displayed in Figs. 3.2, 3.7 and 3.12. However, in the present measurements, similarly to the previous Stage, there are no noticeable peaks in this frequency region. Hence no clear indications of the RPV rocking mode can be observed.

3.3.3 Phase and coherence relationships between the upper and lower detectors

An analysis of the coherence and the phase relationships between detectors at the same and different axial levels was performed, similarly to that in the previous stages. The coherence and phase between the diagonally opposite detectors N41 and N42, for both the same and different axial levels, is shown in Fig. 3.3, and the same for detectors N43 and N44 in Fig. 3.4. The coherence and phase between the upper and lower detectors at the same radial position, for all four detectors, is shown in Fig. 3.5.

Figure 3.3:   The coherence and the phase of the CPSD calculated for the N41U-N42U, N41U-N42L, N41L-N42L and N42U-N41L detector pairs in Measurement 1.

When comparing these results with the previous three Stages, it has to be noted that there were some differences observed between these too, notably between Stages 2019 and 2020. The present results are in agreement with the previous ones for the cases when those agreed with each other. On the other hand, in the case when the results differed between 2019 and 2020, the new results agree with those in 2019,

i.e. not the immediate previous Stage (2020).

In both Stages 2018 and 2019, for the detector pair N41 - N42, (Fig. 3.3 in the present report), the coherence was similar, but this differed from the previous R4 patterns. Unlike in the R4 measurements, the coherence around 8 Hz was very low, with a medium large peak around 4 Hz. This was somewhat surprising, given the fact that the APSD peaks are the highest in this frequency region, and the phase is rather solidly 180° (as expected for the beam mode vibrations), without much scatter, up to about 8 Hz, where it shifts to zero.

However, in Stage 2020, the coherence looked different around and below 8 Hz, becoming similar to the old R4 results. Although it was still not as high as at 20 Hz, the coherence increased between 3 - 8 Hz, and it was noticeably higher around 8 Hz than in the previous two Stages.

In the previous two Stages it was surmised that a possible explanation of the low coherence at 8 Hz was that the beam mode vibrations were highly anisotropic, and are perpendicular to the line connecting the detectors N41 - N42, or if there was an interference between the beam mode, the reactivity mode and the tilting mode. If the previous arguments are valid, then it means that the beam mode vibrations in Stage 2020 were more isotropic, and there was less interference between the various components. As it was also mentioned, the amplitude of the tilted mode has increased, which might have a reason which is in common with the increase of the coherence.

In the present Stage, the behaviour of the coherence is more similar to that in Stages 2018 and 2019 in that it is again very low at 8 Hz, showing a medium large peak around 3-4 Hz. In this respect the behaviour of the coherence in Stage 2020 appears to be an exception. The likely explanation of the low coherence between N41 - N42 is the same as for Stages 2018 and 2019, an anisotropic motion of the core barrel, with a preferred direction perpendicular to the line between N41 - N42.

What regards the phase, its behaviour is more consistent between all Stages. The behaviour of the phase was similar for all three Stages 2018 - 2020. This was in line with the previous R4 measurements, and also with the expectation that just below 8 Hz the beam mode vibrations dominate, which is the cause of the out-of-phase behaviour, after which, at a slightly higher frequency, the reactivity effect of the fuel assembly vibrations take over, which is the cause of the zero phase above 8 Hz. The same behaviour is observed in the present Stage, as the lower part of Fig. 3.3 shows.

As in the preceding two Stages, the picture is rather different for the detector pairs N43 - N44, Fig. 3.4, compared to the pairs N41 - N42. The results are similar both to the previous three R3 Stages and to the former R4 measurements, in that the coherence is much larger at the low frequency range up to 8 Hz than for N41 - N42, more corresponding to the expectations. The coherence is high for all four pair combinations, similarly to Stages 2019 and 2020, whereas in Stage 2018, it was only high for two of the four possible detector combinations. There is a deep dip in the coherence around 7 Hz in all four detector combinations, and this differs from the three previous stages in one way or another. Partly, in the previous three stages,
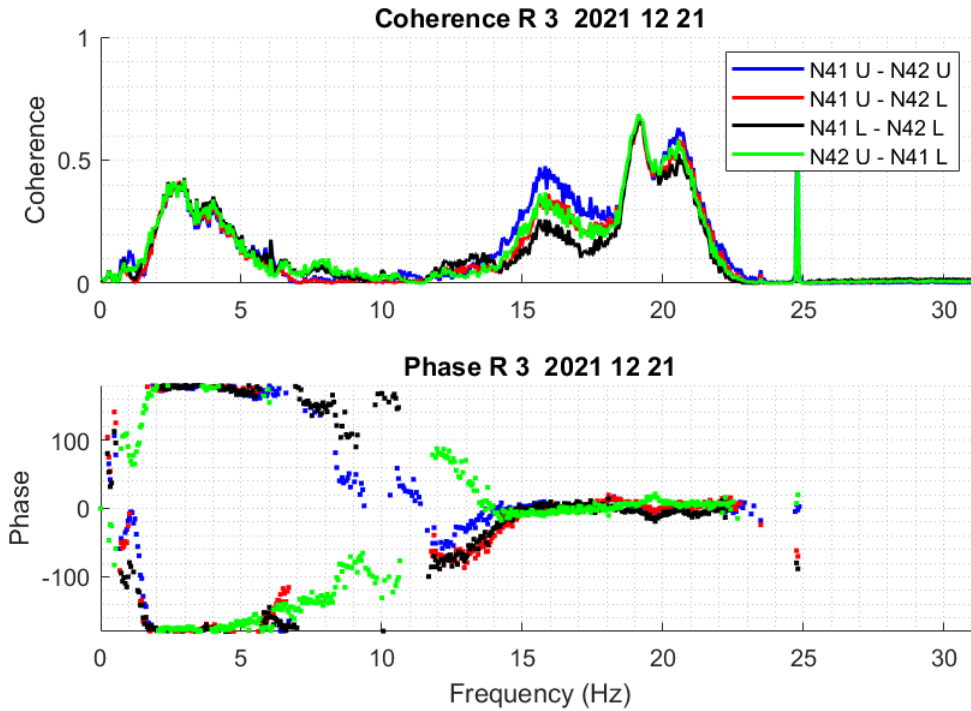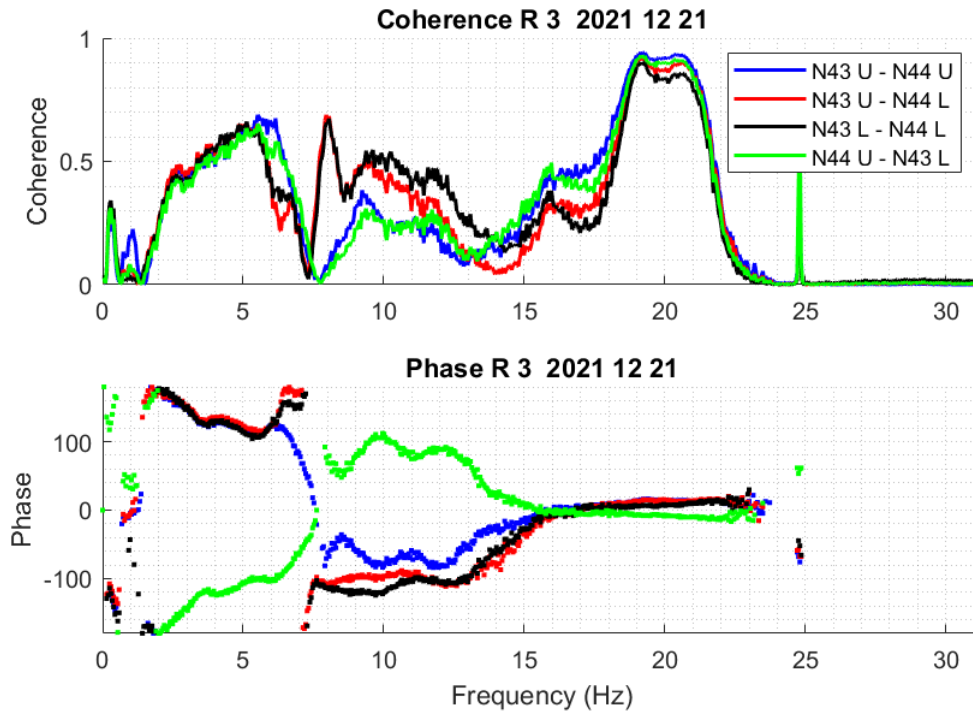
Figure 3.4:   The coherence and the phase of the CPSD calculated for the N43U-N44U, N43U-N44L, N43L-N44L and N44U-N43L detector pairs in Measurement 1.
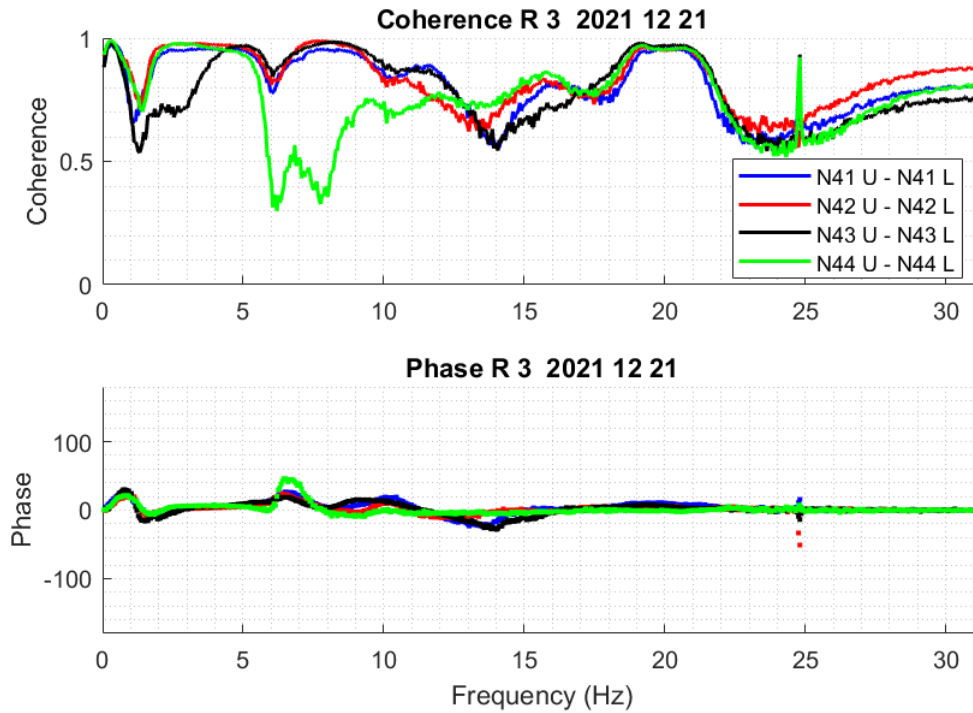

Figure 3.5:   The coherence and the phase of the CPSD calculated for the N41U-N41L, N42U-N42L, N43U-N43L and N44U-N44L detector pairs in Measurement 1.

the dip was found only in the signals of the pairs N43U - N44L and N43L - N44L, whereas now it is found in all four combinations. The dip was relatively shallow in 2018 and 2019, and got deeper in Stage 2020. In the present Stage, it is still deep, but now for all four detector pairs. The origin of this dip is still not known, but it seems that this is a systematic change, showing a tendency of becoming a more significant change.

The phase behaviour also resembles to that in the previous Stage, in that for the combinations N43U-N44U and N44U-N43L, it shows the same out-of-phase behaviour as for the detectors N41 and N42 over the whole frequency region of interest (0 to 8 Hz), whereas for the other two pairs it changes continuously from 180° to -180° with increasing frequencies, although this tendency is less pronounced in the present Stage.

As discussed in the previous reports, this type of shifting (not constant) phase behaviour is unknown from previous measurements, and it is rather difficult to interpret in the context of core barrel vibrations. A linear phase between two detectors is an indicator of a (deterministic) time delay between the two signals, which is hardly conceivable for the ex-core detector signals induced by vibrations. One cannot exclude though the possibility that the vibrations are periodic and not random, in which case the conclusions drawn from the coherence and phase are not valid, since these are only defined for random processes. However, the large qualitative difference between the phase and coherence between the pairs N41 - N42 on the one hand and N43 - N44 on the other, supports the assumption that the CBM may be relatively strongly anisotropic.

Regarding the axial coherence and phase between detectors at the same radial position, Fig. 3.5, these are very similar to those of the previous three Stages, except for the behaviour of those for the pair N44U - N44L. There was a quite deep dip in the coherence and a deviation from zero phase at 6 Hz only for the detectors N44U - N44L. All other three radial pairs have high coherence and zero phase throughout this region. The dip for N44U - N44L is still there in the present Stage, but it has now two minima, i.e. it became a double dip. On the other hand, there was a "spike" in the phase of these detectors at around 7 Hz in the previous report, which is not present in the phase in the present Stage.

Similar deviations between one detector and the other three has also been observed in other measurements, both in R3 and R4. We do not have an explanation for this, but note that the detectors N44U and N44L differ from the others even in other respects in the latest four Stages, such as the smallness of the 8Hz peak in the APSDs. It is likely that these deviations from the other detectors have a common cause, but it is not possible to state whether it depends on the core-barrel vibrations, or on the N44 detectors themselves.

3.4 Analysis of the measurements made on 2022-03-30 (Measurement 2)

3.4.1 Individual spectra of all detectors

The APSDs of all eight individual detector signals are shown in Fig. 3.6. These look very similar to those in Measurement 1. Similarly to the previous Stages, a moderate increase of the amplitude of the 8Hz peak is seen. This is basically the expression of the known within-cycle term, which is manifested by the increase of the amplitude of the beam mode vibrations. The 8 Hz peak in the spectra of detectors N44U and N44L is still significantly smaller than that of the other spectra.
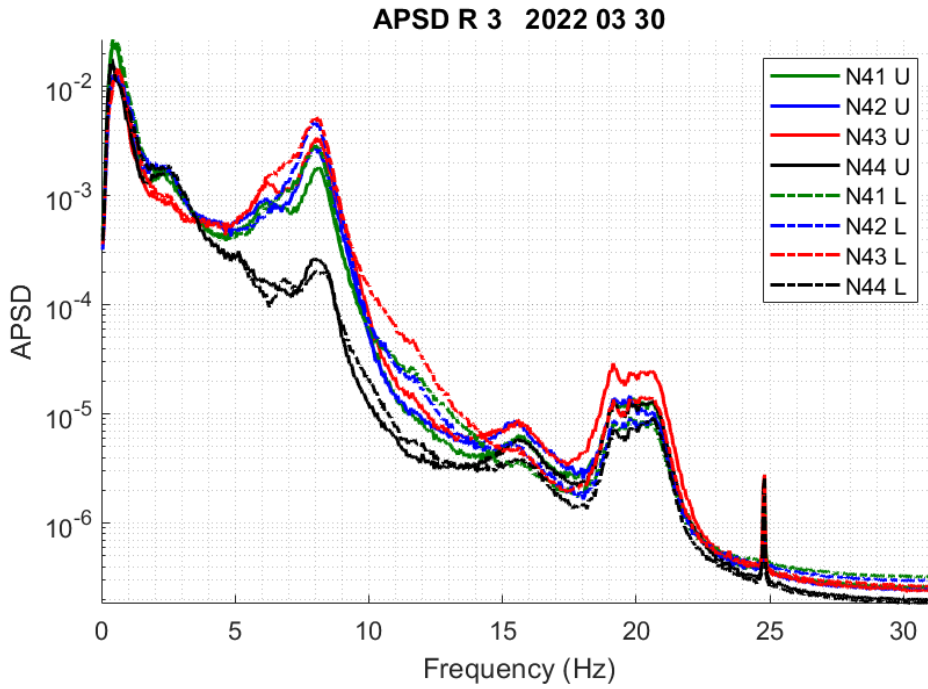

Figure 3.6: APSDs of all 8 ex-core detector signals from Measurement 2
.

3.4.2 Results of the mode separation

The results for the separation of the beam mode, shell mode, reactivity component and the tilting modes are shown for the upper and the lower detectors in Fig. 3.7. These results are also very similar to those of Measurement 1, which include the apparent deviations from Stages 2018 and 2019. One is the fact that the difference in the beam mode amplitude between the upper and the lower detectors has decreased significantly. As with Measurement 1, the most likely reason for this is the compensating effect of the upflow conversion.

The increase of the amplitude of the tilting mode as compared to the previous two Stages 2018 and 2019 is observed too. One difference to Measurement 1 is that the amplitude of the unexpected 8 Hz peak of the shell mode in the lower detectors has decreased, and became a double peak. Similarly to Measurement 1, and in contrast to Stage 2020, the 8 Hz peak is not the largest, and it became a double peak at 6 and 8 Hz, respectively. The much larger amplitude of the 20 Hz peak of
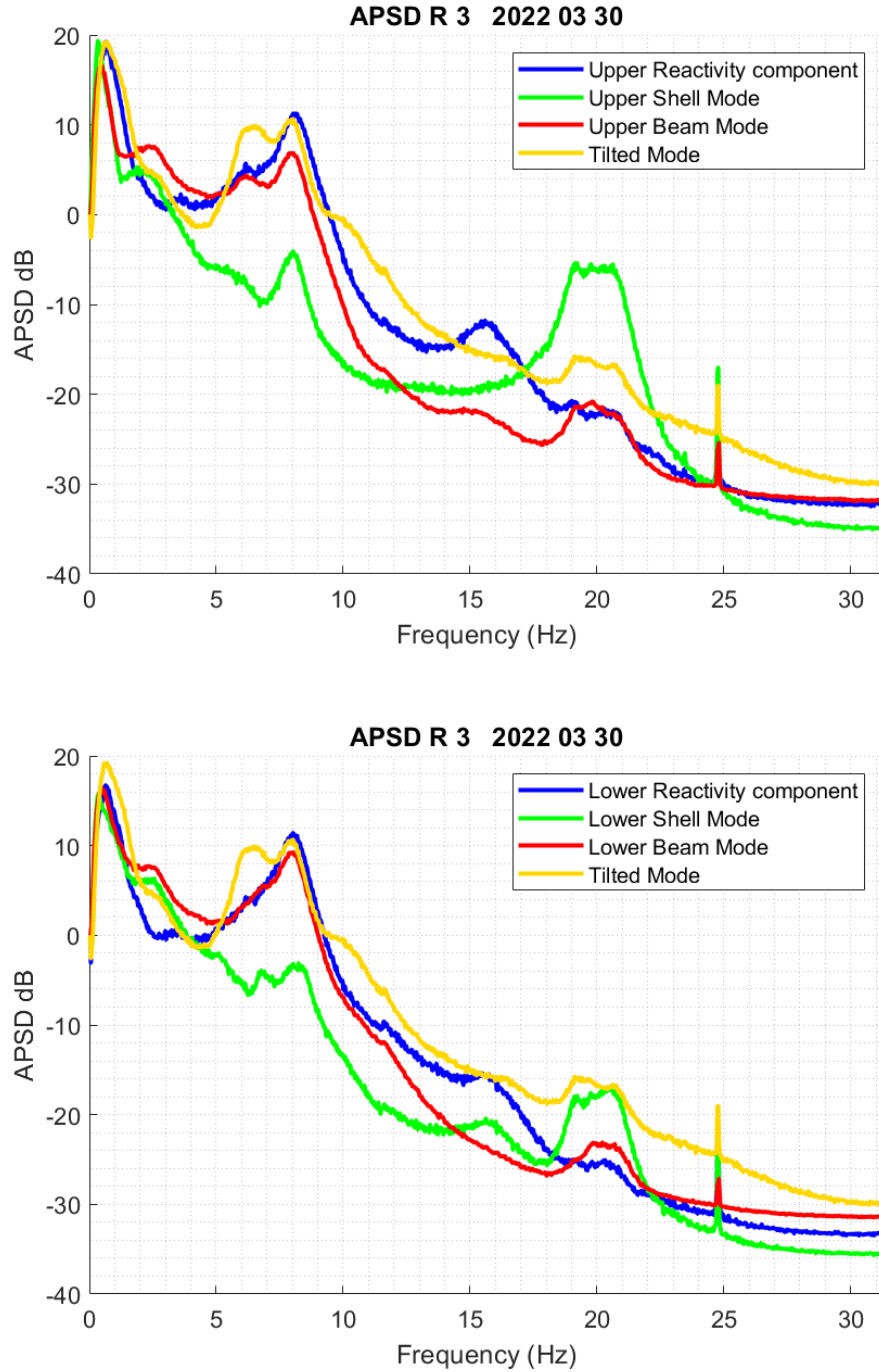
Figure 3.7: APSDs of the beam mode, shell mode, reactivity component and the tilting mode for the upper detectors (top figure) and the lower detectors (bottom figure), extracted from Measurement 2

the shell mode vibrations in the upper detectors than in the lower ones is the same as in Measurement 1 too. The possible reason of all these changes, i.e. the upflow conversion, has already been discussed in Measurement 1.

3.4.3 Phase and coherence relationships between the upper and lower detectors

The coherences and phases between the diagonally opposite detectors N41 and N42, for both the same and different axial levels, are shown in Fig. 3.8, and the same for detectors N43 and N44 in Fig. 3.9. The coherences and phases between the upper and lower detectors at the same radial positions, for all four detectors, are shown in Fig. 3.10.

Figure 3.8: The coherence and the phase of the CPSD calculated for the N41U-N42U, N41U-N42L, N41L-N42L and N42U-N41L detector pairs in Measurement 2.

These coherence and phase plots show mostly strong resemblance to those in Measurement 1. For the pairs N41 - N42 and N43 - N44, the coherences are very similar to Measurement 1. In the phase of the pair N34 - N44, the linear transition from 180° to -180°is now more pronounced than in Measurement 1. The structure of the double dip in the phase of the axial detector pair N44U - N44L, which behaves differently from the other three pairs, is somewhat different from that in Measurement 1; the dip is now deeper at 8 Hz, than at 6 Hz. Apart from these very minor differences, the rest of the results and their interpretations are the same as for Measurement 1.
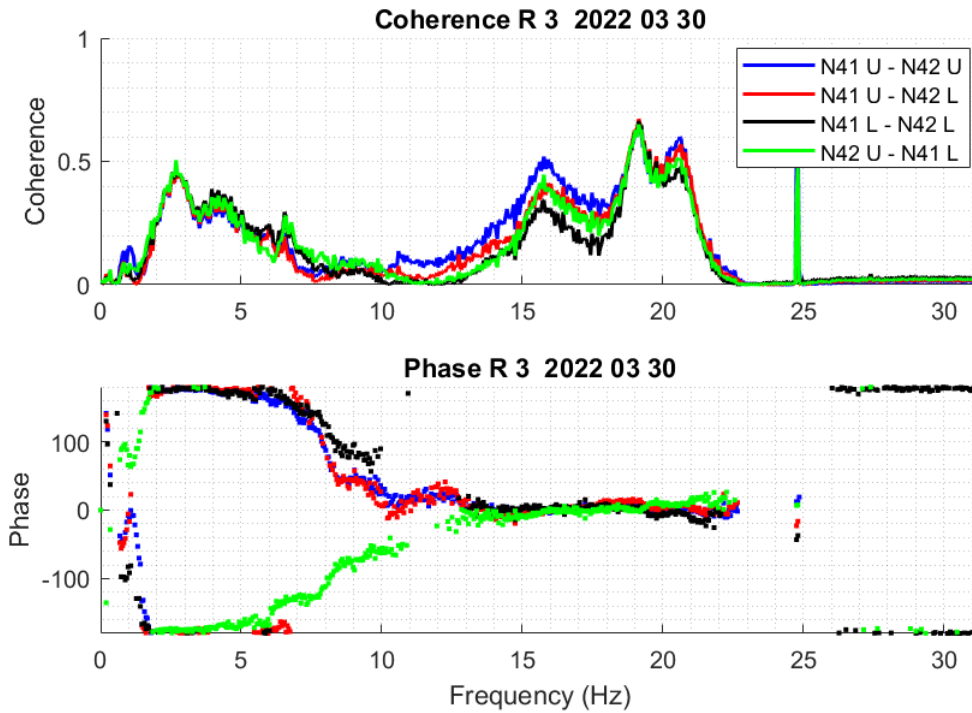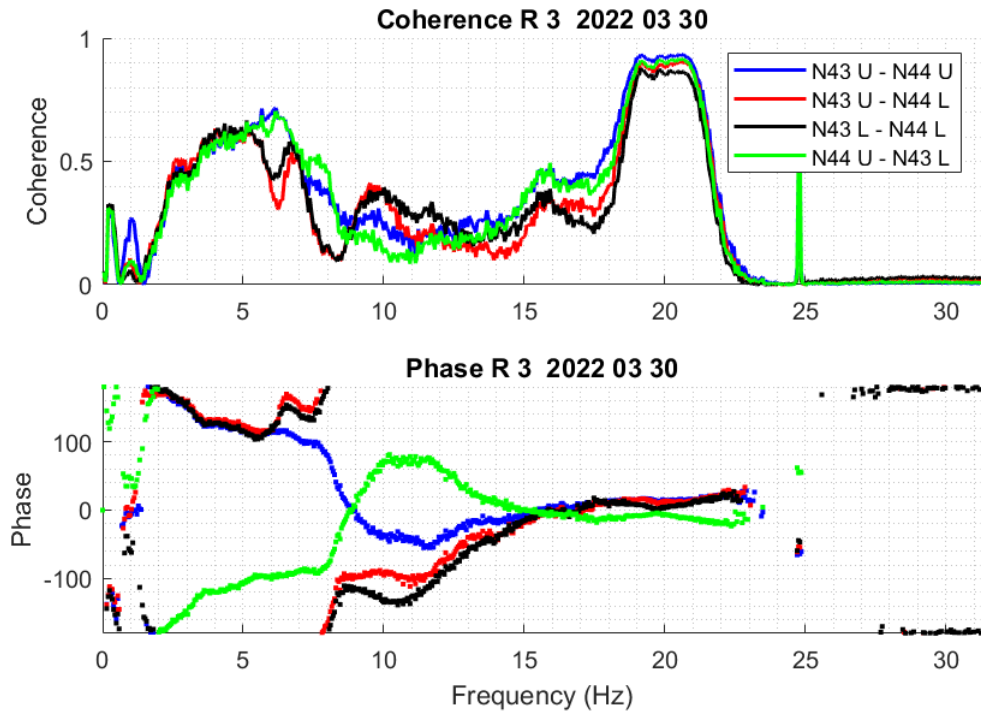
Figure 3.9: The coherence and the phase of the CPSD calculated for the N43U-N44U, N43U-N44L, N43L-N44L and N44U-N43L detector pairs in Measurement 2.
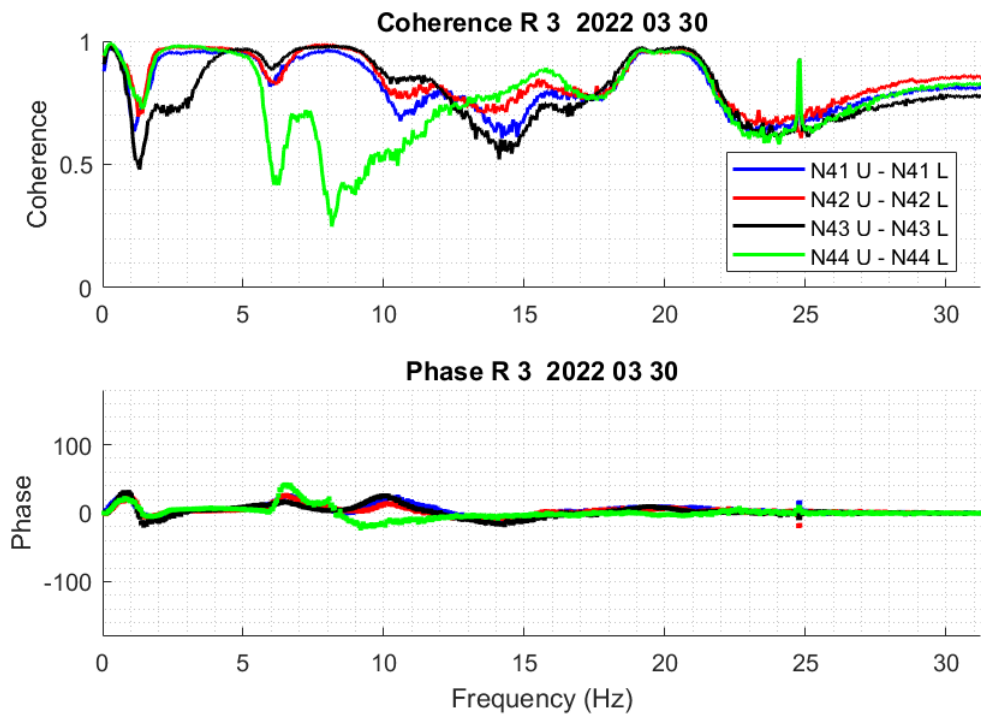

Figure 3.10: The coherence and the phase of the CPSD calculated for the N41U-N41L, N42U-N42L, N43U-N43L and N44U-N44L detector pairs in Measurement 2.

3.5 Analysis of the measurements made on 2022-05-12 (Measurement 3)

3.5.1 Individual spectra of all detectors

The APSDs of all eight individual detector signals are shown in Fig. 3.11. These look again similar to those in Measurements 1 and 2. The 8 Hz peak in the spectra of detectors N44U and N44L is still smaller than that of the other spectra.
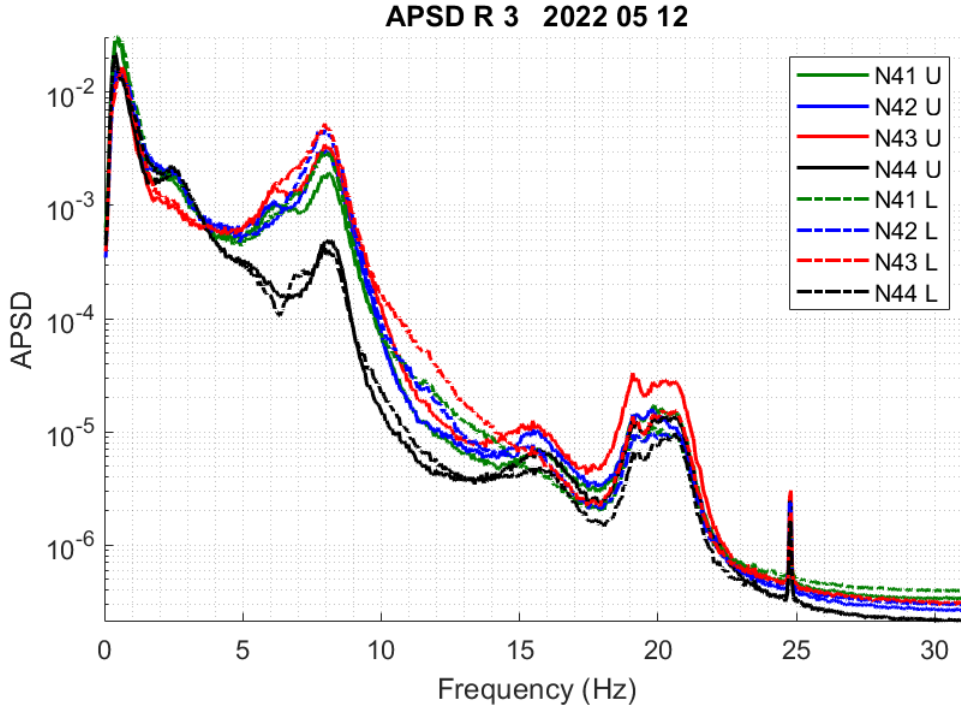
Figure 3.11: APSDs of all 8 ex-core detector signals from Measurement 3
.

3.5.2 Results of the mode separation

The results for the separation of the beam mode, shell mode, reactivity component and the tilting modes are shown for the upper and the lower detectors in 3.12. The (unexpected) peak in the shell mode at 8 Hz, which decreased from Measurement 1 to Measurement 2 in the lower detector signals, has again increased, and the double peak character has weakened. Since there were only two measurements in the previous Stage, no direct comparison of this result is possible with Stage 2020.

3.5.3 Phase and coherence relationships between the upper and lower detectors

The coherence and phase between the diagonally opposite detectors N41 and N42, for both the same and different axial levels, is shown in Fig. 3.13, and the same for detectors N43 and N44 in Fig. 3.14. The coherence and phase between the upper and lower detectors at the same radial position, for all four detectors, is shown in Fig. 3.15.

Again, apart from some minor differences, the structure of all these plots is
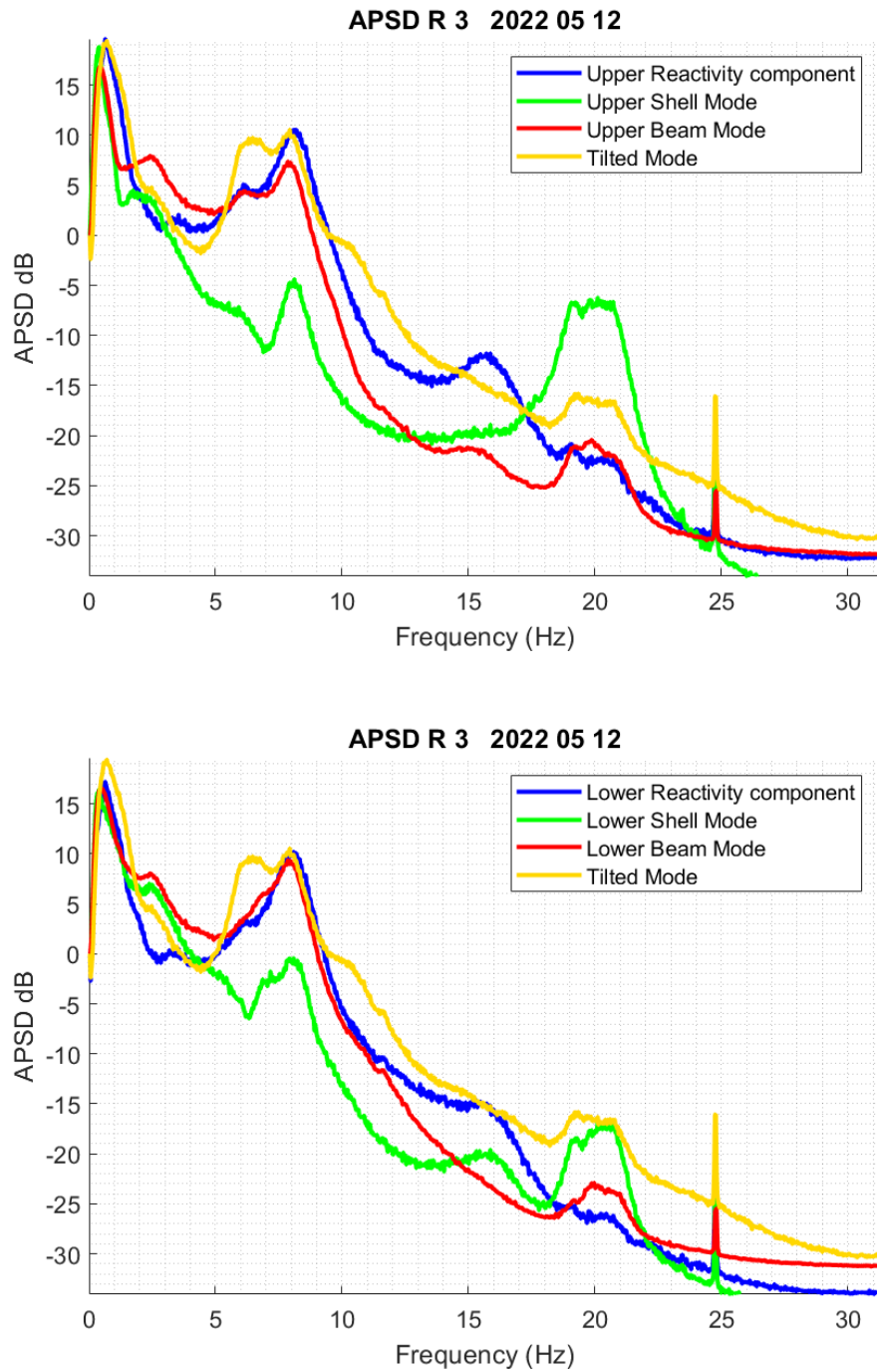
Figure 3.12: APSDs of the beam mode, shell mode, reactivity component and the tilting mode for the upper detectors (upper figure) and the lower detectors (lower figure), extracted from Measurement 3.

similar to the previous two measurements. The only minor deviation is that the double dip of the phase around 6 - 8 Hz between the detectors N44U - N44L has changed again. It became deeper at 6 Hz, whereas the dip at 8 Hz became somewhat shallower and its frequency increased to 9 Hz.
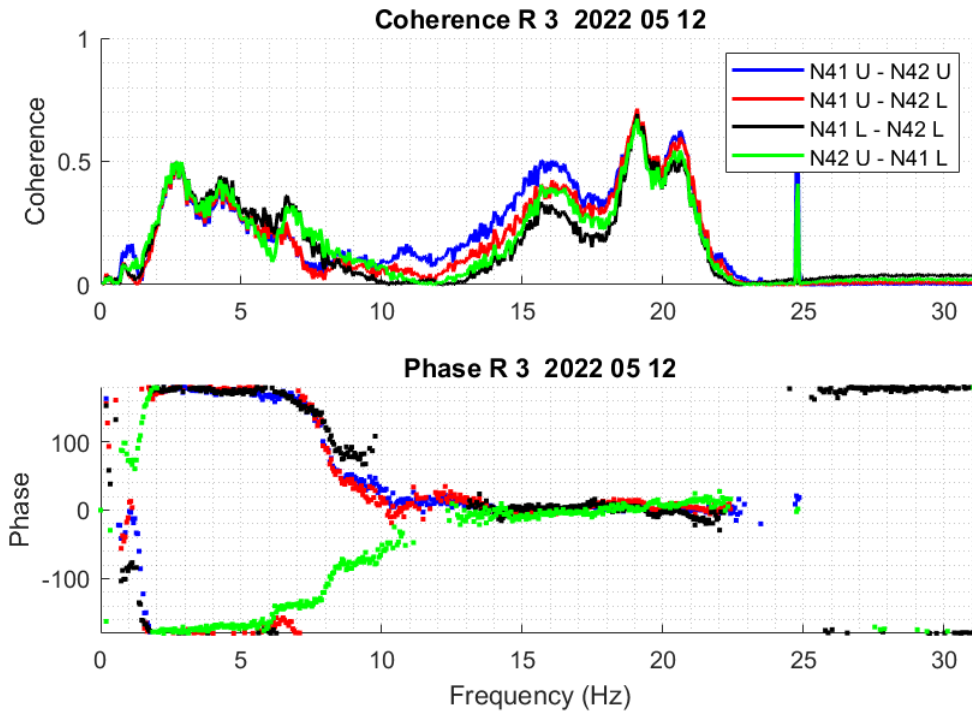
Figure 3.13: The coherence and the phase of the CPSD calculated for the N41U-N42U, N41U-N42L, N41L-N42L and N42U-N41L detector pairs in Measurement 3.
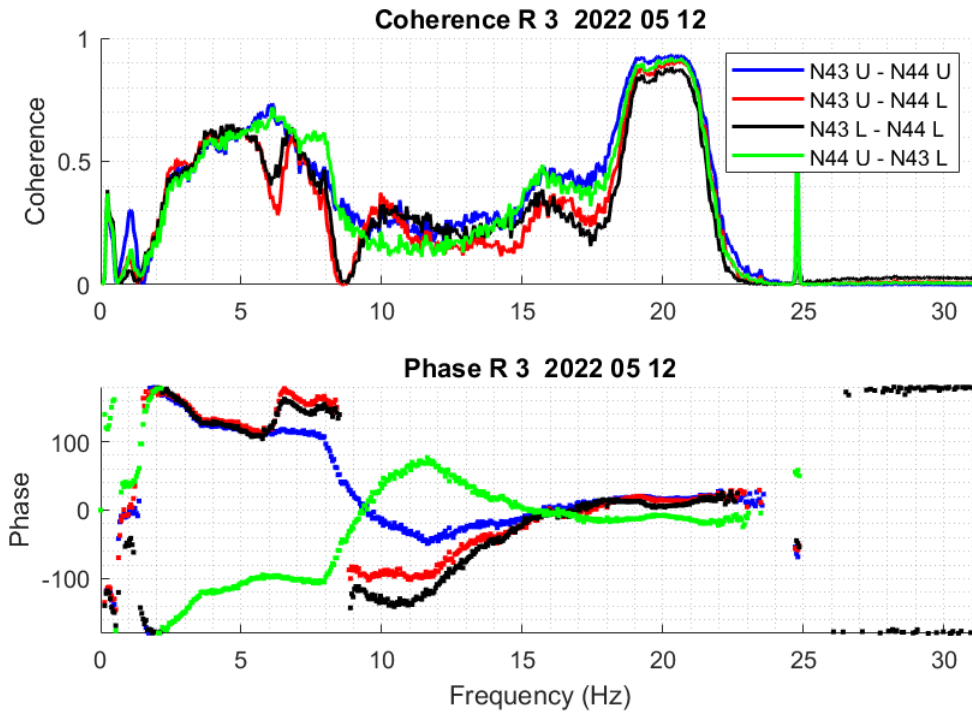
Figure 3.14: The coherence and the phase of the CPSD calculated for the N43U-N44U, N43U-N44L, N43L-N44L and N44U-N43L detector pairs in Measurement 3.
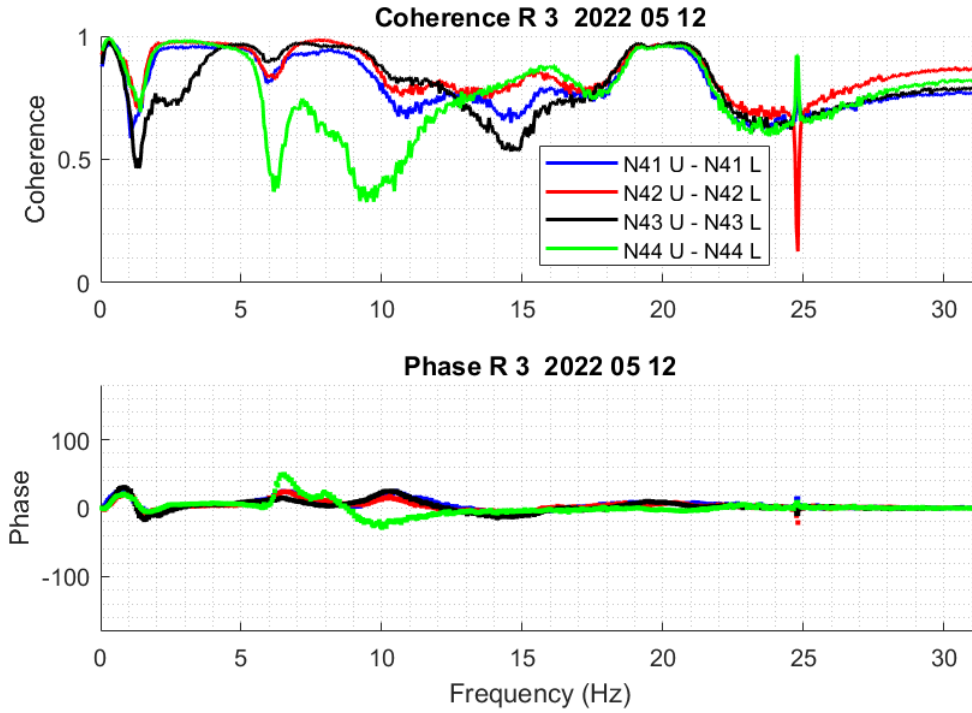
Figure 3.15:   The coherence and the phase of the CPSD calculated for the N41U-N41L, N42U-N42L, N43U-N43L and N44U-N44L detector pairs in Measurement 3.

3.6 Trend analysis within the cycle

The development within the cycle of the amplitudes of the beam and reactivity modes, also called Mode 1 and Mode 2, also called short term trend analysis, has been a matter of interest since quite some time back within the project. Optimally, this requires three measurements during the cycle. If only two measurements are available, as was the case in the previous Stage, the value of the short term trend analysis is limited.

As was noted in the previous reports, this analysis has been relatively difficult in the last measurements both in R3 and R4, due to the difficulties in separating two peaks very close to each other in frequency. Therefore some further refinement of the curve fitting and mode separation method was made by our collaborators at UPM when evaluating the measurements in Stage 2019, which was described in the last two Stages. This improved iteration process was used also in the analysis of the results this year.

The results of the curve fitting are illustrated in Fig. 3.16 for both the upper and the lower detectors from Measurements 2 and Measurement 3. These show a similarity to the results from the previous Stage, although there are some deviations both in the shape and the amplitude of the peaks. The main difference is that the peaks at 8 Hz became less pronounced and wider than in the previous Stage, both for the beam mode and the reactivity mode. Second, the increase of the amplitude of the reactivity mode (Mode 2) is significantly reduced as compared to that in the previous Stage. However, Measurements 1 and 2 in the previous Stage were made

at different times of the cycle than Measurements 2 and 3 in this Stage, so the comparison has a limited value.
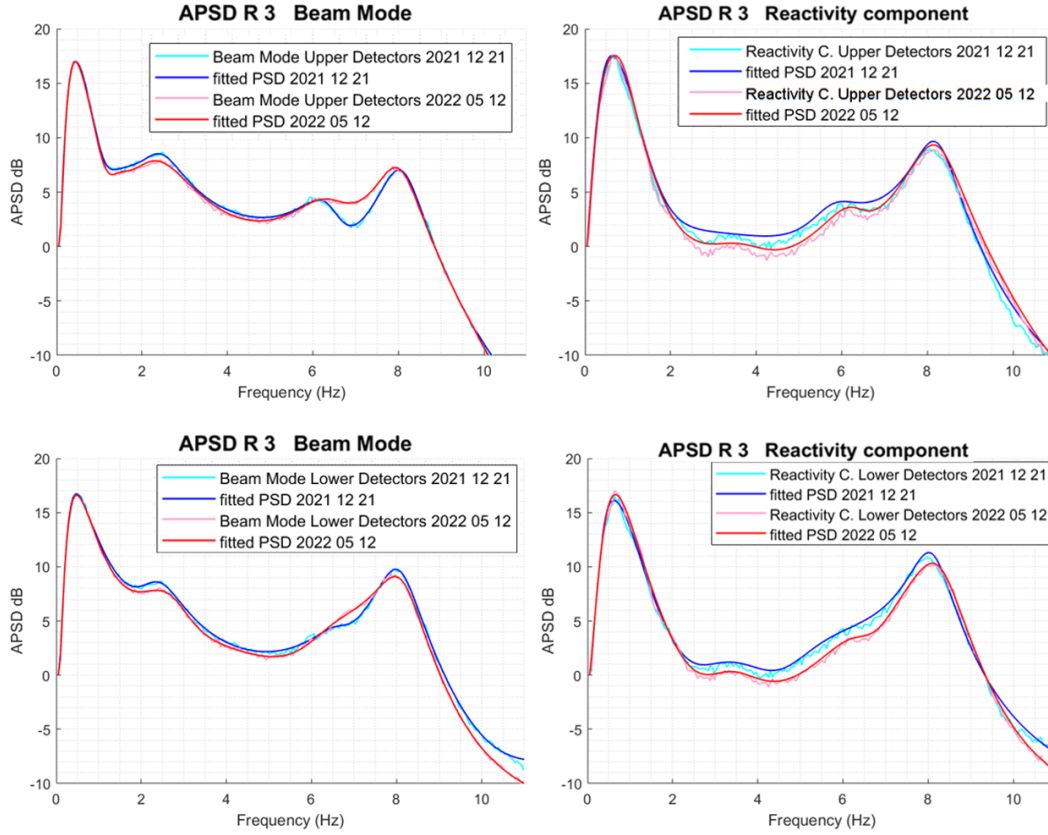
Figure 3.16:   Results of the curve fitting for Measurements 2 and 3 to the peak around 8 Hz for the beam mode (left side), and the reactivity component (right side), both for the upper detectors (upper figures) and the lower detectors (lower figures).

The results of the trend analysis for both Modes are shown in Fig. 3.17. One can note a similar increasing trend for both modes and both for the upper and the lower detectors, even if with slightly differing tendencies. This behaviour is similar to the previous Stages, but it also deviates from the previous measurements in R4, where only one of the modes (Mode 2) did increase during the cycle.

As also mentioned in the previous Stages, this contradicts our previous hypothesis on the character and expected behaviour for the two Modes, according to which Mode 1 (the beam mode) is practically constant during the cycle and only Mode two (individual fuel vibrations) increase in amplitude. It is worth noting that the appearance of this behaviour, which deviates from the previous hypothesis, coincides with the time when the formerly visible two peaks became indistinguishable. Even if with rather refined methods we achieved a separation of the two peaks, since we find a similar behaviour for both modes, one might consider to give up the mode separation process, and only treat one peak in the continuation. On the other hand, the amplitude of the two components is different, which may serve some information to the long-term trend analysis, as will be seen below.

Figure 3.17:   Trend analysis of the amplitude and frequency of the beam mode (Mode 1) and the reactivity component (Mode 2) at 8 Hz for the three measurements made during the cycle.

3.7 Long term trend analysis

The long term trend analysis concerns the development of the amplitudes of the beam and reactivity modes over a longer p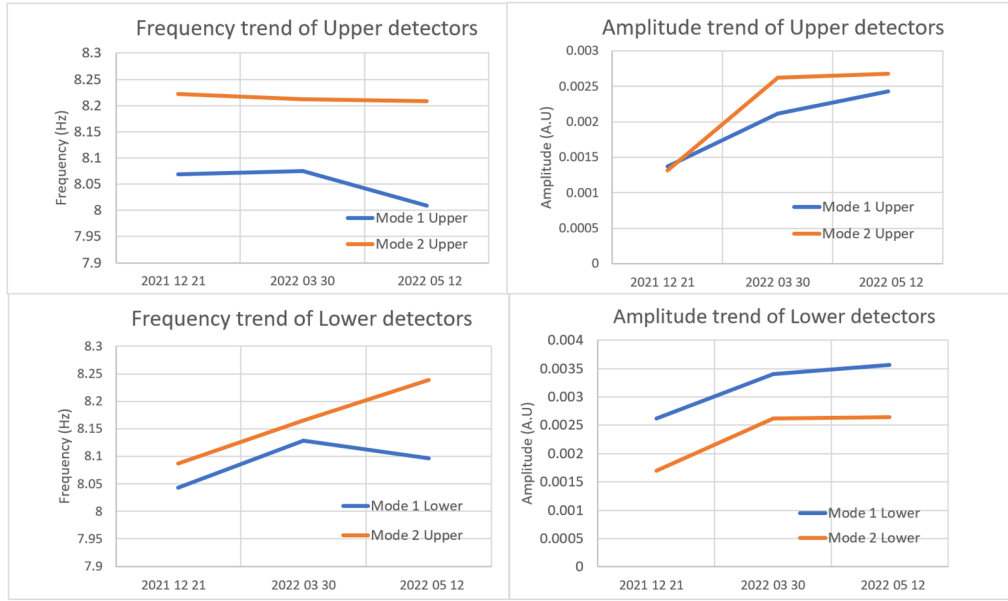eriod of time covering several cycles. The long term trend analysis can only be made to each unit separately, whereas usually measurements are made within one cycle only in one of the units. However, since cycle 35, the measurements were made in R3, hence with the results of the present Stage, a long term trend analysis can be made covering cycles 35 - 39. Actually, the measurements made in cycle 35 are not part of a Stage (there was a gap between Stage 2016 and 2018); they were only evaluated for the sake of the long term trend analysis. Only the two measurements made in spring 2018 were evaluated. Nevertheless, this means that with the data from the present Stage, a long-term trend analysis can be made covering the five cycles 35 - 39.

The results of the 5-year trend analysis for the beam mode are shown in Fig. 3.18. As was the case in the previous reports, the various measurements are referred to by year number, which is in all cases denotes the spring period of the corresponding cycle. Hence, the data from the present Stage 2021 are denoted by the year 2022, and the measurement made in December 2021 counts also to this year group. Even if this introduces some ambiguity, it was found to be more instructive to denote the labels on the x-axis this way. As was mentioned previously, only two measurements were mad in 2018 and 2021, respectively.

In the plot of the long term trend analysis, both the within-cycle trend, as well as the long term trend are visible. From 2018 until 2020 (Stage 2019), one could note a slow long-term increase of the amplitude of the beam mode. In particular the amplitude values for the lower detectors increased significantly between 2018 and 2020. It was surmised that this can be an indication of the fact that the play of the

Lower Radial Key has increased.
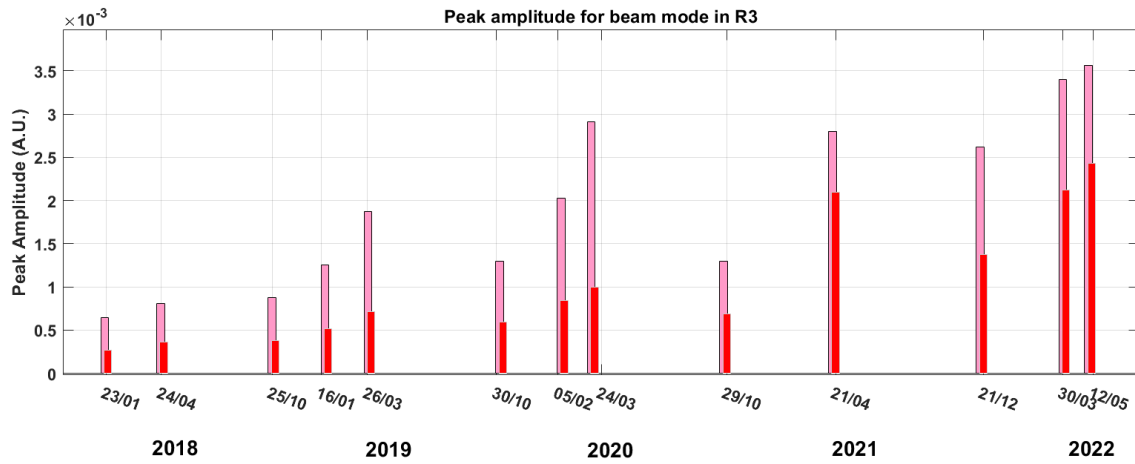
Figure 3.18: Five-year trend analysis of the amplitude of the beam mode (Mode 1). Red: upper detectors; pink: lower detectors.

In the previous cycle the trend was reversed, at least for the lower detectors. At the end of the cycle, the lower detectors showed a definitely lower value than in the preceding cycle, whereas the amplitude of the upper detectors are larger than at the end of the previous cycle. As it was already noticed in the preceding chapters, the difference between the upper and lower detectors has definitely decreased. Again, this change was very likely due to the upflow conversion.
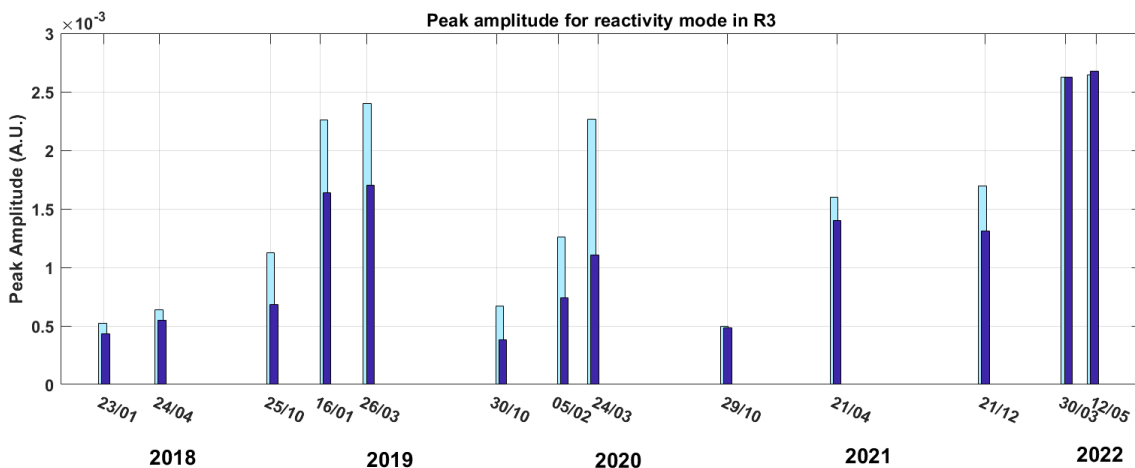
Figure 3.19: Five-year trend analysis of the amplitude of the reactivity mode (Mode 2). Dark blue: upper detectors; light blue: lower detectors.

In the present stage, one can again observe the increase of the amplitudes of the beam mode both in the upper and lower detectors. At the end of the cycle, the amplitudes are larger than not only those of the previous cycle, where the amplitudes were smaller than in the previous cycle, but even larger than the cycle preceding the

previous one. Hence, it appears that the beneficial effect of the upflow conversion is now superseded by the slow increase of the amplitude which was also observed during the period 2018 - 2020.

The same long term trend analysis for the reactivity mode, associated with the individual fuel assembly vibrations, is shown on Fig. 3.19. Here the behaviour was somewhat irregular in the preceding years. There was an increase between 2018 and 2019, whereas this increase was halted already in 2020, i.e. the year before the flow conversion. It was noted that since the reactivity mode is associated with the fuel vibration properties, which may change after each new core loading, a somewhat irregular trend is not completely unexpected. In 2021, after the flow conversion, the amplitudes got even lower, at least for the lower detectors. The character of the change is very similar to that of the beam mode, namely that the decrease concerns the lower detector signals (which give the higher amplitude), and that the difference between the upper and lower detectors has decreased.

In the present Stage (year 2022 in the plot) the amplitudes of both the upper and the lower detectors increased again, exceeding the highest amplitudes from the preceding years. One peculiarity is that in the last two measurements, the amplitudes from the upper and the lower detectors are the same, which has never been observed before. Even if the differences between the upper and lower detectors have decreased after the flow conversion, they have never been equal in amplitude.

3.8 Summary

On the whole, no significant changes in the APSDs, coherences and phases are noticed as compared to the previous Stages. What regards the long term trend analysis, the effect of the upflow conversion, noticed in the previous Stage, which led to a decrease of the difference between the upper and lower detectors in the beam mode, is still observable. On the other hand, the decrease of the amplitudes between Stage 2019 and 2020 seems to have been only temporary, as the amplitudes of both the beam and the reactivity mode increased, to the highest level since 2018 (cycle 35). The spectra and coherences of the detectors N43 and N44 differ in several ways from those of the other detectors, the reason of which is not clear.

4. PRELIMINARY EVALUATION OF THE FEASIBILITY OF A CONCEPTUAL DESIGN, THROUGH SIMULATIONS AND PILOT MEASUREMENTS, OF A FIBRE-BASED DETECTOR FOR THE MEASUREMENT OF THE GRADIENT OF THE NEUTRON FLUX

4.1 Introduction

In core physics and nuclear engineering in general, many applications are related to the task of locating the position of a neutron source, or some strong inhomogeneity (e.g. the the tip of a control rod), from the measurement of the neutron flux, or its fluctuation (the neutron noise) in the core. Based on the knowledge of the surrounding material and hence its effect on neutron transport and multiplication, the task can be achieved by an unfolding procedure, i.e. a kind of triangulation process [31, 32]. The unfolding relies on the fact that the neutron distribution on the neutron noise in the medium can be calculated for any arbitrary position of a hypothetical unknown inhomogeneity, neutron source or noise source, and one seeks the position of these which yields the minimum deviation between the measured and calculated values.

It was suggested earlier by us that in such inverse tasks of localisation, the efficiency and the accuracy of the localisation can be improved if, in addition to the usually measured scalar (angularly integrated) neutron flux, the neutron current vector or the gradient of the neutron flux, or the fluctuations of these, are measured [33]. Both the current and the gradient are vectors, hence they contain more (and independent) information compared to the scalar flux. The feasibility of using the flux gradient in both static and dynamic localisation problems in nuclear reactor cores (e.g., finding the position of a static neutron source, the tip of a partially inserted control rod, a vibrating fuel pin, or a vibrating control rod) was demonstrated via calculations [33, 34]. As it was emphasised in these publications, apart from the static flux gradient, even the fluctuations of the neutron current ("current noise"), or the fluctuations of the flux gradient ("gradient noise") can be used in reactor noise diagnostic problems, which lends significant advantages, especially when the number of accessible measuring positions is few.

It is worth noting already at this point that although, in general, the flux gradient is a 3-component vector in the 3-D space of the core, in most cases the axial coordinate is not of interest, and it is sufficient to use the two horizontal components of the gradient vector. This is because, except the case of determining the axial position of a control rod tip [35], the task is to find the position of a perturbation in the horizontal plane of the reactor: a vibrating control rod or fuel pin, a local thermal hydraulic instability etc. Hence throughout in this work, as well as in all previous pilot measurements, only the aspects of the measurement and use of the two components of the gradient in a horizontal plane are investigated.

What regards experimental verification, so far only the measurement of the static gradient, and in one case that of the partial current, was investigated in pilot mea-

surements. The possibility of locating the position of a neutron source in a water tank from the measurement of the scalar flux and its gradient in one single point was demonstrated experimentally, with the unfolding procedure being supported by Monte Carlo simulations [36]. Another work demonstrated experimentally the possibility of using a single detector (whose half circumference was covered by cadmium) to measure the scalar flux and an approximation of the partial currents, and to identify the position of a neutron source in a water tank from such measured quantities [37, 38].

The measurement of the flux gradient or the neutron current was made possible by the use of very thin detectors (about 1 mm), developed in Japan [39, 40], which allows to obtain the scalar neutron flux with a high spatial resolution. In these detectors a small volume of a mixture of neutron converter and scintillation material is mounted on the tip of a light guiding fiber. In our earlier pilot measurements, only one single fiber was used for the measurement of the flux gradient. The gradient was determined by placing the same detector sequentially in several positions around the circumference of a small circle, and estimating the line integral from the measurements around the circle.

Such an experiment is suitable for a proof-of-concept, but the method is not useful in practical situations. For a fast and reliable measurement of the flux gradient, a dedicated detector can be constructed with several small neutron sensitive volumes grouped together, so that the scalar flux is taken in several nearby positions concurrently. The need for such a detector arose recently in connection with a collaboration, in form of a PhD project between Chalmers and the Belgian Nuclear Research Centre SCK CEN [41]. The goal of the project is to detect and identify, with the help of neutron measurements inside a fuel assembly, whether one or more fuel pins have been removed and replaced by dummy rods, and if so, in which positions. Again, this is clearly a 2-D problem, since removal of only a part of a pin is unrealistic. This diversion scenario is known in the safeguards community as detection of partial defects in a fuel assembly [42, 43]. The idea is to perform measurements of the scalar flux and its 2-D gradient concurrently in several radial positions within a fuel assembly (in the detector guide tubes), and comparing the measured flux shape and the spatial dependence of the gradient with those calculated from the declared data of the (intact) fuel assembly to discover the absence of fuel pins and to identify their position.

Although this is a problem of nuclear safeguards, the detector concept aimed to be developed in the project itself is not specific to this particular application. Rather, it is generic in the sense that it aims to develop a gradient detector which is suitable for in-core measurements, i.e. inside a PWR fuel assembly. Such a gradient detector would be suitable for measuring the static flux gradient, as well as the gradient noise, which can be used to enhance the existing in-core noise diagnostic methods. Actually, the existence of such a detector is a prerequisite to perform localisation of a vibrating fuel pin from the neutron noise and the gradient noise, as elaborated in Ref. [34].

Since the gradient detector will consist of a cluster of four thin scintillators for the two vector components, it will have larger radial dimensions than the individual

fibres. Hence, it can only be inserted into a few special positions within an assembly, such as the detector guide tubes, or possibly some empty control rod channels. This limits the diameter of such a gradient detector to about 1 cm, and this limitation is kept in mind in the design and in the conceptual study below.

The present work concerns only the investigation of the conceptual design of such a flux gradient detector, suitable for measurements within a PWR fuel assembly, and investigate its performance in the static case. The development of the detector itself will go in several steps. First, a detector design is proposed, consisting of four fibre-mounted scintillation detectors arranged in a rectangular pattern within a cylindrical holder, and its performance is investigated via numerical simulations. This is the subject of the present Stage. The next step will be the construction of the detector. Experience with using single fibers for flux measurements is available from previous experimental work, hence the necessary technology for constructing the proposed detector is available and accessible. Finally, the performance of the detector will be investigated in pilot measurements, and possibly in in-core measurements e.g. in a research reactor.

In the subsequent Sections, first the design of the detector will be described. Then a Monte Carlo model of the detector and a test case is introduced in order to assess the performance of the detector. Finally, the results of the numerical investigation of the performance of the detector are discussed.

4.2 The detector design

Although the diameter of the fiber detectors can be as small as about one mm, the diameter of the gradient detector, allowing the measurement of the flux in different positions from which a reliable estimation of the gradient can be obtained, will be inevitably larger. By aiming at performing measurements within a nuclear fuel assembly, one can use the instrumentation guide tubes of the assembly, which are about 1 cm in diameter.

A gradient detector, capable of measuring the x and y components of the flux gradient (which, in a 2-D cylindrical geometry can also be referred to as the r and φ components), with the mentioned size limitation, is proposed as follows. Four axial holes in an aluminum cylinder of a diameter of 1 cm serve as holders of four fiber-mounted scintillation detectors, arranged in a rectangular pattern, as shown in Figure 4.1. The fibers are inserted into the guide tubes from above, and their tip is covered in the neutron sensitive converter and scintillation material, as shown in Figure 4.2. The detector, together with the fibers, is inserted into the instrumentation guide tube and moved to a suitable position sufficiently below the top of the assembly such that the axial flux gradient can be negligible. The two detector pairs at diagonally opposite positions, perpendicular to each other, can be used to measure the two horizontal components of the flux gradient. Aluminum is chosen as the matrix, holding the detectors, due to its easy manufacturing properties, and low neutron absorption cross section.

One remark on the terminology is in order here. The collection of the four fiber-mounted scintillation detectors together constitutes the "gradient detector". In
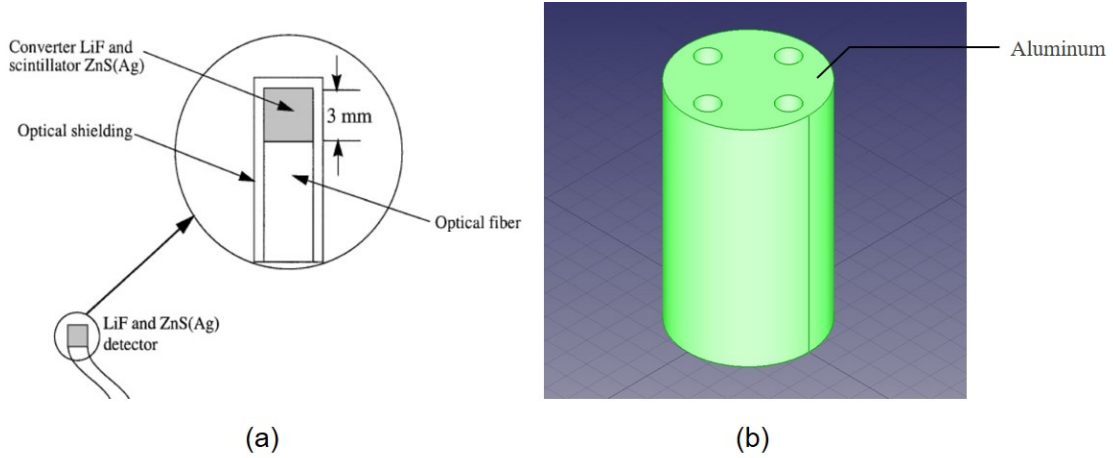
Figure 4.1: A scheme of the planned gradient detector (a) The optical fibers with the scintillation material at their tips (b) Aluminum cylinder that acts as a holder for the detectors.
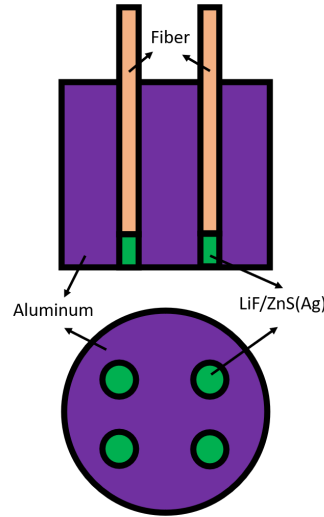
Figure 4.2: A vertical and horizontal cross section view of the detector concept.

order to avoid confusion to call both the collection of the four scintillators, as well as the individual scintillators a "detector", we will follow the terminology that the four scintillators together, i.e. the gradient detector, will be called the "detector". Whenever we want to refer to a single fiber-mounted scintillator, it will be simply referred to as a "scintillator".

4.3 Monte Carlo model of the detector and of a test case

Whereas it is intuitively clear that, in principle, such a detector is suitable to determine the flux gradient, it is useful to assess its performance by detailed simulations. The motivations for this are twofold. First, similarly to the case of the ordinary neutron detectors, the presence of the detector, and in particular the four neutron absorbing scintillators, will affect the neutron flux distribution. The consequences of such a flux distortion are usually not significant when measuring the

scalar flux. However, the gradient is estimated from the difference of two values of the neutron flux, measured relatively close to each other, and hence it is obtained as the small difference of two values close to each other. If the distorting effect of the four scintillators is not uniform, then the presence of the detector may have a much more substantial effect on the accuracy of the determination of the flux gradient than for the scalar flux. Second, systematic distortions might arise from a self-shielding effect, i.e., the scintillators at the higher flux position might shield against the neutron current pointing to the scintillators at the lower flux position. If the effect is relevant, then the detector will systematically underestimate the gradient. Such a possible consequence needs to be investigated quantitatively.

The simulations performed in this work are restricted to the neutronic aspects of the measurement, i.e. calculating the reaction rates in the detector. That is, the generation and transport of the scintillation light is not taken into consideration. The reason for this is that the effects to be studied, such as the influence of the presence of the detector on the estimation of the gradient, is a pure neutronic problem. Although the conversion of the neutron reactions inside the detector into scintillation light, photon transfer to and transport in the fiber, etc. are an important part of the physics of the measurement, which influence the efficiency of the detector, these processes are not relevant from the point of view of the objectives of the present study. Including the light generation and transport into the simulations would require a substantially larger effort, with minimal extra information.

The quantitative work for the assessment of the performance of the detector was made using the open-source code Serpent [44]. Serpent is a multi-purpose three-dimensional continuous-energy Monte Carlo particle transport code developed at VTT, the Technical Research Centre of Finland. The code is designed for traditional reactor physics applications, for multi-physics reactor calculations, and for neutron and photon transport calculations in radiation, fusion and medical physics problems. Serpent also includes numerical capabilities that allow parallel computing on clusters and multi-core workstations.

The strategy to quantify the perturbative effect of the presence of the detector on the accuracy of the determination of the flux gradient goes as follows. Given a system of interest, two sets of simulations are performed. The first simulation does not include the detector and the "unperturbed" thermal neutron flux is calculated in some hypothetical measurement positions where the gradient detector can be inserted. In the second step, simulations are made for the case that the detector is occupying the positions previously selected, one at a time, and the reaction rates in the scintillators are calculated. The gradient obtained from the difference of the reaction rates of the diagonally opposite scintillator pairs is then compared with the gradient of the neutron flux obtained without the detector.

The comparison of the gradient from the unperturbed flux with the gradient from the reaction rates is, however, not completely trivial. It is obvious from simple physical considerations that at any single measurement point, the magnitude of the gradient will be quantitatively different for the flux and the reaction rate, since they correspond to physically different quantities. Nevertheless, the two are proportional to a scaling factor which can be considered as a constant when the energy

distribution of the flux in the system is also constant (this is indicated in Fig. 4.5, showing that the thermal spectrum even inside the source itself is very similar to that in water). The scaling factor does not depend on the actual value of the gradient, and hence on the measurement position. Then the proof of the equivalence is based on the equivalence of the space dependence of the two gradients. If the space dependence of the two gradients is proportional to a constant scaling factor, then it is a demonstration of the negligible effect of the presence of the detector on the measurement of the flux gradient.

The existence of a proportionality factor between the flux gradient and the gradient of the detector response is by no means a problem for the task of localising an unknown perturbation, or an unknown source. Such a task is always based on relative values (ratios of the flux, the neutron noise, or their gradients, as measured in different space points) because in a practical case the strength of the source is not known. Therefore the absolute values of the flux or the gradient are not of interest anyway. The diagnostic information lies in the space dependence of the gradient, and it is this latter which should be reconstructed correctly.

As mentioned above, the first step with Serpent was to calculate the spatial distribution of the neutron flux in a hypothetical arrangement without the presence of the detector, in which thereafter measurements with the proposed detector would be simulated. The arrangement was chosen to be similar to those used in earlier works, namely the case of a neutron source in a water tank [36, 37]. The reason is partly that it is a simple setup, with an azimuthally symmetric flux distribution in the horizontal plane, in which the results can be easily interpreted intuitively. And partly, because such an experiment will be possible to carry out at a later stage of the project, when the detector will actually be fabricated. The general layout is shown in Figure 4.3. It consists of a cylindrical Aluminum tank 1m in height and 1m in diameter filled with water, with a ^{252}Cf source, 2cm in diameter, in the middle.
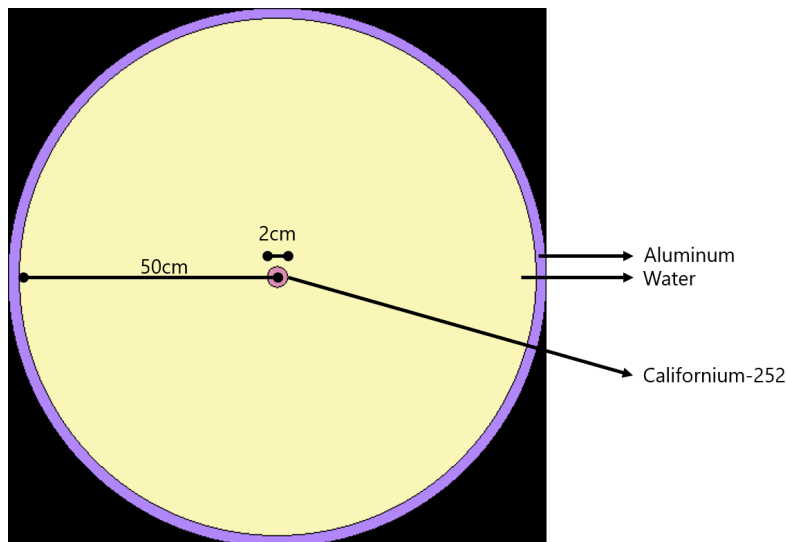

Figure 4.3: Setup used for the evaluation of the detector, as modelled in Serpent.

The next step was the modelling of the part of the gradient detector which are called "scintillators" in this paper. There exist several different options for small

size neutron detectors in terms of neutron converter and scintillation material (Li-CaF, boron loaded plastic scintillator, etc.). We restrict the present study to the type of detectors which we have at hands and which were also used in previous works, namely LiF as neutron converter and ZnS(Ag) as the scintillation material. Two such detectors are available by courtesy of Kyoto University Institute for Integrated Radiation and Nuclear Science (KURNS). The detailed Serpent model of the detector is shown in Figure 4.4.
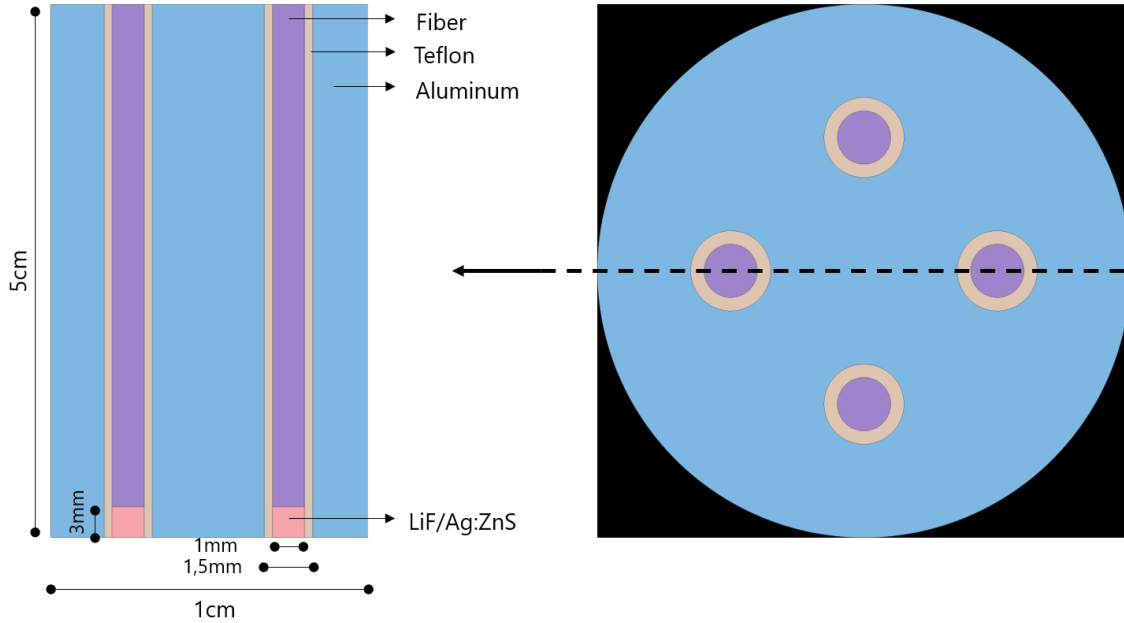
Figure 4.4: The LiF-based gradient detector as modelled in Serpent.

4.4 Quantitative analysis

The Serpent model of the test case is used to analyze the energy and space dependence of neutron flux due to the californium-252 source in the water tank. Then simulations were performed to study the performance of the proposed detector to estimate the neutron flux gradient in such a test case.

4.4.1 Estimation of the neutron flux in the test case

Sample results of the energy and space dependence of the neutron flux estimated for the source in the water tank are shown in Figures 4.5 and 4.6, respectively. Far away from the source (indicated as "Water" in the figure), a thermalised spectrum is seen. Inside the sample (^{252}Cf in the figure legend), in the thermal region the spectrum is very similar to that in the water, in the epithermal region one can see the fission resonances inside the sample, and the fast spectrum is determined by the spectrum of the spontaneous fission of the ^{252}Cf source.

Regarding the space dependence, the thermal flux is of primary interest, since the detector is assumed to be sensitive to thermal neutrons. The space dependence of the thermal flux shown in Figure 4.6 is similar to the one found in the previous experiments, although a different type of source was used. The thermal flux decays

with increasing distance from the source, but this decrease is not monotonic. There is a dip in the vicinity of the source, which is due to the absorption of the thermal neutrons in the source itself. This space dependence is suitable for the investigation of the performance of the detector, because there are positions with both small and high flux gradients, the radial component changing from positive to negative with increasing distance from the centre. In order to verify the Serpent model, the calculations were also performed with the Monte Carlo code MCNP [45]. Figure 4.6 shows that the results from the two codes are in good agreement.
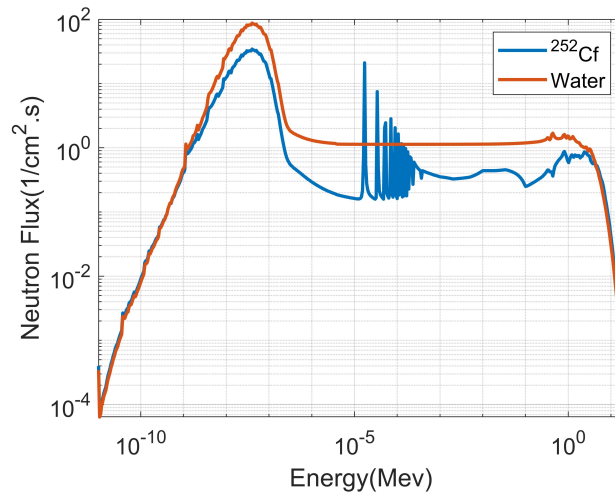

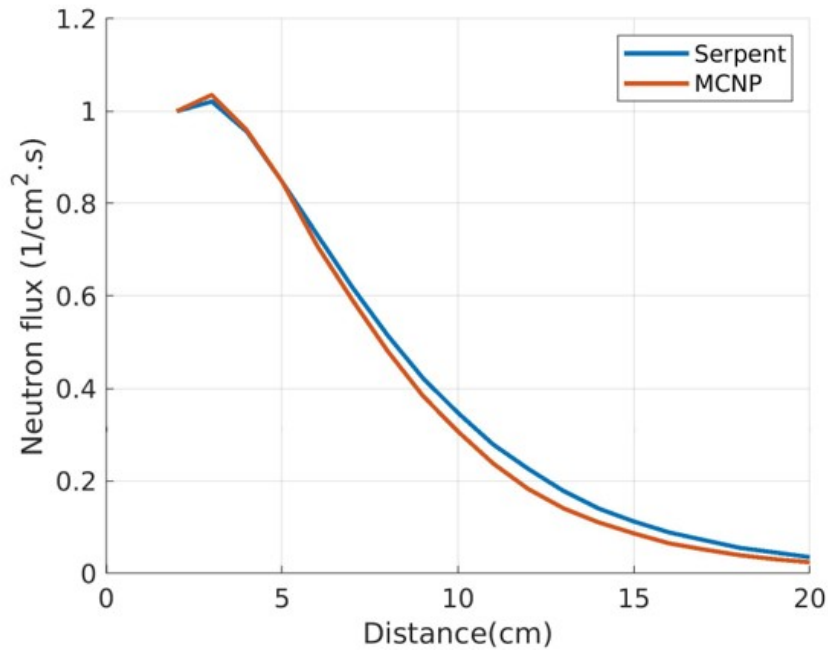Figure 4.5: The energy spectrum of the neutrons in the ^{252}Cf source and in the surrounding water.

Figure 4.6: The radial dependence of thermal neutrons in the measurement setup.

4.4.2 Investigation of the performance of the detector

The performance of the detector to determine the magnitude and the direction of the neutron flux gradient was investigated via Monte Carlo calculations in the case of the setup defined in section 3. Different positions and orientations of the detector in the water tank, and the effect of scintillators with non-ideal ^{6}Li content were considered.

Estimation of the magnitude of the gradient

As mentioned in Section 4.3, one goal is to investigate how the presence of the detector affects the accuracy of the estimation of the gradient. In this step, we chose a detector orientation such that two scintillators were lined up on the x-axis, i.e. the line connecting two of the scintillators was pointing to the source (towards the centre of the water tank). Because of the azimuthal symmetry of the setup, these two scintillators measure the radial gradient (i.e. its x-component), and the azimuthal component of the flux gradient is zero. Hence, the radial component is equal to the absolute value (magnitude) of the gradient. The Serpent model of this arrangement is shown in Figure 4.7.

(Cross-sectional view)   (Top view)
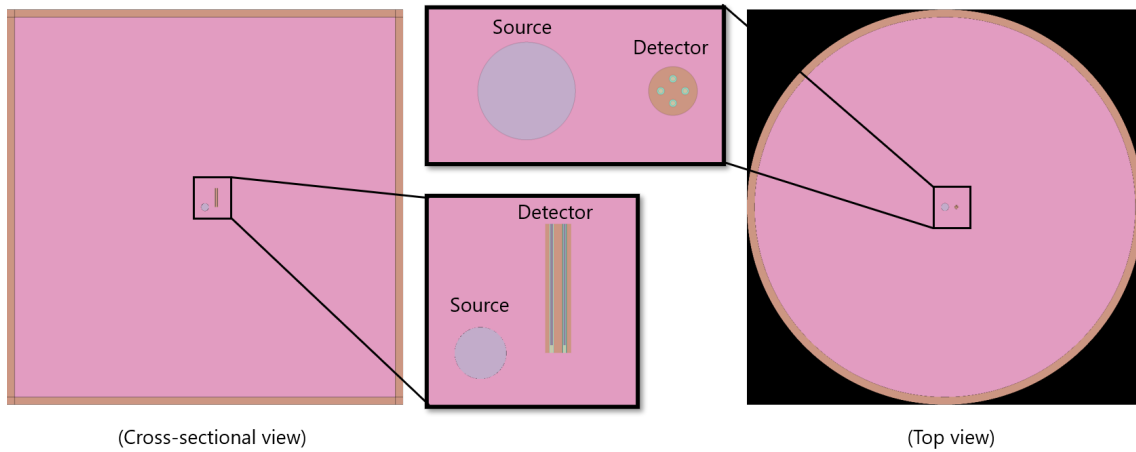
Figure 4.7: The Serpent model for the simulation of the measurement of the radial component of the gradient.

Calculations were made by including the detector in the setup. The reaction rates in the four scintillators of the detector were calculated. To assess the possible distorting effect of the detector, as described in Section 4.3, the gradient was calculated both from the neutron flux which prevails in the system without the detector, as well as from the reaction rate in the scintillators, with the whole detector being included into the simulations.

The comparison of the space dependence of the flux gradient and the gradient based on the reaction rate is shown in Figure 4.8. The space dependence of the gradient, determined from the reaction rates in the detector, follows very closely the space dependence of the gradient of the unperturbed flux over the whole spatial measurement range, indicating that the distortion effect of the proposed detector

design is negligible.
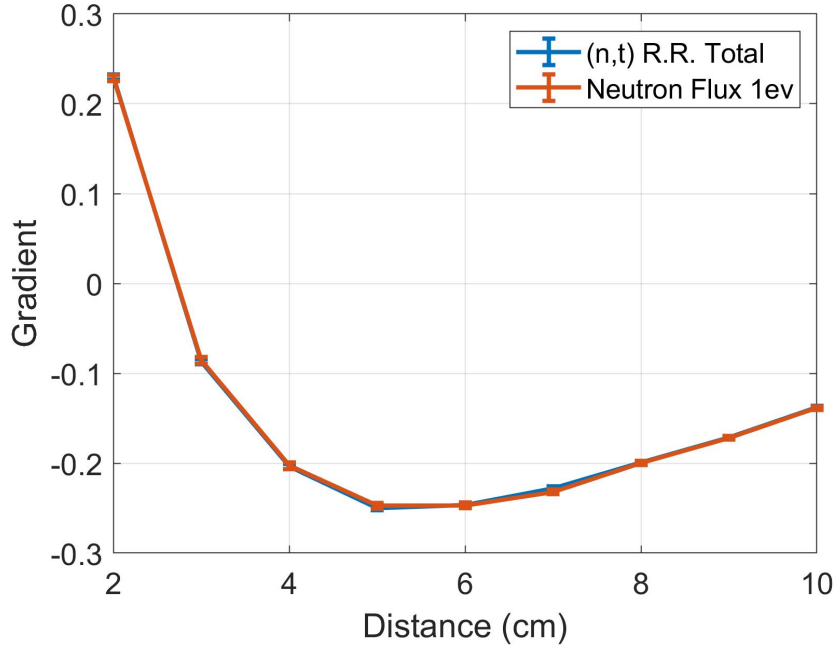
Figure 4.8: The spatial dependence of the radial component of the gradient with and without the presence of the detector.

Estimation of the direction of the gradient vector

The two-dimensional flux gradient has two Cartesian components which carry independent information. For practical purposes, instead of using these two components, the space dependence of the magnitude (absolute value) of the gradient and its direction are used in unfolding problems. This is because the absolute value and the direction are physical concepts with a physical content that is easier to interpret intuitively. One can see an analogy with the case of complex valued physical quantities, such as Fourier transforms of time dependent signals in the frequency domain, where the amplitude and phase have clear physical meaning, as opposed to that of the real and imaginary parts individually. From the point of the planned application, the magnitude and direction are more effective feature parameters in a pattern recognition or any other identification/unfolding task than the vector Cartesian components.

Therefore, it is useful to investigate the suitability of the detector to estimate the direction of the gradient vector. The best way of doing this is when both components of the gradient are different from zero. In the present setup, this means that the detector needs to be positioned such that none of the two scintillator pairs lie on a radial line (i.e. along the x axis in a Cartesian system). Other special orientations are also avoided, e.g., when the angle between the two scintillator lines and the x axis is $\pm 45°$. Then, we chose a setup where the detector was rotated 30° counterclockwise as compared to the calculations in the previous Subsection. An illustration of this case is shown in Figure 4.9.
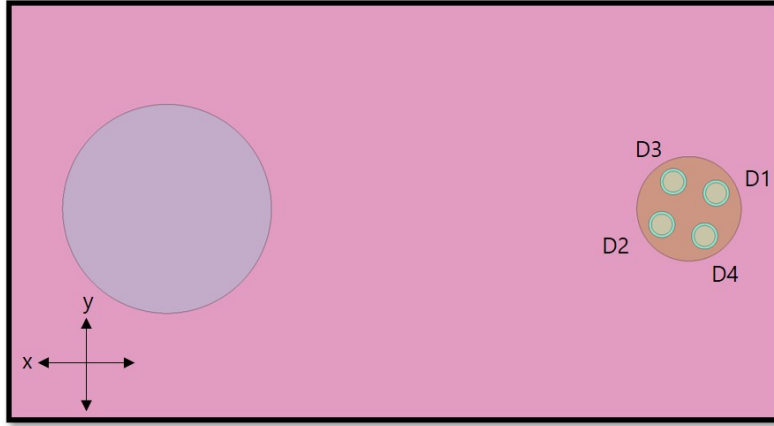
Figure 4.9: The Serpent model of the measurement of the direction of the gradient showing the detector shifted in a 30° angle counterclockwise.

The detector measures the two components of the gradient in the coordinate system determined by its own orientation, but the orientation of the measured gradient vector is naturally independent from the orientation of the detector as shown in Figure 4.10. We performed several simulations with assuming the detector at different positions along the x axis, and the results of the direction of the gradient vector from the calculated reaction rates are shown in Figure 4.11. The Figure shows that the direction angle of the gradient is estimated correctly.
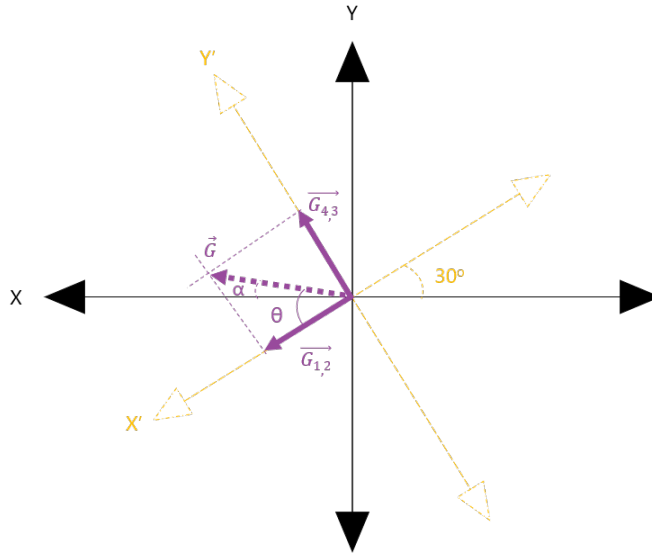
Figure 4.10: The detector coordinate system based on its orientation (yellow) the original coordinate system of the measurement setup (black) and the two components of the gradient vector (purple).

To prove the consistency of the performance of the detector, the magnitude (as an absolute value) of the gradient vector measured by the detector was compared between the case where the gradient was calculated from only the horizontal component as in section 4.4.2 (normal case) and the case where the gradient was calculated from the two components after it was shifted by a 30° angle. The values of the mag-
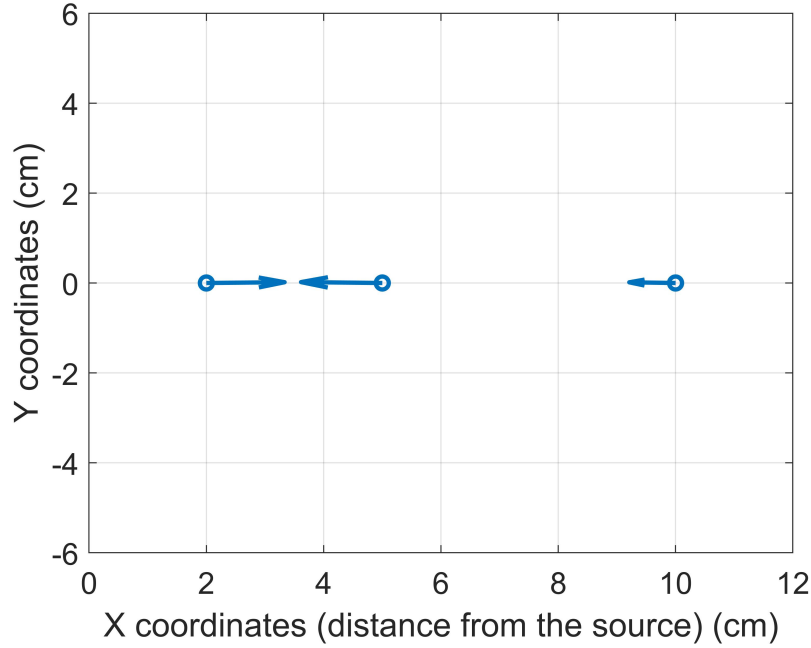
Figure 4.11: The direction of the gradient vector at different placements of the detector along the x-axis.

nitude of the gradient in the two cases, at different positions along the x-axis, are listed in Table 4.1. It can be seen that the detector is capable of giving similar values of the magnitude of the gradient regardless of its orientation.

Table 4.1: A comparison of the magnitude of the gradient vector.

Distance (cm)	Magnitude of the gradient			
	Normal case		30° angle shift	
	Value ($\times 10^{-3}$)	Uncertainty (%)	Value ($\times 10^{-3}$)	Uncertainty (%)
2	3.77	1.22	3.86	2.04
5	-4.10	1.05	-4.01	1.61
10	-2.26	1.07	-2.28	1.58

Effect of the differences in the scintillators of the detector

In the simulations so far, it was assumed that all four scintillators are equal and thus have the same efficiency. In a real detector, the four scintillators may slightly differ from each other, especially in view of their manual manufacturing procedure. This incurs that the amount of neutron converter and scintillation material is not strictly controlled, and is likely to have different values in the individual scintillators. This problem can of course be minimized in various ways. One possibility is to use the emerging technology of 3D printing, by which the volume of the sensitive part of the scintillator can be controlled with high precision. Further, the scintillators can also be calibrated in laboratory measurements, and to use the calibration factors to correct the measured values.

However, a quantitative investigation of the effect of the different sensitivities of the scintillators, and the methods for correcting them, are still of interest. Even if the efficiency of the individual scintillators can be calibrated in laboratory measurements separately, these efficiencies may not be the same for the scintillators after they are mounted in the detector. The mounting material, the surrounding matrix, the optical coupling of the fiber to both the scintillator and the PM tube will affect the individual performances. This means that after the scintillators are mounted in the detector, their individual efficiencies become more complicated to determine.

On the other hand, one does not need to determine the absolute efficiencies of the four scintillators, only the efficiencies relative to each other, and elaborate methods to compensate for them. As mentioned earlier, the flux gradient is only determined to a constant scaling factor, whose value is not of interest. With scintillators of different sensitivities, this scaling factor would not be constant, but would depend e.g. on the detector orientation. The purpose of the correction is thus to make sure that a constant scaling is preserved, irrespective of the orientation of the detector. Such correction methods will be quantitatively investigated in the forthcoming. The correction method used in the current study as discussed below amounts to an in-situ calibration of the relative efficiencies, which can be even performed in a field measurement, and has to be executed only once.

In order to investigate the effect of having imperfect scintillators on the estimation of the flux gradient, 4 scenarios were considered. In the first scenario, one of the four scintillators is altered to have a lower atomic fraction of ^{6}Li and hence a lower efficiency. The second case is such that the detector defined in the first scenario is tested with a different orientation. In the third scenario, the gradient detector consists of 4 scintillators with a different content of ^{6}Li. In the fourth scenario, the detector with 4 different scintillators is studied adding a possible uncertainty to the initial position and the rotation angles.

Detector with one scintillator with different ^{6}Li content

In the first simulation, we chose an arrangement in which the two diagonally opposite scintillators D1 and D2 (see Fig. 4.9 for the notations) were lined up on a radial line, hence measuring the radial component of the gradient. Since the azimuthal component of the gradient is zero, we only need to consider these two scintillators (similarly to the case presented in section 4.2.1). Two positions of the gradient detector were chosen; one at 3 cm from the source, and another at 6 cm. In the first, the magnitude of the gradient is very low (as seen from the previous results) and is expected to reflect the maximum biasing effect of having different scintillator efficiencies. The other point lies at a position of high flux gradient, 6 cm from the source. The material composition of only one of the four scintillators (D1) was altered to have a lower efficiency than the other three. In the sensitive part of scintillator D1 the atomic fraction of ^{6}Li was reduced to 80% of its original value.

One single measurement in a point would give a biased value of the gradient, due to the different sensitivities of D1 and D2. One obvious way to compensate for the difference between D1 and D2 is to perform two measurements at the same location, the first one with the detector in its original orientation, and the second

one by rotating the detector by 180°, such that D1 and D2 swap their positions. By taking the average between the respective values of the gradients obtained from the two measurements leads to an unbiased estimation of the gradient.

The results of such a simulation are listed in Table 4.2. The calculated magnitude of the gradient is slightly underestimated compared to the ideal case (i.e., when both D1 and D2 have 100% efficiency). The underestimation of the magnitude of the gradient is expected, and is simply due to the lower total efficiency of the detector.

Similar to the measurements with perfectly identical scintillators, the absolute value of the gradient does not bear any significance. Again, the important fact is that the space dependence of the gradient obtained from this procedure is the same as that of the true gradient of the thermal flux. One way of investigating this in the present case is to see whether the ratio between the gradients obtained by D1 and D2 with equal and different sensitivities respectively, is constant, regardless of the position of the detector. The last row of Table 4.2 shows that the ratio between the two quantities indeed is very close to each other in the two different spatial positions, indicating that the method of compensating for the different scintillator efficiencies is applicable. For this procedure, the actual difference in the sensitivities does not need to be known.

Table 4.2: The effect of having one of the four scintillators at a lower efficiency on the estimation of the flux gradient.

Case	Position (Distance from the source)			
	3cm		6cm	
	Value ($\times 10^{-3}$)	Uncertainty (%)	Value ($\times 10^{-3}$)	Uncertainty (%)
Ideal case[a]	-1.43	3.45	-4.05	0.97
Non-ideal case [b]	-1.37	2.50	-3.91	0.71
Ratio[c]	958	1.21	965	4.23

[a]The ideal case of having the four scintillators at 100% efficiency.
[b]The case where D1 is at a lower efficiency (the atomic fraction of ^{6}Li was reduced to 80% of its original value).
[c]The ratio between the gradient estimated from the non-ideal case to the one estimated from the ideal case.

Detector with one scintillator with different ^{6}Li content and different orientation

One potential weakness of the above mentioned correction method is that, when the detector is inserted several meters into the guide tube of a fuel assembly, its orientation may not be possible to control (or to know) with 100% precision. This is valid for both the uncertainty of the original positioning, as well as the inaccuracy of the magnitude of the rotation. In order to quantify the effect of the uncertainty in the detector orientation, the same simulation was repeated with a rotation of the detector according to 175° instead of a perfect 180°. This slight difference in the rotation angle has a correspondingly little effect on the estimation of the gradient, as is seen in Table 4.3.

Table 4.3: The effect of added uncertainty in the rotation angle on the estimation of the flux gradient.

Case	Position	
	3cm	
	Value ($\times 10^{-3}$)	Uncertainty (%)
Ideal case	-1.43	3.45
Non-ideal case	-1.37	2.50
Non-ideal case $(175°)^d$	-1.37	2.48
^{d}The case where D1 is at a lower efficiency and the rotation angle was set to 175° instead of 180°.		

Detector with scintillators with different ^{6}Li content

A further step is a more general scenario in which both the measured components of the gradient are non-zero, and all four scintillators have different sensitivities. This latter was achieved in the simulations by leaving one of the efficiencies unchanged, and changing the efficiencies of the other three scintillators to various degrees. The atomic fraction of ^{6}Li was reduced for D2, D3 and D4 to 80%, 70% and 60% respectively, and kept at 100% for D1. The detector was again placed at 3 cm from the source but this time rotated by a 30° angle counterclockwise as the starting orientation. This experimental arrangement will result in both measured components of the gradient being non-zero.

Based on the foregoing, one might think that, to obtain an unbiased estimate of the two components of the gradient vector, it is sufficient to rotate the detector with 180°, such that D1 and D2, as well as D3 and D4, respectively, swap positions. Although with such a procedure one indeed gets a scaling of both components of the gradient which is independent of the measurement position, it is also easy to see that with this method, in general, the direction of the gradient would be determined incorrectly, i.e. it would contain a bias. This is because the scaling is linearly proportional with the total efficiency of D1 + D2 for one component, and with the total efficiency of D3 + D4 for the other. If these two total efficiencies are not equal to each other, then the two components will be scaled differently, leading to a bias in the determination of the direction of the gradient vector.

For an unbiased estimate of the direction of the gradient vector, the detector needs to be rotated three times with 90° at a time, i.e. rotating the detector by 90°, 180° and 270° from its original orientation. Then each scintillator will occupy each of the four angular positions once. The average value of the four reaction rates at each measurement position is then calculated, and the two components of the gradient are determined by taking the difference of the average reaction rates in the diagonally opposing positions.

The results of such a simulation are shown in Table 4.4 and Fig. 4.12. The estimated magnitude of the gradient with the four scintillators characterized by dif-

ferent fractions of ^{6}Li is smaller than in the case of four identical scintillators (see Table 4.4), which is a direct consequence of the fact that the efficiencies of 3 scintillators are reduced. On the other hand, despite of the efficiencies of the scintillators, the detector is capable of providing the expected direction of the gradient vector (see Fig. 4.12). Again, this procedure does not require knowledge of the individual sensitivities.
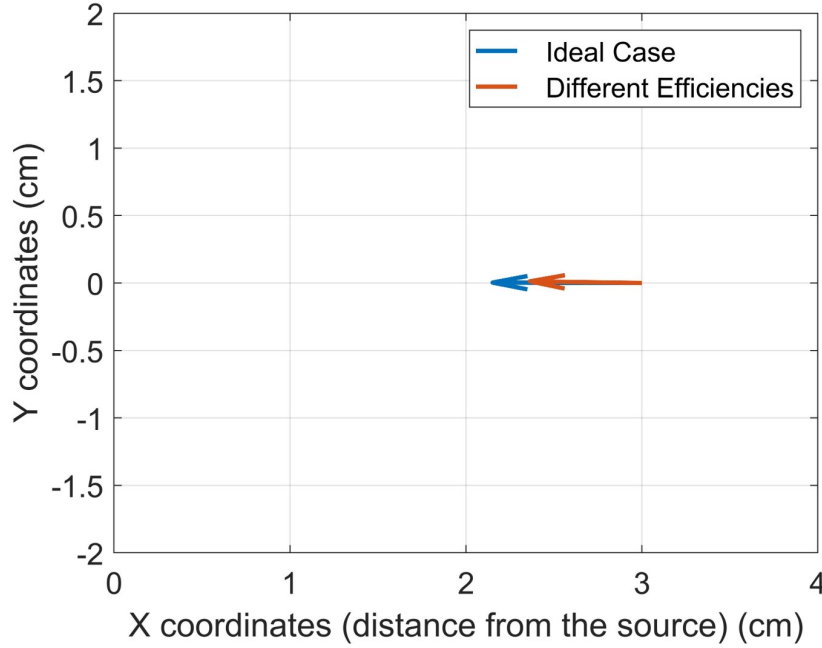

Figure 4.12: The effect of the different scintillator efficiencies (after correction) on the estimation of the direction of the gradient vector

Table 4.4: The effect of different scintillator efficiencies on the estimation of the magnitude of the flux gradient.

Case	Position	
	3cm	
	Value ($\times 10^{-3}$)	Uncertainty (%)
Ideal case[e]	-1.46	3.12
Non-ideal case[f]	-1.22	2.61
[e]The ideal case of having the four scintillators at 100% efficiency with the detector rotated by a 30° angle as the starting orientation. [f]The case where D2, D3 and D4 is at a varying lower efficiencies than D1.		

Naturally, a measurement procedure which requires four sub-measurements in one spatial position to obtain the two components of the gradient is not useful in practice. If each scintillator needs to be placed in each of the four angular positions, then in principle it would suffice to use only one scintillator, and put it sequentially in the four designated positions. In that case the problem with the different efficiencies would not occur, and there would be no need for an averaging procedure either.

However, the measurement of the gradient vector with one gradient detector without the need of rotating it is the method to be preferred. Apart from the option of manufacturing scintillators with equal efficiencies, another possibility is to make four separate measurements by rotating the detector three times, amounting to an in-situ relative calibration of the individual scintillator efficiencies. This is achieved such that the reaction rates of each scintillator in the four angular positions are added up individually. If all scintillators had the same efficiency, then these four total reaction rates would be equal. If the efficiencies are different, this will be reflected in the total reaction rates of the scintillators, taken in the four orientations. The total reaction rates are linearly proportional to the individual efficiencies. One such measurement with the original position plus three rotations of the detector can be used to determine the relative efficiencies, which can be used to correct the measurements in other points, without the need of rotating the detector.

The feasibility of this method was investigated using the previous simulation, in which the detector is placed at 3 cm from the source and the ^{6}Li content in the four scintillators is known (i.e., 100%, 80%, 70% and 60% of the nominal value for D1, D2, D3 and D4, respectively). The individual relative efficiencies of the detectors were estimated from the count rate ratios Di/D1, i = 1...4, see Table 4.5. These results show that the relation between ^{6}Li contents and relative performances of the scintillators is not linear. For example, the scintillator D4 has an efficiency of 81.2% with respect to D1, although its ^{6}Li fraction is only 60%.

Table 4.5: The estimation of the relative efficiencies of the four scintillators.

Relative Efficiency	Scintillators			
	D_1	D_2	D_3	D_4
D_1/D_i,i=1,..,4	100%	92.1%	87%	81.2%

Another measurement was simulated with the detector positioned at 6 cm from the source. This simulation was also made with the detector being rotated 30° counterclockwise as its initial position. The calculated reaction rates were then divided by the individual relative efficiencies derived from the previous step (see Table 4.5).

The resulting direction of the gradient vector is unfolded correctly with the calibration procedure, as shown in Figure 4.13.

Detector with scintillators with different ^{6}Li content and different rotations

The possible source of error of incorrect orientation of the detector was further investigated by comparing the direction of the gradient vector from the ideal case with two other cases as shown in Figure 4.14. The ideal case (represented by the blue arrow in Figure 4.14) is when the four scintillators have the exact same material composition and the detector is placed accurately at 30° as its initial orientation. The second case (red arrow) is when the four scintillators have the same material composition but an error was introduced to the initial orientation angle, i.e., the detector is shifted of 27° with respect to the x-axis. The third case (yellow arrow) is when the four scintillators have different atomic fractions of ^{6}Li (100%, 80%, 70%,
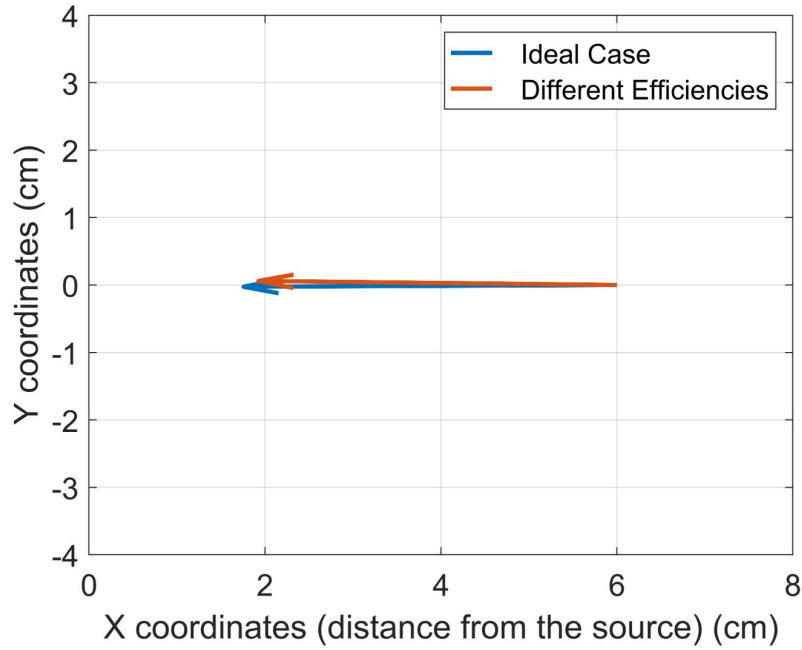
Figure 4.13: The estimation of the direction of the gradient vector from the calibrated detector at 6 cm from the source.

60% for D1, D2, D3 and D4 respectively) and an error was introduced to the rotation angles during the calibration. In this particular case the detector was rotated with 92°, 179° and 273°, instead of 90°, 180° and 270°, respectively.

The results show that an accurate reconstruction of the direction of the gradient vector is still possible despite the possible random uncertainty in the initial positioning or the rotation angles of the detector. It can also be noticed that the estimation of the direction was even more accurate in the case where the detector needed to be rotated four times than the case where the only source of error was in the initial positioning of the detector, which is probably due to the fact that random errors that arise from the four rotations tend to compensate for each other, which leads to a lower total error in the end.

The results of the reaction rates from the case described above, where the four scintillators had different material compositions and an uncertainty was introduced to the four rotation angles, were again used to estimate the relative efficiencies of the four scintillators. The results show that the presence of the uncertainty in the rotation angles had a very small effect on the estimation of the relative efficiencies of the four scintillators and the results were identical to the ones presented in Table 4.5. Hence, the method is still applicable for the calibration process and for the correction of the direction of the gradient at other spatial positions.

4.5 Conclusion

The design of a new neutron detector, capable of measuring the gradient of the neutron flux within a fuel assembly has been suggested and evaluated using
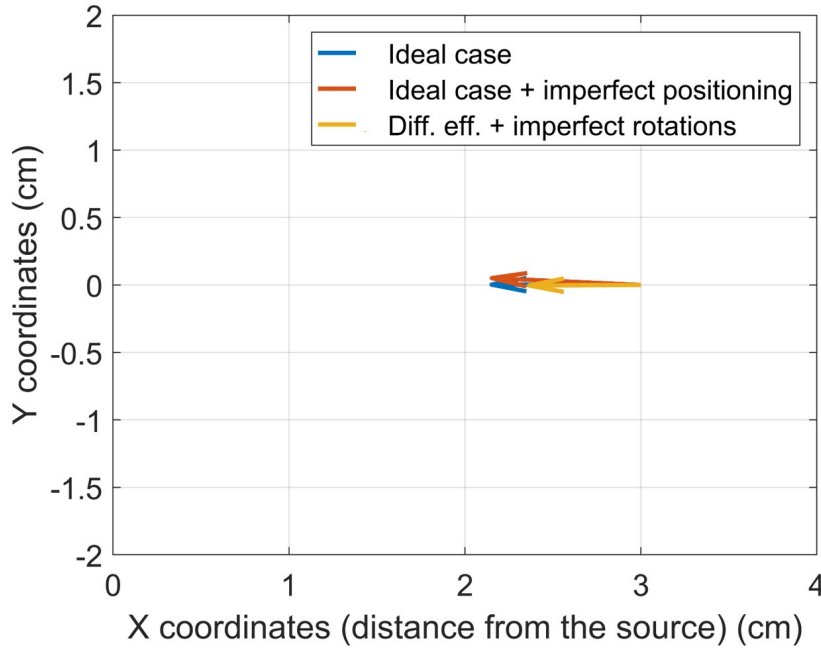
Figure 4.14: The effect of random uncertainties in the initial positioning and the rotation angles on the estimation of the direction of the flux gradient.

Monte Carlo simulations. The detector allows measuring the magnitude and direction of the neutron gradient vector within a multiplying or scattering neutron system. The detector is based on four thin LiF/ZnS(Ag) optical fiber-mounted neutron scintillators arranged in an aluminium matrix according to a rectangular pattern. The detector can be used to estimate the two components of the gradient of the scalar neutron flux, from the difference between the measurements provided by the diagonally-opposite pairs of scintillators.

The detector was modelled and its performances simulated in a hypothetical setup with a ^{252}Cf neutron source in a water tank. It was showed that determination of the gradient vector is feasible, i.e. the presence of the detector and associated shielding effects do not introduce significant distortion of the flux which would make the determination of the gradient inaccurate. It was also found that differences from the ideal composition of the scintillators and from their orientations with respect to the neutron source have a minor influence on the calculated gradient.

Future work is planned to study the detector in a full fuel assembly (instead of the simple case of a neutron source in a water tank) and its performance to identify possible local inhomogeneities. Manufacturing and testing of the proposed detector is also on the way.

Acknowledgement

performed jointly with our collaboration partners Alessandro Borella and Riccardo Rossa, the advisors of the joint PhD project at SCK CEN.

5. INVESTIGATION OF THE POSSIBILITY OF DETECTING SUBCOOLED BOILING IN THE UPPER PART OF A PWR THROUGH EVALUATION OF IN-CORE MEASUREMENTS MADE BY MOVABLE DETECTORS

5.1 Introduction

Detection and monitoring of subcooled boiling in the core of PWRs is of interest for detecting any onset of abnormal boiling and for verifying thermodynamic calculations of boiling rates. Apart from abnormal boiling, newer types of PWRs are expected to operate with a small boiling rate even in normal conditions, in accordance with Departure from Nucleate Boiling (DNB) margins.

As was already suggested in earlier EDF work [46], in-core neutron noise analysis may be a suitable method for detection and monitoring of the possible occurrence of such subcooled boiling. This is partly based on the experience one has with the application of in-core neutron noise analysis in BWRs for characterising flow velocities and indicate void fraction levels, or changes in these parameters. Naturally both the circumstances and the goals of the analysis, are different in a PWR from that of a BWR, yet some of the BWR experience, which we also utilised in earlier stages of the project, can be transferred with some modification.

The main objectives of boiling monitoring in PWRs is the detection of boiling, determining the onset point of boiling, and possibly to quantify the void content, at least on a relative scale, which might need calibration. The idea of the detection of boiling and determination of its onset point has already actually occurred in the immediate past Stages of this project, when, in order to determine the void velocity profile, the onset point of boiling was needed [26, 17]. We suggested using a TIP detector, and taking measurements at various axial positions. The onset of the boiling would be indicated by an increase of the RMS (root mean square) of the detector signal, as well as the change of the shape of its APSD. Another possibility is to cross-correlate the TIP signal with that of the lowermost LPRM. In PWR measurements, a movable detector would be used in the top region of the core. Only the change of the RMS and the shape of the APSD can be used in a PWR, no cross-correlation with another detector in the same radial position (in the same detector guide tube) is possible. No such measurements have yet been made in this project, and with the phasing out of R1, there is no possibility either for new BWR measurements in the project. Such measurements may possibly be performed in the future by our Swiss collaborating partners at the Paul Scherrer Institute and EPFL.

In the EDF work, use was made of the fact that since in a PWR one has to do with nucleate boiling, the flow structure is simple bubbly flow, and no complicated flow regimes will occur. Hence, attempts were made to develop models of the in-core neutron noise, based on simple bubbly flow with homogeneously distributed bubbles randomly generated in the flow. In this area we have vast experiences from previous Stages, where we developed an in-house model for simulating such a simple structure

of the two-phase flow with probabilistic (Monte-Carlo) methods, and were able to generate the induced neutron noise by numerical simulations [22, 47, 48, 23, 49]. Experience from that work is still accessible to us, and one of of the project was to adapt it to the present problem.

Previous experience shows that the most effective way of the diagnostics of propagating perturbations is the cross-correlation and coherence between two axially displaced detectors. If the boiling starts below the lowermost detector, a large coherence will occur, and the propagating character of the two-phase flow will lead to a peak at a delay time $\tau > 0$ of the cross-correlation, and a phase of the CPSD (cross power spectral density) depending linearly on the frequency. These are unmistakable, and easily detectable footprints of the presence of subcooled boiling.

However, experimental verification or application of this method is not possible in the Ringhals PWRs, since only one movable detector can be inserted into one detector guide tube at a time. Hence, in the present work, we explore the possibilities of using a single detector APSD (auto power spectral density) as an indicator. In such a case the only possibility of detection is if the APSD shows a noticeable increase at the axial elevations above the onset of the boiling. To this order we investigated, through the adoption of the previous simulation model of two phase flow to the subcooled boiling conditions, the axial dependence of the APSD in the presence of boiling. The verification and/or experimental application of this method would require relatively long (> 30 minutes) measurements at each axial elevation, in a sufficient number of positions. However, in this Stage this option was not available either. An in-core measurement with a total of 7 axial positions was performed, and the results of this measurement were used as a first estimate of the occurrence of subcooled boiling. The details and the results of the simulation model are given in the subsequent sections, and finally a comparison with the experimental results is made.

5.2 Basic principles

Previous experience with BWR in-core noise shows that the presence of propagating bubbles manifests itself most clearly in form of the presence of a linear phase of the CPSD between two axially positioned detectors, which expresses the phase delay between the two detector signals. This is illustrated in Fig. 5.1 below, which shows measurement results made in the German Lingen BWR [50]. The slope of the phase yields the transit time between the two detectors. Since in our case such an information is not possible to collect from measurements, it is more interesting to know how the APSD behaves at different axial elevations. This is shown in Fig. 5.2, taken from the same measurements. It is this latter feature which we will try to reconstruct and quantify in our simulation work, described in the next section, in order to facilitate the detection of subcooled boiling from meassurements with a movable detector.
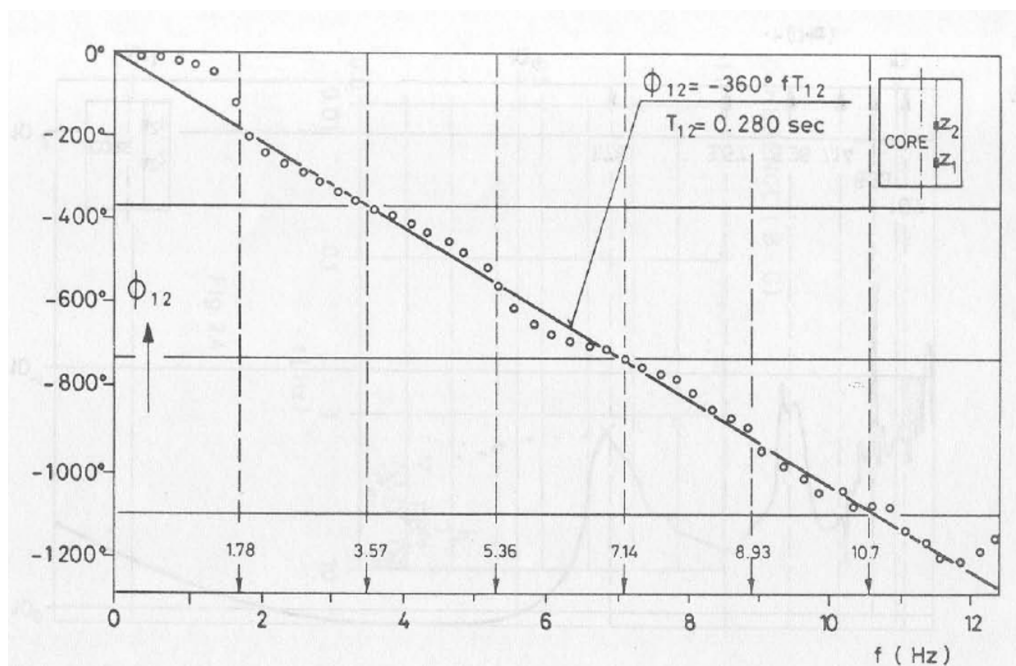
Figure 5.1: Phase of the CPSD between two axially displace detectors from measurements in the German Lingen BWR [50]
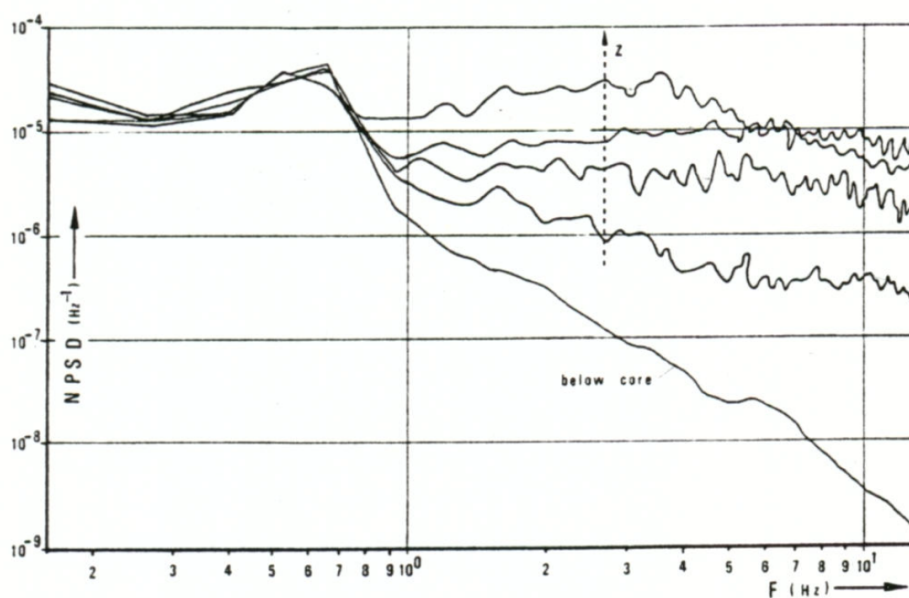

Figure 5.2: Demonstration of the increasing of the APSD of a movable ionisation chamber with axial elevation above 1 Hz in the German Lingen BWR [50]

5.3 The simulation model

The details of the simulation model of BWR noise, used in our previous work, which was the starting point of the present work, is described in detail in the previous publications (see e.g. Refs [23] and [49]. In contrast to our previous Monte Carlo model for simulating boiling in a BWR channel, for simplicity, in the current simulations, the distribution of the bubble generation in both radial and axial directions was taken as homogeneous, and then the bubbles are allowed to propagate upwards with a certain velocity profile. The axial velocity profile of bubbles can easily be estimated from the following steady-state mass conservation equation written for the mixture density between the vapour and the liquid phases of the coolant as:

$$\frac{\partial \rho_m(z)\, v_m(z)}{\partial z} = 0 \tag{5.1}$$

With this, one gets for the axial bubble velocity the simple expression

$$v(z) = v_m(z) \approx \frac{v_0}{1 - \alpha(z)} \tag{5.2}$$

where $v_0 = v_l$ is the velocity of the liquid phase at the channel inlet. In the last equation the second term in the denominator is neglected due to its smallness.

5.4 Details of the flow simulation

As a starting point, a two-dimensional model of a heated channel, representing the vertical cross-section of the interpin area of a fuel assembly was chosen. Only one dimension was assumed for the radial direction, denoted by x, and the axial direction, in which the two-phase flow is propagating, was denoted by z. The bubbles are represented as 2-D circles in this model. The coordinates of the bubble centres are generated by random sampling methods along the x and z directions, assuming uniform distributions. To conform to the real case of subcooled boiling in a PWR assembly, the generation of the bubbles started at the upper part of the core, at some onset point $z = z_0$ but below of the fourth LPRM in a detector tube, and was restricted to the area between z_0 and the top of the core at $z = H$.

It is worth noting that overlapping between different bubbles is not allowed in the present model, but this is not a severe condition in view of the sparse bubbly flow character of the subcooled boiling. The bubble diameter was set to $d_b = 0.2$ cm while the diameter of the simulated channel was chosen to $D = 2$ cm. The height of the channel corresponds to the length of a PWR fuel assembly, i.e. to $H = 360$ cm and the onset point is selected to be $z_0 = 300$ cm. The bubble inlet velocity is taken to be $v_0 = 200$ cm/s, corresponding to a typical PWR inlet flow velocity under normal operational conditions. To provide proper detection intensity and time resolution, the time step in the data processing was selected equal to

$$\delta t = \frac{d_b}{5\, v_0} = 0.00002 \text{ sec}, \tag{5.3}$$

which gives an opportunity to detect the same bubble up to 5 times while it bypasses the detector aperture.

The simulation starts with generating 100 bubbles at $t = 0$ and proceeds with random injection of 1 new bubble at each consecutive time step. Since the transient part of the simulation is not of interest here, the recording of calculated void fluctuations as well as the corresponding induced neutron noise is started after 20 seconds of the simulation, which eliminates any transient effects. The total simulation time is limited to 260 seconds, which is somewhat longer than the duration of an in-core measurement at Ringhals-3, but was chosen to improve the simulation statistics. In order to estimate the void fraction generated by the simulations, the entire 2D $(x - z)$ plane of the simulated channel is divided into horizontal layers, each of the size of δz=0.09 cm. The void fraction is then estimated for each axial position between the layers and for each time step by calculating the total intersection length between the bubbles and the corresponding layer boundary. In order to evaluate the void fraction, the total intersection length of bubble crossings for each axial level is weighted with the diameter of the channel. Since the goal of the simulations is to emulate subcooled boiling, the void fraction should not exceed the typical value of the void fraction for such a flow regime. This was achieved by adjusting the bubble generation rate so that the maximum axial void fraction did not exceed $\alpha \approx 0.15$ - 0.2.

The pile-up of the bubbles leads to an axially increasing void fraction, which also leads to an axially dependent velocity profile. A substantial effort was made to find input data to the simulation model which led to realistic void and velocity profiles. The axial velocity $v(z)$ is calculated for each axial position separately via Eq. (5.2). It is worth mentioning, that the real bubble velocity is usually a continuous function in space. However, due to spatial discretisation, the velocity in the present model is evaluated only in a discrete number of spatial points. Furthermore, due to the random character of bubble production, and in addition owing to the fact that the bubbles are born instantaneously with full size, the axial velocity also becomes a random quantity. This also incurs that some bubbles at lower axial elevations can move faster than those with a higher axial position, which is unrealistic. To tackle the above-mentioned problem, the velocity profile is fitted with a third order polynomial function just after the system reaches a steady state. Obviously, in such a case the velocity becomes a continuous function in space.

It turned out that the simulation of the sparse flow introduced substantial difficulties. Due to the sparseness and smallness of the bubbles (e.g. with a bubble size of 2 mm) a very high spatial and temporal resolution was necessary in the simulations to get results, which in turn led to huge data files. Therefore, some trade-off had to be found between the parameters, such as the bubble size and the sampling time. The resulting void fraction and velocity profile with the optimalised parameters are shown in Fig 5.3.

As a test of the model, the CCF was calculated between two "bubble detectors", i.e. between the fluctuations of the void fraction between two axial point, both situated above the onset of the boiling, at z = 320 and 340, respectively (Fig 5.4. The time peak of the CCF corresponds with a good precision to the transit time of the bubbles between the two detectors, which can be calculated from the velocity profile.
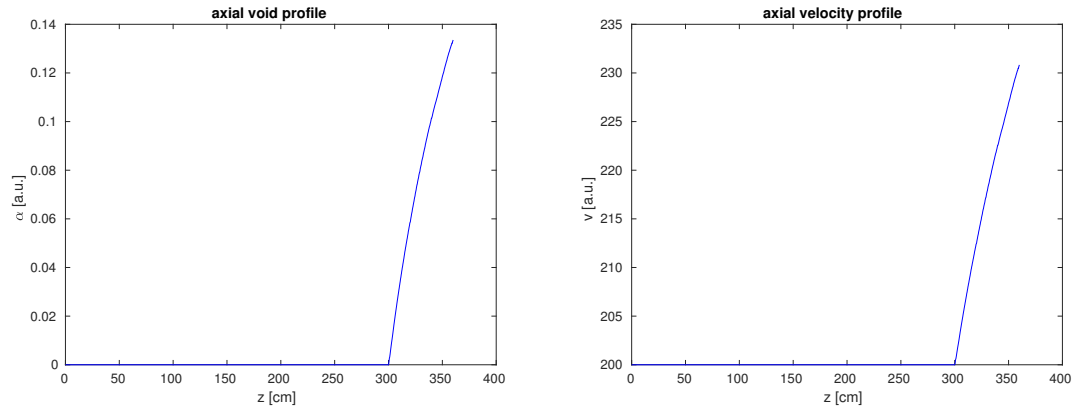
Figure 5.3: Axial dependence of the void fraction (left) and void velocity (right) in the simulation model
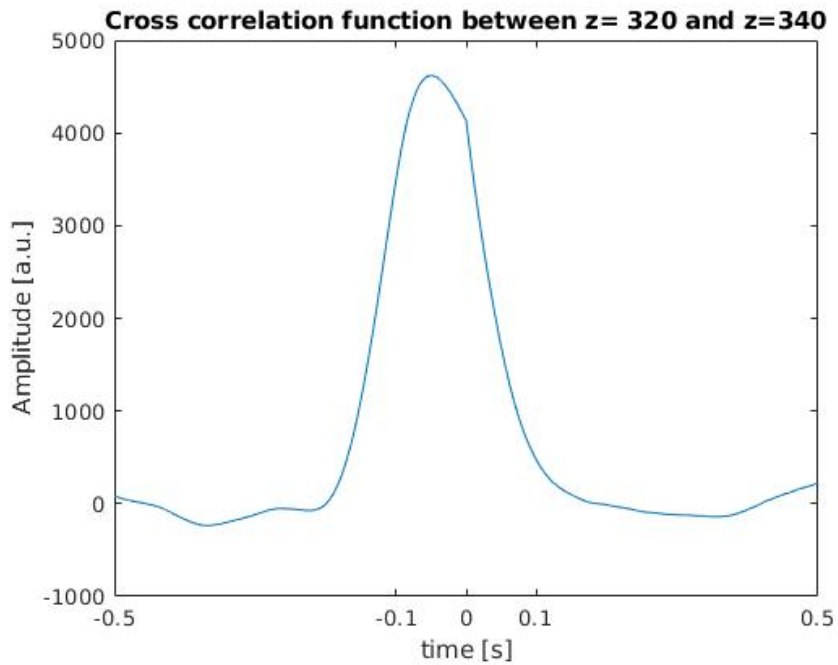

Figure 5.4: Cross correlation function of the simulated signals between two detectors at z = 340 and z = 320 cm.

Before turning to the calculation of the induced neutron noise, a question was investigated which has been all the time tacitly assumed in the noise literature. Namely, whether the induced void fluctuations, as a noise source, can indeed be considered as white noise, and whether the relationship between the average void fraction $\alpha(z)$ and the rms of the induced void fluctuations $\delta\alpha(z,\omega)$ is indeed linear. On the face of it, due to the generation of the bubbles with a Poisson statistics, the answer would be "yes". However, this only concerns the bubble birth process. The fluctuations of the void fraction at one point are affected by all bubbles generated at lower elevation, and the bubble arrival process to a given point is non-Poissonian. Hence this question is far from trivial. The significance of this question is that whether the increase of the spectra above 1 Hz in Fig. 5.2 can indeed to be attributed to the increase of the *average* void fraction.

The answer is shown in Figs. 5.5 and 5.6. It is seen from 5.5 that up to about 100 Hz, which is beyond the break frequency of the neutronic transfer, the void fluctuations constitute a white noise to a good approximation. In addition, the amplitude increases with the axial elevation. The correspondence between the axial dependence of the average void fraction and the rms of the void fraction fluctuation, displayed in Fig. 5.6 shows that the space dependence of these two quantities is very similar to each other. This result bears significance to the development of theoretical models of subcooled boiling, which is planned in the continuation, but also justifies, the first time, the use of this assumption in earlier BWR work.
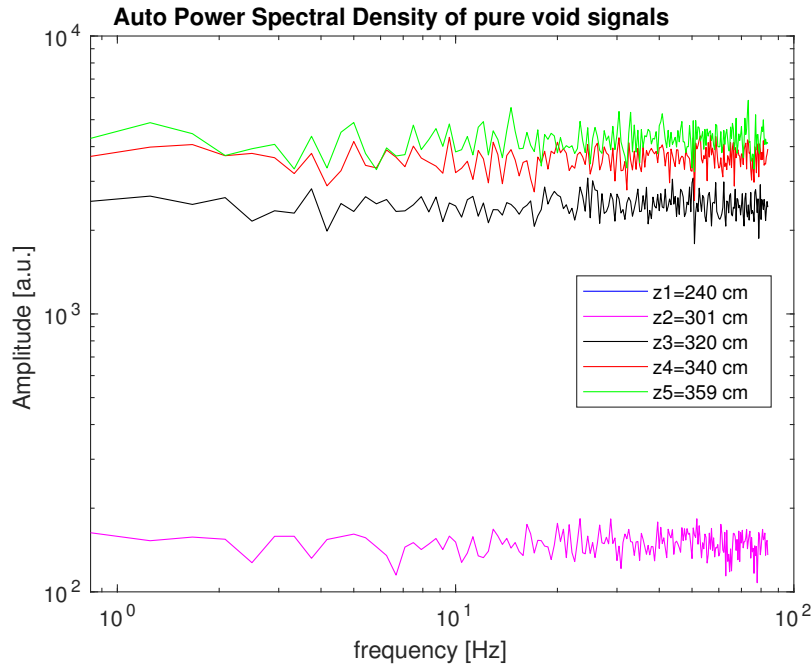

Figure 5.5: APSD of the pure void signals at different axial elevations

5.5 Calculation of the simulated neutron noise

As in the previous work, the space-time dependent simulated void fluctuation signals are converted into measured neutron noise by taking these as the noise source,
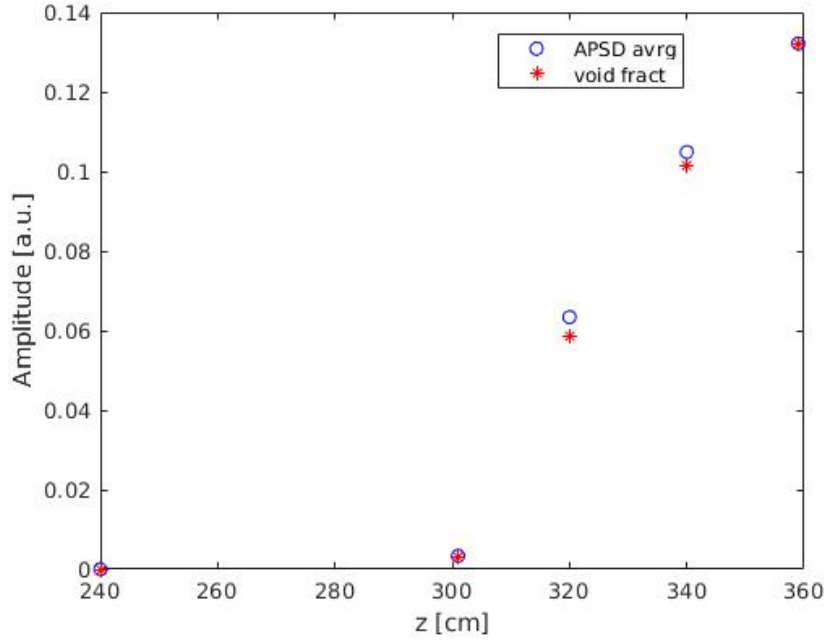
Figure 5.6: Comparison of the axial dependence of the average void fraction with that of the rms of the void fluctuations

and integrating them with the reactor transfer function. Due to the strong influence of bubbles in the case of the BWR work, and the possibility of determining transit time of the flow between the axially placed detectors, the focus was only the local component of the noise. For this reason, only the local component of the neutron noise was used in the calculation of the induced neutron noise. For the local component of the transfer function, a simple exponentially decaying function was chosen.

This was sufficient when the main objective was the determining of the transit time between detectors, in order to reconstruct the velocity profile. Since in the present case, in the detection of subcooled boiling only one detector and its APSD can be used, a more involved simulation is necessary. Namely, in addition to the calculation of the local component of the neutron noise, the global component, induced by the same perturbation, was also calculated, and the final conclusions were drawn from the total noise (the sum of the local and the global components).

The calculation of the local component of the corresponding normalized neutron noise is generated through the spatial convolution between the void fraction signals and the local component of the transfer function as

$$\frac{\delta\phi_l(z,t)}{\phi_0(z)} = \int_0^H e^{-\lambda(z-z')} \, \delta\alpha(z',t) \, \mathrm{d}z' \tag{5.4}$$

where $\delta\phi_l(z,t)$ denotes the local component of the neutron noise due to void fraction fluctuations, $\delta\alpha(z,t)$ is the fluctuation of the simulated void fraction signal at axial position z, and λ is the range of the local component, which in this work was set to 0.3 cm^{-1}. $\phi_0(z)$ is the static flux, which was assumed to have a simple cosine shape, with an extrapolation length.

In writing down Eq. (5.4), use was made of the fact that in the frequency range of interest, up to at least 100 Hz, the local component of the frequency dependent transfer function, connecting the noise source with the induced neutron noise, is independent of frequency. Hence the expression of the spatial convolution of the noise between the noise source and the local component of the transfer function, which is valid in the frequency domain, can be inverted back to the time domain. In general, the induced noise can be written as a spatial convolution of the noise source and the transfer function only in the frequency domain. However, if the transfer function is independent of frequency, one can take the inverse Fourier transform of both sides of the equation, arriving to Eq. (5.4) in the time domain. This is essential, since the simulations can only be made in the time domain.

The above fact is also used for the calculation of the global component, which for simplicity is assumed to be equal to the point kinetic component. The normalised point kinetic component is given as the product of the frequency dependent zero power reactor transfer function $G_0(\omega)$, and the Fourier-transform of the reactivity fluctuations. However, at the so-called plateau frequency region (between approximately 0.5 - 15 Hz), which is the major frequency region of interest, one can use the approximation $G_0(\omega) \approx 1/\beta$, where β is the delayed neutron fraction. With these approximations, one has

$$\frac{\delta\phi_g(z,t)}{\phi_0(z)} = \frac{\delta\phi_g(t)}{\phi_0(z)} = -\frac{k}{\beta}\frac{\displaystyle\int_0^H \phi_0^2(z')\,\delta\alpha(z',t)\,\mathrm{d}z'}{\nu\Sigma_f \displaystyle\int_0^H \phi_0^2(z')\mathrm{d}z'} \tag{5.5}$$

where k is the scaling factor between the void fluctuations and the fluctuations of the absorption cross section. As is well known, as Eq. (5.5) also shows it, the normalised point kinetic component is space-independent.

With the above, the total induced normalised noise $\delta\phi_t(z,t)$ can be written as

$$\delta\phi_t(z,t) = \frac{\delta\phi_g(t)}{\phi_0(z)} * SF + \frac{\delta\phi_l(t)}{\phi_0(z)} \tag{5.6}$$

where SF stands for scaling factor between the global and local components. This factor, or rather the full transfer function should ideally be calculated from two-group diffusion theory, which gives the local and the global components in absolute values without the need of scaling them to each other. In this preliminary study we only approximated these components by assuring their functional form being realistic. In this study we selected this factor being equal to 0.23, such that the ratio of the local and global components have approximately an equal weight, which is a plausible assumption for a PWR.

5.6 Results of the simulation for the neutron noise

A number of simulations of the flow, and subsequent calculations of the induced neutron noise as well as void fraction profiles have been performed. As a starting point, 260-second long void fraction signals were generated by the Monte Carlo two-phase flow model. When simulating the induced neutron noise, these were performed

at five different axial levels at the same radial position. The selection of detector positions was made in such a way that some of detectors are placed in the non-boiling area (below the onset of boiling) and some are located in the boiling area (above the onset of boiling). Choosing detector positions below the onset of the boiling was made mostly for testing purposes. The detector locations are given in the first column of Table 1 below. For the convenience of calculations, void fraction signals were recorded in a binary form where "1" indicates the presence of a vapour bubble in the detection point, and "0" designates the presence of water in the position in question. The detection of vapour bubbles is controlled by estimating the distance between a bubble centre and a detector.

Table 5.1: Detector positions in the simulations

	Detector position
5	$z_5 = 359$ cm
4	$z_4 = 340$ cm
3	$z_3 = 320$ cm
2	$z_2 = 301$ cm
1	$z_1 = 240$ cm

Subsequently, the power spectral densities for each of the five detectors are calculated by using standard FFT methods. The results of the calculations of the neutron noise are shown in Figs 5.7 - 5.9. Since, similarly to the evaluation of the measurements, the results are normalised to the static flux, as mentioned before, the amplitude of the global (point kinetic) noise is independent of the axial elevation (Fig. 5.7). This is seen by the fact all curves are identical, only one is seen in the figure. Even the normalised noise at the elevation $z = 240$ cm, which is below the onset of the boiling, is identical with the normalised noise at the other positions.

On the other hand, the amplitude of the local noise increases monotonically along the axial elevation (Fig. 5.8). The fact that there is a small local component even at $z = 240$ cm, which lies below the onset of the boiling, depends on the fact that the exponential decay of the local component of the transfer function reaches also to this point, although with a three order of magnitude less amplitude. The frequency dependence of the APSD of the local component is also much flatter, i.e. its break frequency is also much higher than for the global component, which is in line with the former BWR measurements. Hence in this respect, the simulations conform with previous experience from the BWR measurements.

The total noise, shown in Fig. 5.9, summarizes this behaviour, and resembles to that in Fig. 5.2 for the BWR case, but also showing some deviations, which are natural since the two cases are not identical. The flattening of the spectra at frequencies above 1 Hz is not so explicit as in the BWR case, which is due to the fact that the increase of the amplitude of the noise source is also much more moderate than in the BWR case.
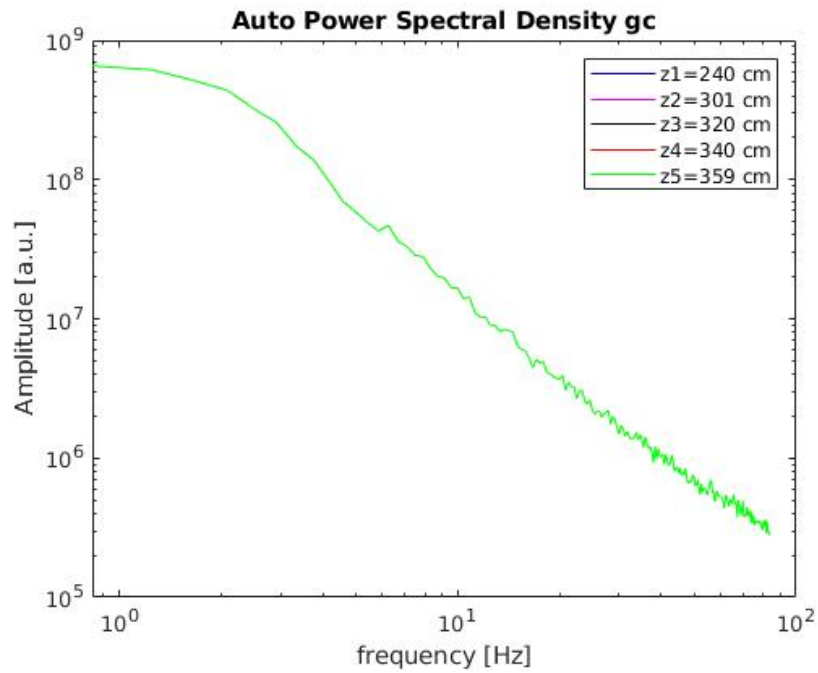
Figure 5.7: The APSD of the global component of the simulated neutron noise at the five different axial elevations, as a function of the frequency.
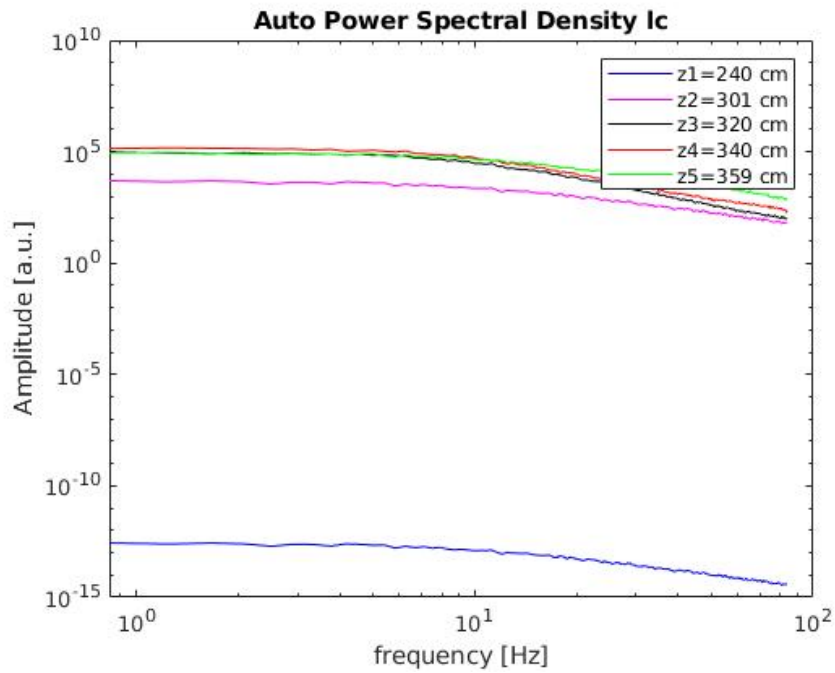

Figure 5.8: The APSD of the local component of the simulated neutron noise at the five different axial elevations, as a function of the frequency.
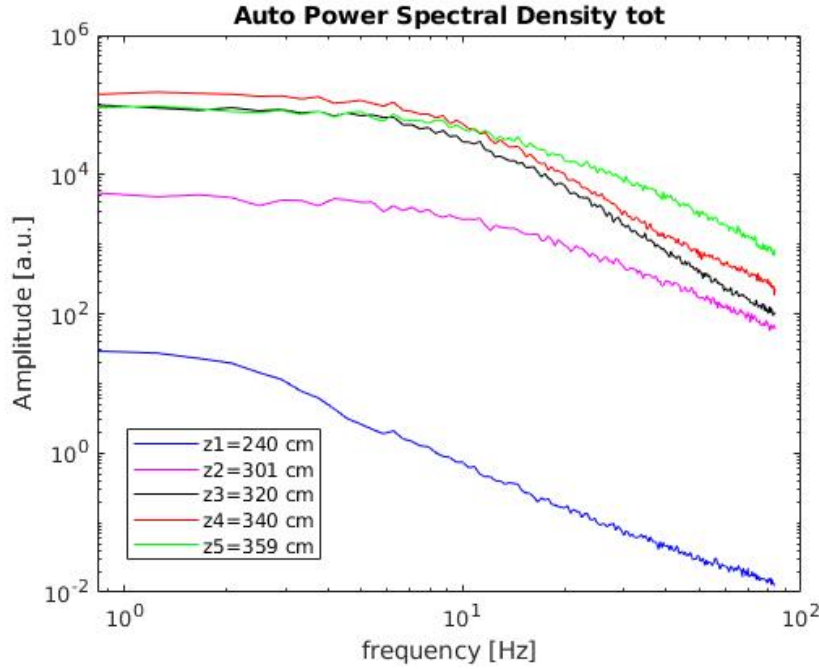
Figure 5.9: The APSD of the total (global + local component) simulated neutron noise at the five different axial elevations, as a function of the frequency.

Finally, the quantity most interesting from the point of view of the diagnostics, the axial dependence of the RMS (root mean square) of the detector signals, as a function of the axial elevation, is shown in Fig. 5.10. The fact that there are substantially more points shown here than the previously described five detector positions depends on the fact that at the lower half of the core, the effect of the local component is zero, due to the large distance to the location of the noise source. Thus, at these points, only the global (reactivity or point kinetic) component exists, which does not need to be re-calculated, since it is the same everywhere in the core.

Therefore, as the figure shows, up to the elevation which is below the onset point of the boiling, at a distance of the range of the local component, the normalised RMS value is constant. After that, when the effect of the local component starts, the RMS value starts to increasing monotonically. In case there is only one detector available, this is the only indicator one can use to detect subcooled boiling.

5.7 Comparison with experiments

As the above discussion shows, with one single detector in the core at a time, there are two possibilities to detect subcooled boiling with measurements in the upper part of the core. One is to observe an increase of the APSD at higher frequencies for the uppermost detector(s), basically in the form that above the break frequency of the global component, the decay of the APSD with increasing frequencies becomes slower at higher axial elevations. This was seen both in the simulations, as well as in the BWR measurements (Fig. 5.2). The other is the increase of the RMS of the signal (the integral of the APSD over all frequencies). This latter is only indicated by the simulation results (Fig. 5.5), it has not previously been investigated
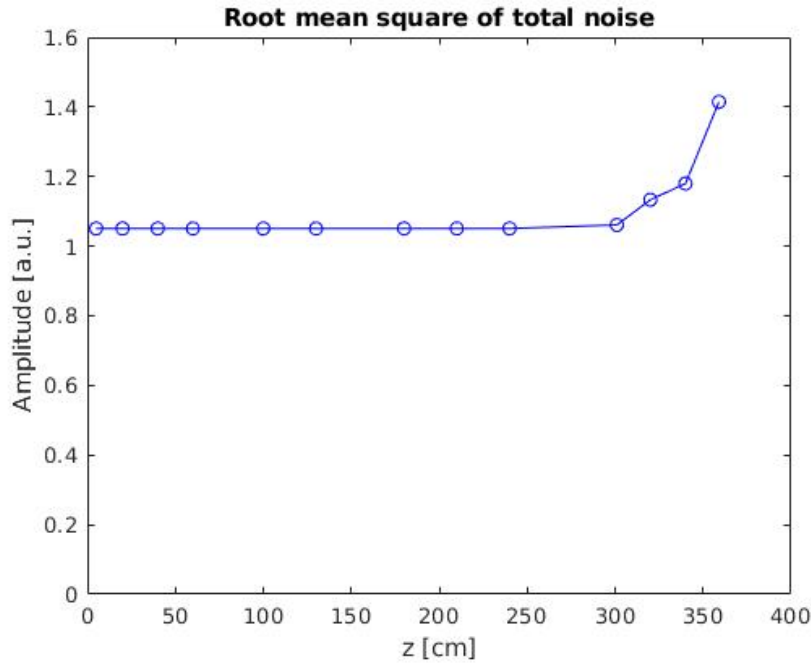
Figure 5.10: The axial dependence of the normalised root mean square (RMS) of the total neutron noise at various elevations.

from measured data. These two indicators are not completely independent, but the information content they carry is not identical either.

However, utilisation of the above two indicators is hampered by the fact that in PWRs, a large number of other noise sources, mostly related to vibrations of the various components (fuel assemblies, control rods, thimble tubes, core barrel etc.) are present. As a consequence, the spectrum is by far not as smooth as in the case of a BWR, where the wide-broad noise of the boiling process dominates (as seen in Fig. 5.2). Rather, the APSD of the in-core detectors (and even that of the ex-core detectors), features a number of resonant peaks, corresponding to the eigenfrequencies of the various vibrating components, as was seen in the in-core spectra of Chapter 2, Figs. 2.3 - 2.6. These peaks occur at low and intermediate frequencies, practically over the whole plateau region of the zero power transfer function $G_0(\omega)$ and with a high amplitude. Hence, these peaks will dominate the axial dependence of the RMS of the signals, suppressing the possible small contribution from the incipient boiling at the high axial elevations. In addition, the possible increase of the "tail" of the spectra is not so visible either, since the break frequency of the global component is also masked by the presence of the peaks.

Yet another problem is that in these in-core measurements, only the AC component (the fluctuating part) of the signals was registered, but not the DC component (the mean value). This means that, unlike in the ex-core measurements, there is no possibility to normalise the noise spectra. As a consequence, the axial dependence of the static flux, which is not constant, is reflected in the measurement, representing a further complication. The axial dependence of the static flux can be discerned from the top plots of Figs 2.11 - 2.14, showing the time series of the measurement

when the movable detector travelled through the whole elevation of the core. The envelope of the noisy signal reflects the axial dependence of the static flux, which is not constant. As a consequence, the axial dependence of the global component will not be constant either, and hence a small possible increase of the RMS values, as predicted in the simulations (see Fig. 5.10) will not be possible to see, even it it should exist.

As an illustration, the spectra of the in-core detector A (N12) in the six axial points (from bottom to top) are shown in Fig. 5.11 in a representation different from that in Chapter 2, namely in a "waterfall" or "ridgeline" type representation. The advantage of such a representation is that it is much easier to identify which curve corresponds to which axial position, without the need of a label for each curve.
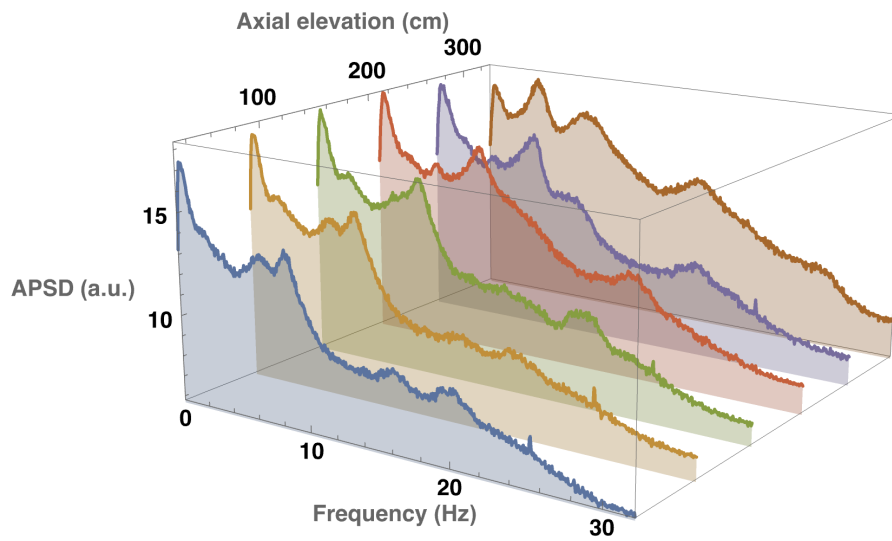

Figure 5.11: APSDs of the signals of detector A (N12) in six axial positions, from close to the bottom ($z = 30$ cm, leftmost) to close to the top of the core ($z = 330$ cm, rightmost curve). (Note that the quantitative value of z in this plot does not conform with the Ringhals convention of denoting positions measured from the top of the core.)

As a curiosity, even a stereographic picture of the same figure, which can be seen in real 3D with depth perception, viewing it with the so-called "cross-eye view" [51, 52], is included (Fig. 5.12).

These plots serve as an illustration of the difference between a BWR and a PWR what regards the smoothness of the spectra as a function of the frequency. Neither in these figures, nor in the ones with the traditional representation (Figs. 2.3 - 2.6) can one notice an increase of the spectra at higher frequencies for the uppermost position. This is the same for all four detectors, as an inspection of the figures of Chapter 2 shows.

What regards the dependence of the RMS value on the axial position, the fact that due to the lack of the mean value (DC component), the spectra cannot be normalised, these values cannot be properly used for discovering a possible increase of the RMS value of the signals at higher (basically at the highermost) elevation.
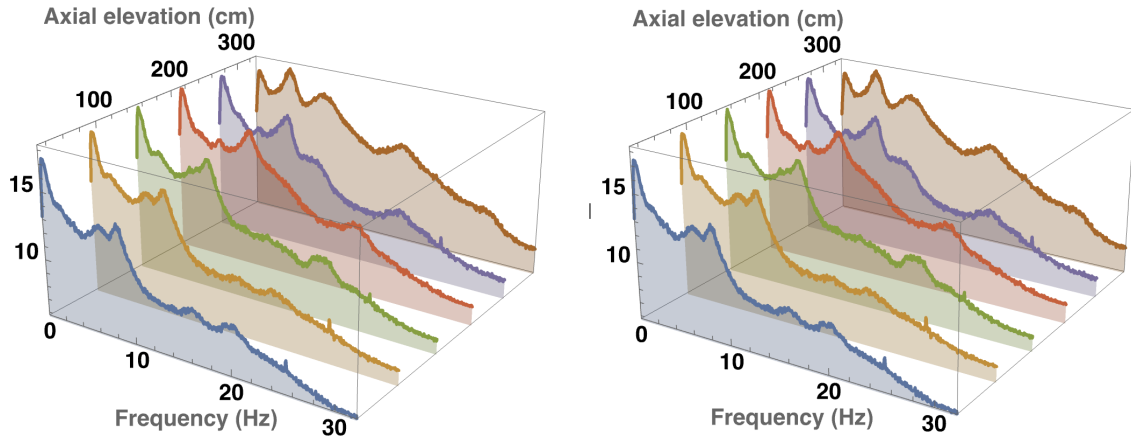
Figure 5.12: A stereographic view of the APSDs of the signals of detector A (N12) in the six axial positions as above.

This is illustrated in Fig. 5.13, which shows the axial dependence of the RMS of all four in-core detectors at the 7 axial positions from Measurement 1. Here, the APSD from the extra measurement at 60 cm from the top was also accounted for. It is
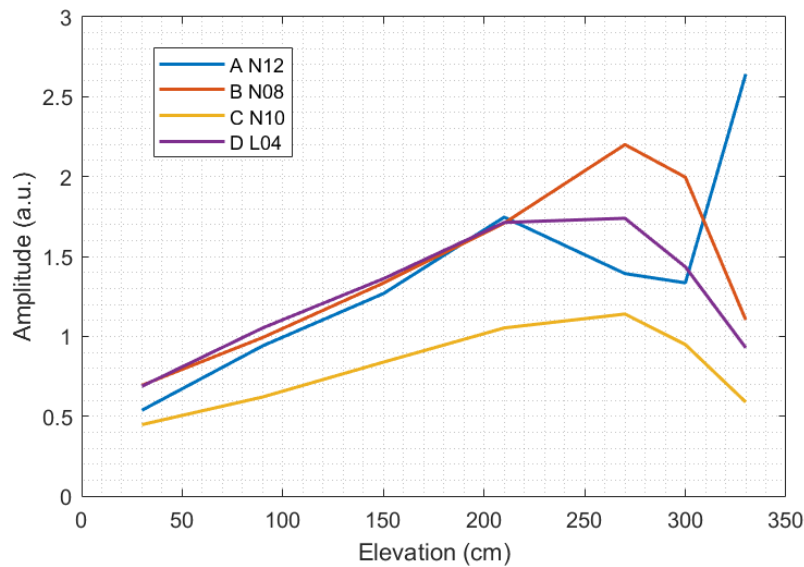

Figure 5.13: The axial dependence of the RMS of the signal of the void fluctuations

seen that there are no regions where the RMS values are constant in space, not even at low axial elevations. Rather, they show a somewhat asymmetric cosine shape around the core centre. In this respect they resemble quite a lot to the envelope of the time series of Measurement 2 in Chapter 2, upper part of Figs 2.11 - 2.14, in that the maximum of the envelope of the time signals is in the upper part of the core.

However, as mentioned before, these measurements contain of course the effects of a number of other noise sources, such as fuel, control rod and thimble tube

vibrations. In particular, the sudden increase of the signal of detector A (N12) at the highest elevation, is not an indicator of subcooled boiling, rather it is due to the appearance of a peak at 5 Hz with high amplitude at the axially highest measurement point, as is also seen in Fig. 5.11. It is noted that in the evaluation of Measurement 2 with the wavelet technique, the appearance of a peak around 5 Hz in the signal of detector A was also noticed close to the top of the core (lowermost plot in Fig. 2.11),

One could add that detector A is at the rather peripheral core position N12 with low power, so the possibility of subcooled boiling is low in that position anyway, which corroborates the judgement that the increase of the RMS at the top of the core is not a sign of subcooled boiling.

5.8 Conclusions

The simulations presented in this Section, inspired by some early work by EDF in this area, suggested some possibilities of detecting subcooled boiling from the APSD of single detector signals. The increase of the RMS value of the detector signals, and the increase of the amplitude of the high frequency tail of the of the APSDs were pointed out as possible indicators of subcooled boiling. None of these indicators showed sign of subcooled boiling in the measurements we had access to. This may be partly due to the fact that the in-core detectors whose signals were available, were in relative peripheral positions, where the probability of the subcooled boiling is low. In additin, since the DC component of the in-core detectors was not registered, application of one of the two indicators (the axial dependence of the RMS value) could not be effectively applied. Finally, the presence of the many resonant frequencies in the in-core spectra of a PWR, due to various vibration phenomena, makes the detection of the subcooled boiling even more complicated.

The overall conclusion is that detection of subcooled boiling with one single detector in one channel, which is restricted to the behaviour of the APSD, is not an effective way of detecting subcooled boiling. One possible remedy would be to consider taking measurements with two movable neutron detectors in adjacent channels, placed at different axial positions, both in the upper part of the core, but at different axial positions. If the two detectors are closer to each other than the range of the local component, and there is a correlated boiling in both assemblies, then their CPSD should "sense" the transit time between the two axial elevations. Finally, measurements at the bottom of BWRs, which in some sense are similar to the subcooled boiling in a PWR, could be performed by our collaborating partners at the Paul Scherrer Institute and at EPFL. From the theoretical point of view, the simulation model could also be refined, e.g. by developing a theoretical model which is capable of handling the axially varying void content and velocity profile.

6. PROPOSAL FOR 2022-23

No concrete proposal is given, due to the planned revision of the feasibility and possible changed forms of the collaborative project between Chalmers and Ringhals. A possible continuation could include the following points.

1. Analysis of vibrations of thimble tubes with axially dependent in-core measurements in various radial positions, by wavelet transform and wavelet filtering methods.

2. Evaluation of new ex-core measurements for beam, reactivity, shell and tilting mode vibrations in R3 or R4.

3. Further investigation, with method development and measurements in foreign BWRs of the possibility of detecting subcooled boiling in the upper part of a PWR.

4. An overview and summary of the collaborative project on diagnostics and monitoring between Chalmers and Ringhals 1995 - 2022.
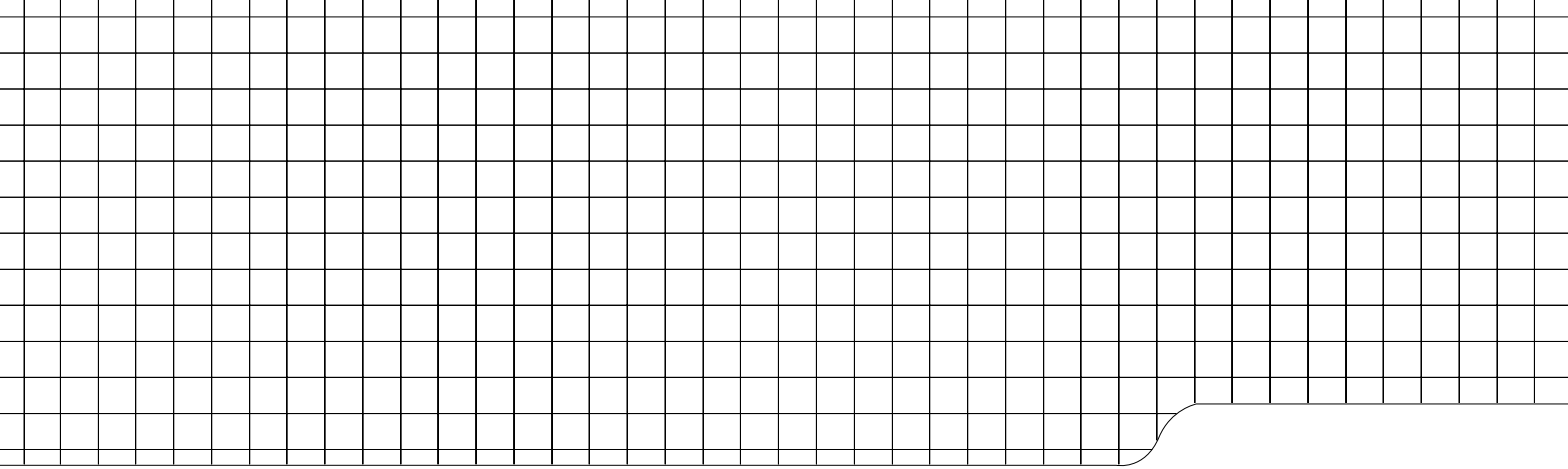
7. ACKNOWLEDGEMENT

REFERENCES

[1] J. Guitton and C. Puyal, "New trends in vibration and acoustic monitoring in nuclear components in EDF," *Progress in Nuclear Energy*, vol. 21, pp. 807–811, 1988.

[2] B. Michel and C. Puyal, "Operational and economical experience with vibration and loose parts monitoring systems on primary circuits of PWRs," *Progress in Nuclear Energy*, vol. 21, pp. 469–473, 1988.

[3] A. Trenty, C. Puyal, C. Vincent, M. H. Inchauspe, R. Baeyens, C. Messainguiral-Bruynooghe, and G. Lagarde, "Thimble vibration analysis and monitopring on 1300 and 900 MW reactors using accelerometers and in-core neutron noise (in French)," *Progress in Nuclear Energy*, vol. 21, pp. 97–106, 1988.

[4] I. Pázsit, L. A. Torres, C. Montalvo, Y. Kitamura, L. Nagy, and H. Nylén, "*Ringhals Diagnostics and Monitoring, Annual Research Report 2018-19*," CTH-NT-339/RR-22, Chalmers University of Technology, Göteborg, Sweden, June 2019.

[5] I. Pázsit and O. Glöckler, "BWR Instrument Tube Vibrations - Interpretation of Measurements and Simulation," *Annals of Nuclear Energy*, vol. 21, no. 12, pp. 759–786, 1994.

[6] C. Demazière, C. Sunde, V. Arzhanov, and I. Pázsit, "*Final Report on the Research Project Ringhals Diagnostics and Monitoring, Stage 8*," CTH-RF-177/RR-10, Chalmers University of Technology, Göteborg, Sweden, December 2003.

[7] C. Demazière, C. Sunde, and I. Pázsit, "*Final Report on the Research Project Ringhals Diagnostics and Monitoring, Stage 9*," CTH-RF-187/RR-11, Chalmers University of Technology, Göteborg, Sweden, January 2005.

[8] C. Sunde, J. Wright, C. Demazière, and I. Pázsit, "*Final Report on the Research Project Ringhals Diagnostics and Monitoring, Stage 10*," CTH-RF-194/RR-12, Chalmers University of Technology, Göteborg, Sweden, November 2005.

[9] C. Sunde, C. Demazière, and I. Pázsit, "*Final Report on the Research Project Ringhals Diagnostics and Monitoring, Stage 11*," CTH-NT-206/RR-13, Chalmers University of Technology, Göteborg, Sweden, February 2007.

[10] I. Pázsit, C. Demazière, C. Sunde, P. Bernitt, and A. Hernández-Solís, "*Final Report on the Research Project Ringhals Diagnostics and Monitoring, Stage 12*," CTH-NT-220/RR-14, Chalmers University of Technology, Göteborg, Sweden, August 2008.

[11] I. Pázsit, N. S. Garis, J. Karlsson, and A. Rácz, "*Forskningsprogram angående härddiagnostik med neutronbrusmetoder Etapp 3. Slutrapport,*" SKI Rapport 97:31, SKI, September 1999.

[12] I. Pázsit, C. Demazière, V. Arzhanov, and N. S. Garis, "*Research and Development Program in Reactor Diagnostics and Monitoring with Neutron Noise Methods Stage 7. Final Report,*" SKI Rapport 01:27, SKI, August 2001.

[13] I. Pázsit, C. Demazière, and V. Arzhanov, "*Research and Development Program in Reactor Diagnostics and Monitoring with Neutron Noise Methods Stage 8. Final Report,*" SKI Rapport 2003:08, SKI, January 2003.

[14] I. Pázsit and V. Dykin, "Investigation of the space-dependent noise induced by propagating perturbations," *Annals of Nuclear Energy*, vol. 37, no. 10, pp. 1329–1340, 2010.

[15] C. Demazière, V. Arzhanov, J. K.-H. Karlsson, and I. Pázsit, "*Final Report on the Research Project Ringhals Diagnostics and Monitoring, Stage 4,*" CTH-RF-145/RR-6, Chalmers University of Technology, Göteborg, Sweden, September 1999.

[16] I. Pázsit, C. Montalvo Martín, V. Dykin, and T. Tambouratzis, "*Final Report on the Research Project Ringhals Diagnostics and Monitoring, Stage 13,*" CTH-NT-230/RR-15, Chalmers University of Technology, Göteborg, Sweden, March 2010.

[17] I. Pázsit, L. A. Torres, C. Montalvo, L. Nagy, G. Klujber, M. Szieberth, T. Misawa, Y. Kitamura, V. Dykin, and H. Nylén, "*Ringhals Diagnostics and Monitoring, Annual Research Report 2020-21,*" CTH-NT-344/RR-24, Chalmers University of Technology, Göteborg, Sweden, June 2021.

[18] I. Pázsit (Ed.), "*Final Report on the Research Project Ringhals Diagnostics and Monitoring, Stage 1,*" CTH-RF-122/RR-3, Chalmers University of Technology, Göteborg, Sweden, September 1996.

[19] I. Pázsit, J. Karlsson, and N. Garis, "*Final Report on the Research Project Ringhals Diagnostics and Monitoring, Stage 2,*" CTH-RF-132/RR-4, Chalmers University of Technology, Göteborg, Sweden, October 1997.

[20] J. K.-H. Karlsson and I. Pázsit, "*Final Report on the Research Project Ringhals Diagnostics and Monitoring, Stage 3: Analysis of core barrel vibrations in Ringhals 2, 3 and 4 for several fuel cycles,*" CTH-RF-135/RR-5, Chalmers University of Technology, Göteborg, Sweden, October 1998.

[21] M. Pázsit and I. Pázsit, "*Final Report on the Analysis of Core Barrel Vibrations in Ringhals PWRs R2, R3 and R4 from Measurements Made in 2005,*" Internal report, Chalmers University of Technology, Göteborg, Sweden, 2006.

[22] I. Pázsit, C. Montalvo Martín, V. Dykin, and H. Nylén, "*Final Report on the Research Project Ringhals Diagnostics and Monitoring, Stage 14,*" CTH-NT-253/RR-16, Chalmers University of Technology, Göteborg, Sweden, December 2011.

[23] V. Dykin, C. Montalvo Martín, H. Nylén, and I. Pázsit, "*Ringhals Diagnostics and Monitoring, Final Research Report 2012 - 2014*," CTH-NT-304/RR-19, Chalmers University of Technology, Göteborg, Sweden, December 2014.

[24] V. Dykin, C. Montalvo, N. Tran, H. Nylén, and I. Pázsit, "*Ringhals Diagnostics and Monitoring, Annual Research Report 2015*," CTH-NT-319/RR-20, Chalmers University of Technology, Göteborg, Sweden, December 2015.

[25] I. Pázsit, C. Montalvo, N. Tran, H. Nylén, and O. Olvera Guerrero, "*Ringhals Diagnostics and Monitoring, Annual Research Report 2016-17*," CTH-NT-333/RR-21, Chalmers University of Technology, Göteborg, Sweden, December 2017.

[26] I. Pázsit, L. A. Torres, C. Montalvo, L. Nagy, M. Szieberth, G. Klujber, T. Misawa, Y. Kitamura, and H. Nylén, "*Ringhals Diagnostics and Monitoring, Annual Research Report 2019-20*," CTH-NT-342/RR-23, Chalmers University of Technology, Göteborg, Sweden, June 2020.

[27] M. Nilsson, "*Brusmätning för att söka lågfrekventa störningar i R3, Annual Research Report 2015*," Ringhals internal report UH-rapport 2099930 / 2.0, Ringhals AB, Göteborg, Sweden, October 2010.

[28] B. Severinsson, ""*Brusmätningar för analys av härdhöljesvibrationer på Ringhals 3. Utförda mellan 2013-02-26 och 2013-07-05*," Ringhals internal report UH-rapport 2245846 / 2.0, Ringhals AB, Göteborg, Sweden, July 2013.

[29] B. Severinsson, "*Brusmätning för analys av Härdhöljesvibrationer på utförda under 2013*," Ringhals internal report UH-rapport 2233461 / 2.0, Ringhals AB, Göteborg, Sweden, July 2013.

[30] J. A. Bezuidenhout, "Signature analysis of the primary components of the Koeberg nuclear power station," Master's thesis, North-West University, South Africa, 2010. URL http://hdl.handle.net/10394/4387.

[31] I. Pázsit and O. Glöckler, "On the Neutron Noise Diagnostics of Pressurized Water Reactor Control Rod Vibrations III. Application at a Power Plant," *Nuclear Science and Engineering*, vol. 99, no. 4, pp. 313–328, 1988.

[32] J. K. H. Karlsson and I. Pázsit, "Localisation of a channel instability in the Forsmark-1 boiling water reactor," *Annals of Nuclear Energy*, vol. 26, no. 13, pp. 1183–1204, 1999.

[33] I. Pázsit, "On the possible use of the neutron current in core monitoring and noise diagnostics," *Annals of Nuclear Energy*, vol. 24, no. 15, pp. 1257–1270, 1997.

[34] V. Arzhanov, I. Pázsit, and N. S. Garis, "Localization of a vibrating control rod pin in pressurized water reactors using the neutron flux and current noise," *Nuclear Technology*, vol. 131, no. 2, pp. 239–251, 2000.

[35] N. S. Garis, I. Pázsit, U. Sandberg, and T. Andersson, "Determination of PWR control rod position by core physics and neural network methods," *Nuclear Technology*, vol. 123, no. 3, pp. 278–295, 1998.

[36] P. Lindén, J. K. H. Karlsson, B. Dahl, I. Pázsit, and G. Por, "Localisation of a neutron source using measurements and calculation of the neutron flux and its gradient," *Nucl. Instr. Meth.*, vol. A 438, no. 2-3, pp. 345–355, 1999.

[37] S. Avdic, P. Lindén, and I. Pázsit, "Measurement of the neutron current and its use for the localisation of a neutron source," *Nucl. Instr. Meth.*, vol. A 457, no. 3, pp. 607–616, 2001.

[38] S. Avdic, P. Lindén, B. Dahl, and I. Pázsit, "Determination of the neutron current and diagnostic application in an experimental system.," *Nuklearna Tehnologija*, vol. 2, pp. 34–40, 2001.

[39] C. Mori, T. Osada, K. Yanagida, T. Aoyama, A. Uritani, H. Miyahara, Y. Yamane, K. Kobayashi, C. Ichihara, and S. Shiroya, "Simple and Quick Measurement of Neutron Flux Distribution by Using an Optical Fiber with Scintillator," *Journal of Nuclear Science and Technology*, vol. 31, no. 3, pp. 248–249, 1994.

[40] T. Yagi, H. Unesaki, T. Misawa, C. H. Pyeon, S. Shiroya, T. Matsumoto, and H. Harano, "Development of a small scintillation detector with an optical fiber for fast neutrons," *Applied Radiation and Isotopes*, vol. 69, no. 2, pp. 539–544, 2011.

[41] M. Al-dbissi, *Developments toward a novel methodology for spent nuclear fuel verification.* Licentiate Thesis, CTH-NT-347, Chalmers University of Technology, May 2022. URL: https://research.chalmers.se/en/publication/?id=530091.

[42] R. Rossa, A. Borella, and N. Giani, "Comparison of machine learning models for the detection of partial defects in spent nuclear fuel," *Annals of Nuclear Energy*, vol. 147, p. 107680, 2020.

[43] H. Lee and M.-S. Yim, "Investigation of a fast partial defect detection method for safeguarding pwr spent fuel assemblies," *Annals of Nuclear Energy*, vol. 144, p. 107496, 2020.

[44] J. Leppänen, "The Serpent Monte Carlo code: Status, development and applications in 2013," *Annals of Nuclear Energy*, vol. 82, pp. 142–150, 12015.

[45] C. J. Werner, "MCNP6.2 Release Notes," 2018.

[46] P. Bernard, J. Cloue, and C. Messainguiral, "Detection and monitoring of boiling in PWRs by incore neutron noise analysis," *Progress in Nuclear Energy*, vol. 9, pp. 581–594, 1982.

[47] V. Dykin, C. Montalvo Martín, H. Nylén, and I. Pázsit, "*Ringhals Diagnostics and Monitoring, Final Research Report 2012*," CTH-NT-269/RR-17, Chalmers University of Technology, Göteborg, Sweden, December 2012.

[48] V. Dykin, C. Montalvo Martín, H. Nylén, and I. Pázsit, "*Ringhals Diagnostics and Monitoring, Final Research Report 2013*," CTH-NT-286/RR-18, Chalmers University of Technology, Göteborg, Sweden, December 2013.

[49] V. Dykin and I. Pázsit, "Simulation of in-Core Neutron Noise Measurements for Axial Void Profile Reconstruction in Boiling Water Reactors," *Nuclear Technology*, vol. 183, no. 3, pp. 354–366, 2013.

[50] D. Wach and G. Kosály, "Investigation of the joint effect of local and global driving sources in incore-neutron noise measurements," *Atomkernenergie*, vol. 23, pp. 244–250, 1974.

[51] https://en.wikipedia.org/wiki/Stereoscopy.

[52] I. Pázsit, "Kan man se bilder i 3D utan glasögon?," Vetenskapsfestivalen i Göteborg, 18 April 2021. https://chalmersuniversity.box.com/s/impdxllwwr6o1lakccphhu024bkhv6i5.